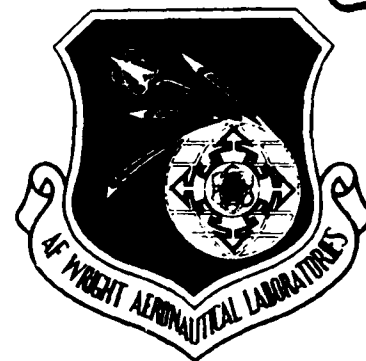


AD-A199 211

AFWAL-TR-88-2055



**ADVANCES IN THE NUMERICAL ANALYSIS OF LINEARIZED UNSTEADY
CASCADE FLOWS**

**Joseph M. Verdon
William J. Usab, Jr.**

**United Technologies Research Center
Silver Lane
East Hartford CT 06108**

August 1988

Interim Report for Period February 1985 - May 1988

Approved for public release; distribution is unlimited



**AEROPROPULSION LABORATORY
AIR FORCE WRIGHT AERONAUTICAL LABORATORIES
AIR FORCE SYSTEM COMMAND
WRIGHT-PATTERSON AIR FORCE BASE, OHIO 45433-6563**

88 9 9 002

NOTICE

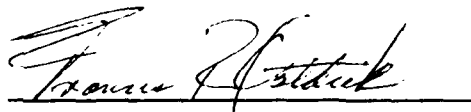
When Government drawings, specifications, or other data are used for any purpose other than in connection with a definitely Government-related procurement, the United States Government incurs no responsibility or any obligation whatsoever. The fact that the Government may have formulated or in anyway supplied the said drawings, specifications, or other data, is not to be regarded by implication, or otherwise in any manner construed, a licensing the holder, or any other person or corporation; or as conveying any rights or permission to manufacture, use, or sell any patented invention that may in any way be related thereto.

This report has been reviewed by the Office of Public Affairs (ASD/PA) and is releasable to the National Technical Information Service (NTIS). At NTIS, it will be available to the general public, including foreign nations.

This technical report has been reviewed and is approved for publication.




RICHARD J. MARTIN, Project Engineer
Compressor Research Group



FRANCIS R. OSTDIEK, Chief
Technology Branch

FOR THE COMMANDER



ROBERT E. HENDERSON
Deputy for Technology
Turbine Engine Division
Aero Propulsion Laboratory

If your address has changed, if you wish to be removed from our mailing list, or if the addressee is no longer employed by your organization please notify AFWAL/POTX, Wright-Patterson AFB, OH 45433-6563 to help us maintain a current mailing list.

Copies of this report should not be returned unless return is required by security considerations, contractual obligations, or notice on a specific document.

UNCLASSIFIED
SECURITY CLASSIFICATION OF THIS PAGE

REPORT DOCUMENTATION PAGE

1a. REPORT SECURITY CLASSIFICATION UNCLASSIFIED			1b. RESTRICTIVE MARKINGS		
2a. SECURITY CLASSIFICATION AUTHORITY			3. DISTRIBUTION/AVAILABILITY OF REPORT Approved for Public Release; Distribution Unlimited		
2b. DECLASSIFICATION/DOWNGRADING SCHEDULE					
4. PERFORMING ORGANIZATION REPORT NUMBER(S) UTRC Report R88-957685-1			5. MONITORING ORGANIZATION REPORT NUMBER(S) AFWAL-TR-88-2055		
6a. NAME OF PERFORMING ORGANIZATION United Technologies Research Center		6b. OFFICE SYMBOL (If applicable)		7a. NAME OF MONITORING ORGANIZATION Air Force Wright Aeronautical Laboratories Aeropropulsion Laboratory (AFWAL/POTX)	
6c. ADDRESS (City, State, and ZIP Code) Silver Lane East Hartford, CT 06108		7b. ADDRESS (City, State, and ZIP Code) Department of the Air Force Aeronautical Systems Division /PMRSA Wright Patterson AFB, OH 45433-6563			
8a. NAME OF FUNDING/SPONSORING ORGANIZATION		8b. OFFICE SYMBOL (If applicable)		9. PROCUREMENT INSTRUMENT IDENTIFICATION NUMBER F33615-84-C-2446	
8c. ADDRESS (City, State, and ZIP Code)		10. SOURCE OF FUNDING NUMBERS			
		PROGRAM ELEMENT NO. 62203F		PROJECT NO. 3066	TASK NO. 12
				WORK UNIT ACCESSION NO. 72	
11. TITLE (Include Security Classification) Advances in the Numerical Analysis of Linearized Unsteady Cascade Flows					
12. PERSONAL AUTHOR(S) Joseph M. Verdon and William J. Usab, Jr.					
13a. TYPE OF REPORT Interim		13b. TIME COVERED FROM 2/85 TO 5/88		14. DATE OF REPORT (Year, Month, Day) August 1988	
15. PAGE COUNT 80					
16. SUPPLEMENTARY NOTATION Project Manager: Mr. Richard Martin, Aeronautical Systems Division, Wright Patterson AFB, OH 45433					
17. COSATI CODES			18. SUBJECT TERMS (Continue on reverse if necessary and identify by block number)		
FIELD	GROUP	SUB-GROUP	Linearized Unsteady Flow; Two-Dimensional Compressor Cascade; Velocity Potential; Subsonic Transonic Flow; Shocks; Composite Solution Procedure; Transfinite Local Mesh; Unsteady Aerodynamic Response; Subsonic Flow		
01	01				
21	01				
19. ABSTRACT (Continue on reverse if necessary and identify by block number)					
<p>This report describes two new developments in the numerical analysis of linearized unsteady cascade flows, which have been motivated by the need for an accurate analytical procedure for predicting the onset of flutter in highly loaded compressor cascades. In previous work numerical solutions were determined using a two-step procedure in which a solution was first determined on a rectilinear-type cascade mesh to determine the unsteady flow over an extended blade-passage solution domain and then on a polar-type local mesh to resolve the unsteady flow in high-gradient regions. In the present effort a composite solution procedure has been developed in which the cascade and local mesh equations are solved simultaneously. This allows the detailed features of the flow within the local mesh region to impact the unsteady solution over the entire domain. In addition, a new shock-conforming local mesh has been introduced to permit a more accurate modeling of unsteady shock phenomena. Numerical results are presented to demonstrate the impact of the new composite solution procedure and the new local mesh on unsteady flow predictions. Results are also presented to illustrate the global unsteady aerodynamic response behavior of a compressor-type cascade operating at high subsonic inlet Mach numbers and at high mean incidences. <i>Keywords:</i></p>					
20. DISTRIBUTION/AVAILABILITY OF ABSTRACT <input checked="" type="checkbox"/> UNCLASSIFIED/UNLIMITED <input type="checkbox"/> SAME AS RPT. <input type="checkbox"/> DTIC USERS			21. ABSTRACT SECURITY CLASSIFICATION UNCLASSIFIED		
22a. NAME OF RESPONSIBLE INDIVIDUAL R. J. Martin			22b. TELEPHONE (Include Area Code) 513 255-8210		22c. OFFICE SYMBOL AFWAL/POTX

have been

SUMMARY

This report describes two new developments in the numerical analysis of linearized unsteady cascade flows. These have been motivated by the need for an accurate analytical procedure for predicting the onset of flutter in highly loaded compressor cascades operating at high subsonic inlet Mach number. In previous work numerical solutions were determined using a two-step procedure in which a solution was first determined on a rectilinear-type cascade mesh to determine the unsteady flow over an extended blade-passage solution domain and then on a polar-type local mesh to resolve the unsteady flow in high-gradient regions. Unfortunately, with this so-called single-pass approach the detailed local analysis could not impact the unsteady solution beyond the region covered by the local mesh. In addition, the polar local mesh did not allow an accurate modeling of unsteady shock phenomena.

Thus, in the present effort a composite solution procedure has been developed in which the cascade and local mesh equations are solved simultaneously. This procedure allows the detailed features of the flow within the local mesh region to impact the unsteady solution over an entire extended blade passage domain. In addition, a new transfinite local mesh has been introduced which contains "radial" lines that conform to the shape of the mean shock locus. Therefore, shock conditions can now be modeled more accurately. Numerical results are presented to demonstrate the impact of the new composite solution procedure and shock-conforming local mesh on unsteady flow predictions. We find that shocks have an unexpectedly strong effect on linearized unsteady transonic solutions. Results are also presented to illustrate the global unsteady aerodynamic response behavior of a compressor-type cascade operating at high subsonic inlet Mach numbers and at high mean incidences.

Accession For	
NTIS GRA&I	<input checked="checked" type="checkbox"/>
DTIC TAB	<input type="checkbox"/>
Unannounced	<input type="checkbox"/>
Justification	
By	
Distribution/	
Availability Codes	
Dist	Avail and/or Special
A-1	

TABLE OF CONTENTS

1. INTRODUCTION	1
2. PROBLEM DESCRIPTION	4
3. THE LINEARIZED UNSTEADY AERODYNAMIC FORMULATION	7
3.1 The Steady Background Flow	7
3.2 The Linearized Unsteady Problem	8
3.3 Aerodynamic Response at a Moving Blade Surface	9
4. NUMERICAL ANALYSIS	12
4.1 Calculation Meshes	13
4.2 Difference Approximations	14
4.3 Inversion of Cascade and Local Mesh Equations	16
5. TRANSFINITE LOCAL MESH	17
5.1 Interpolation Procedure	18
5.2 Mesh Generation Procedure	19
6. COMPOSITE SOLUTION PROCEDURE	22
6.1 Composite Mesh Equations	23
6.2 Inversion of Composite Equation System	25
7. DEMONSTRATION OF SOLUTION PROCEDURES	27
7.1 Single-Pass Solutions	28
7.2 Composite-Mesh Solutions	31
8. GLOBAL UNSTEADY AERODYNAMIC RESPONSE BEHAVIOR	34
9. CONCLUDING REMARKS	38
REFERENCES	65

LIST OF FIGURES

Figure	Page
1 Two-dimensional vibrating transonic compressor cascade; $M_{-\infty} < M_{\infty} < 1$.	40
2 Steady state, ———, and instantaneous, - - - -, blade, wake and shock mean positions.	41
3 Numerical solution domain: extended blade-passage region of finite extent.	42
4 Calculation meshes for unsteady cascade flows: (a) cascade mesh; (b) polar-type local mesh: • calculation point; o neighbor point.	43
5 Typical local-mesh domain: (a) physical domain; (b) parametric domain.	44
6 Schematic of composite mesh.	45
7 Mesh point classification: (a) local mesh; (b) cascade mesh.	46
8 Surface Mach number distributions for the example NACA 0006 cascade: (a) subsonic flow; $M_{-\infty} = 0.7$, $\Omega_{-\infty} = 55$ deg; (b) transonic flow; $M_{-\infty} = 0.8$, $\Omega_{-\infty} = 58$ deg.	47
9 Unsteady pressure difference distributions due to torsional blade vibrations of the subsonic NACA 0006 cascade; $\alpha = (1, 0)$, $\omega = 1$, $\sigma = 180$ deg: (a) cascade-mesh solution; (b) single-pass solution using polar local mesh; (c) single-pass solution using transfinite local mesh: - - - - in-phase component (real part); ——— out-of-phase component (imaginary part).	48
10 Unsteady pressure difference distributions due to torsional blade vibrations of the transonic NACA 0006 cascade; $\alpha = (1, 0)$, $\omega = 1$, $\sigma = 180$ deg: (a), (b), (c), - - - - and ——— as in Figure 9: shocks are captured in the local calculations.	49
11 Unsteady pressure difference distributions due to torsional blade vibrations of the transonic NACA 0006 cascade; $\alpha = (1, 0)$, $\omega = 1$, $\sigma = 180$ deg: (a), (b), (c), - - - - and ——— as in Figure 9; shocks are fitted in the local calculations.	50
12 Single-pass solution for the unsteady potential contours due to torsional blade vibrations of the subsonic NACA 0006 cascade; $\alpha = (1, 0)$, $\omega = 1$, $\sigma = 180$ deg: (a) in-phase component (real part of ϕ); (b) out-of-phase component (imaginary part of ϕ).	51

Figure	Page
13 Single-pass solution for the unsteady potential contours due to torsional blade vibrations of the transonic NACA 0006 cascade; $\alpha = (1, 0)$, $\omega = 1$, $\sigma = 180$ deg: (a) and (b) as in Figure 12.	52
14 Composite solution for the unsteady potential contours due to torsional blade vibrations of the subsonic NACA 0006 cascade; $\alpha = (1, 0)$, $\omega = 1$, $\sigma = 180$ deg: (a) and (b) as in Figure 12.	53
15 Composite solution for the unsteady potential contours due to torsional blade vibrations of the transonic NACA 0006 cascade; $\alpha = (1, 0)$, $\omega = 1$, $\sigma = 180$ deg: (a) and (b) as in Figure 12.	54
16 Unsteady pressure difference distributions due to torsional blade vibrations of the subsonic NACA 0006 cascade: $\alpha = (1, 0)$, $\omega = 1$, $\sigma = 180$ deg: (a) composite solution using polar local mesh; (b) composite solution using transfinite local mesh: - - - in-phase component; — out-of-phase component.	55
17 Composite solutions for the unsteady pressure difference distributions due to torsional blade vibrations of the transonic NACA 0006 cascade; $\alpha = (1, 0)$, $\omega = 1$, $\sigma = 180$ deg: (a), (b), - - - and — as in Figure 16: shocks are captured in the unsteady calculation.	56
18 Composite solutions for the unsteady pressure difference distributions due to torsional blade vibrations of the transonic NACA 0006 cascade; $\alpha = (1, 0)$, $\omega = 1$, $\sigma = 180$ deg: (a), (b), - - - and — as in Figure 16: shocks are fitted in unsteady calculation.	57
19 Out-of-phase component of unsteady lift vs interblade phase angle for pure bending vibrations of the NACA 0006, —, and flat-plate, - - -, cascades: (a) $M_{\infty} = 0.7$, $\omega = 1$; (b) $M_{\infty} = 0.8$, $\omega = 0.5$.	58
20 Out-of-phase component of unsteady moment vs interblade phase angle for pure torsional blade vibrations of the NACA 0006, —, and flat-plate, - - -, cascades: (a) $M_{\infty} = 0.7$, $\omega = 1.5$; (b) $M_{\infty} = 0.8$, $\omega = 1.0$.	59
21 Out-of-phase component of unsteady lift vs interblade phase angle for pure bending vibrations of the flat-plate cascade at $\omega = 0.5, 1.0, 1.5$ and 2.0 : (a) $M_{\infty} = 0.7$; (b) $M_{\infty} = 0.8$.	60
22 Out-of-phase component of unsteady lift vs interblade phase angle for pure bending vibrations of the NACA 0006 cascade at $\omega = 0.5, 1.0, 1.5$ and 2.0 : (a) $M_{\infty} = 0.7$; (b) $M_{\infty} = 0.8$.	61

Figure	Page
23 Out-of-phase component of unsteady moment vs interblade phase angle for pure torsional vibrations of the flat-plate cascade at $\omega = 0.5, 1.0, 1.5$ and 2.0 : (a) $M_{\infty} = 0.7$; (b) $M_{\infty} = 0.8$.	62
24 Out-of-phase component of unsteady moment vs interblade phase angle for pure torsional vibrations of the NACA 0006 cascade at $\omega = 0.5, 1.0, 1.5$ and 2.0 : (a) $M_{\infty} = 0.7$; (b) $M_{\infty} = 0.8$.	63
25 Out-of-phase components of the shock loads due to single-degree-of-freedom blade motions of the transonic NACA 0006 cascade: (a) lift force due to bending; (b) moment due to torsion.	64

1. INTRODUCTION

The development of theoretical analyses to predict unsteady flows in axial-flow turbomachines has been motivated primarily by the need to predict the aeroelastic behavior of the blading, i.e., blade flutter and forced vibration. For this purpose such analyses must be capable of predicting the unsteady loads acting on the blades and arising from various sources of unsteady excitation, i.e., prescribed structural (blade) motions and external aerodynamic excitations. The latter include variations in total temperature and total pressure ("entropy and vorticity waves") at inlet and variations in static pressure (acoustic waves) at inlet and exit. In particular, for blade flutter applications it is only necessary to predict the unsteady loads due to prescribed blade motions, while for forced response applications the unsteady loads due to incident entropic, vortical and acoustic disturbances are also required.

For the most part, in the unsteady aerodynamic analyses intended for turbomachinery aeroelastic applications the blades of an isolated, usually two-dimensional, cascade are considered, viscous effects are neglected and unsteady fluctuations are regarded as sufficiently small so that a linearized treatment of the unsteady flow is justified. Linearizations, which include the effects of realistic design features, such as blade geometry, mean blade loading and operation at transonic Mach numbers (see Refs. 1 and 2), have been actively developed over the past decade. Here, the unsteady flow is regarded as a small-amplitude harmonic (in time) fluctuation about a fully nonuniform isentropic and irrotational mean or steady flow. The steady flow is determined as a solution of the full potential boundary-value problem, and the unsteady flow is governed by linear equations with variable coefficients which depend on the underlying steady flow. Although analyses based on this type of linearization have received considerable attention in recent years (c.f. Refs. 3-8), significant advances in the associated numerical solution procedures are still required before it will be appropriate to consider them for transonic design applications.

This report describes contributions to the numerical analysis of linearized unsteady flows around the vibrating blades of compressor-type cascades operating at high subsonic inlet Mach number and at high mean incidence. The present work builds upon that reported in Refs. 6 and 8 and is motivated by the need to provide an unsteady aerodynamic analysis for the prediction of subsonic/transonic positive incidence flutter in compressor blade rows. Subsonic/transonic positive incidence flutter is the most common type of flutter encountered in the fan and compressor stages of axial-flow turbomachines. It usually occurs in blading that is highly loaded and operating at high subsonic inlet Mach number, and it is characterized by an increase in flutter stress as exit to inlet static pressure ratio is increased. It may occur at part speed in a high-speed fan and at or near design speed in a low- or high-pressure compressor. Flutter in bending, torsion and coupled (bending-torsion) blade vibration modes have been observed over a reduced frequency (based on relative inlet flow speed and blade chord) range extending from 0.4 to 1.6. In an unshrouded rotor the blade motions are generally unphased at low amplitudes

with the possibility of a constant interblade phase angle at larger amplitudes of vibration. In a shrouded rotor phasing is enforced by part-span mechanical ties (Refs. 9 and 10).

The linearized unsteady aerodynamic analysis developed in Refs. 6 and 8 accounts for the important effects of blade geometry and mean pressure rise (or fall) across a blade row (i.e., mean blade loading). Furthermore, this analysis applies to transonic flows and includes the effects of shocks and their motions in the prediction of unsteady airloads. The linearized unsteady equations are solved numerically using an implicit least-squares finite-difference approximation which is applicable on arbitrary grids. Solutions have been reported for subsonic flows through cascades of NACA 0012 airfoils (Ref. 6) and for subsonic and transonic flows through vibrating cascades of sharp-edged flat-bottomed double-circular-arc (DCA) airfoils (Ref. 8). More recently, the analysis has been applied to representative two-dimensional outer-span sections of an actual fan rotor (Ref. 11), to a NASA Lewis flutter cascade (Ref. 12) and to four of the nine standard configurations suggested by T. Fransson and P. Suter (Refs. 13, 14) for theoretical and experimental investigations on turbomachine cascades (Ref. 15).

Because of the stringent and often conflicting requirements placed on the construction of a computational mesh for cascade flows, a two-step numerical solution procedure was adopted in Refs. 6 and 8. Here the basic approach is to first capture large-scale unsteady phenomena on a rectilinear-type cascade mesh of moderate density and then to determine detailed phenomena on a polar-type local grid of high density. The cascade mesh covers an extended blade-passage solution domain, while the local mesh covers and extends well beyond a region of high velocity gradient, e.g., a region surrounding a rounded blade leading edge (Ref. 6) or a region containing a shock (Ref. 8). Information determined by the cascade mesh solution provides the outer boundary-condition information for the local calculation, and the solution to the unsteady boundary-value problem is taken to be the local solution in the region covered by the local mesh and the cascade solution elsewhere. Thus the local solution is essentially a correction to the cascade solution over the local mesh region since there is no iteration between the two calculations.

The local mesh of Refs. 6 and 8 consists of radial and circumferential lines normal and roughly parallel respectively to a blade surface. For a discontinuous transonic flow two of the radial lines are positioned at the mean location of the shock foot to represent information on the upstream and downstream sides of a shock. Hence, the mean shock locus is approximated as being normal to the airfoil surface in the local unsteady calculation.

In the present effort improvements have been made to the numerical solution methods of Refs. 6 and 8 so that flows around realistic compressor blades operating at high subsonic inlet Mach number and high mean incidence can be considered. For such applications the local solution must provide an accurate description of the flow both in the vicinity of a rounded blade leading edge as well as in the vicinity of a shock. In addition, the global and local solutions should be coupled so that local unsteady information is allowed to impact the flow over an entire blade-passage solution domain. Finally, a local mesh topology in which mesh lines conform closely to the mean shock locus should be employed. These

considerations are addressed in the present report and demonstrated through a number of example calculations. In addition, the results of parametric studies are presented to partially illustrate the effects of mean flow nonuniformities on the unsteady aerodynamic response to vibrating compressor blades operating at high subsonic inlet Mach number and at high mean incidence.

2. PROBLEM DESCRIPTION

We consider time-dependent adiabatic flow, with negligible body forces, of an inviscid non-heat-conducting perfect gas through a two-dimensional cascade of vibrating blades (see Fig. 1). In the following discussion all physical quantities are dimensionless. Lengths have been scaled with respect to blade chord, time with respect to the ratio of blade chord to the upstream free-stream speed, density and velocity with respect to the upstream free-stream density and velocity, respectively, and pressure with respect to the product of the upstream free-stream density and the square of the upstream free-stream speed. The mean or steady-state positions of the blade chord lines coincide with the line segments $\eta = \xi \tan \Theta + mG$, $0 \leq \xi \leq \cos \Theta$, $m = 0, 1, 2, \dots$, where ξ and η are Cartesian coordinates attached to the blade row and pointing in the axial-flow and cascade "circumferential" directions, respectively, m is a blade number index, Θ is the cascade stagger angle, and \vec{G} is the cascade gap vector which is directed along the η -axis with magnitude equal to the blade spacing.

The blade motions are of small-amplitude, periodic in time and periodic in the η -direction. Thus,

$$\vec{\mathcal{R}}(\vec{X} + m\vec{G}, t) = \text{Re}\{\vec{r}_{B_m}(\vec{X} + m\vec{G}) \exp(i\omega t)\} = \text{Re}\{\vec{r}_B(\vec{X}) \exp[i(\omega t + m\sigma)]\}, \quad \vec{X} \in B \quad (2.1)$$

where $\vec{\mathcal{R}}$ measures the displacement of a point on a moving blade surface relative to its mean or steady-state position, \vec{X} is a position vector relative to the space-fixed ξ, η - (or x, y -) coordinate axes, t is time, \vec{r} is a complex displacement-amplitude vector with $|\vec{r}| \sim \mathcal{O}(\epsilon)$, ω is the frequency of the blade motion, σ is the phase angle between the motions of adjacent blades, $\text{Re}\{\}$ denotes the real part of $\{\}$ and B denotes the mean position of the reference ($m = 0$) blade surface.

In the absence of blade motion the flows far upstream ($\xi < \xi_-$) and far downstream ($\xi > \xi_+$) from the blade row are assumed to be at most small irrotational steady perturbations of a uniform free stream. In addition, blade shape and orientation relative to the inlet free-stream direction, the inlet to exit mean static pressure ratio and the amplitude, frequency and mode of the blade motion are assumed to be such that the flow remains attached to the blade surfaces. Thus thin vortex sheets or unsteady wakes emanate from the blade trailing edges and extend downstream. Finally, any shocks that might occur are assumed to be of weak to moderate strength, have small curvature and terminate in a continuous region of the flow, i.e., at a sonic point. Because of the first two of these shock assumptions, changes in the entropy and vorticity of a fluid particle as it passes through a shock can be regarded as negligible.

The equations governing the fluid motion follow from the integral forms of the mass, momentum and energy conservation laws and the thermodynamic relations for a perfect gas. The former provide a coupled set of corresponding nonlinear differential equations (the Euler equations) in continuous regions of the flow and jump conditions (Rankine-Hugoniot conditions) at surfaces across which the inviscid flow variables are discontinuous, i.e., vortex-sheet wakes and shocks. In continuous regions the energy equation

can be replaced by the requirement that the entropy following a fluid particle must remain constant. However, as a consequence of our assumptions regarding shocks and the steady flow far upstream of the blade row and, since blade motions are the only source of unsteady excitation, the time dependent flow through the cascade can be regarded as isentropic and irrotational. In this case, the field equations governing the flow reduce to

$$\frac{\partial \tilde{\rho}}{\partial t} + \nabla \cdot (\tilde{\rho} \nabla \tilde{\Phi}) = 0 \quad (2.2)$$

and

$$\tilde{\rho}^{(\gamma-1)} = (\gamma M_{-\infty}^2 \tilde{P})^{(\gamma-1)/\gamma} = (M_{-\infty} \tilde{A})^2 = 1 - (\gamma - 1) M_{-\infty}^2 \left\{ \frac{\partial \tilde{\Phi}}{\partial t} + [(\nabla \tilde{\Phi})^2 - 1]/2 \right\} \quad (2.3)$$

where $\tilde{\Phi}$, $\tilde{\rho}$, \tilde{P} and \tilde{A} are the time-dependent velocity potential, density, pressure and speed of sound propagation, respectively, M is the Mach number of the undisturbed or steady flow, γ is the specific heat ratio of the fluid and the subscript $-\infty$ refers to the upstream free-stream condition. The admissible solutions to Equations (2.2) and (2.3), for the present application, are those in which far-field acoustic disturbances either attenuate with increasing axial distance from the blade row or propagate away from or parallel to the blade row.

The foregoing field equations must be supplemented by boundary conditions at moving blade surfaces, B_m , and jump conditions at moving blade wakes, W_m , and at moving shocks, $Sh_{m,n}$. Here, the subscript n refers to the n th shock associated with the m th blade. In particular, the condition of flow tangency at blade surfaces requires that

$$(\nabla \tilde{\Phi} - \frac{\partial \tilde{\mathcal{R}}}{\partial t}) \cdot \tilde{n} = 0, \quad \tilde{X} \text{ on } B_m. \quad (2.4)$$

Also, the fluid pressure and normal velocity component must be continuous across blade wakes and therefore

$$[\tilde{P}] = 0 \text{ and } [\nabla \tilde{\Phi}] \cdot \tilde{n} = 0, \quad \tilde{X} \text{ on } W_m. \quad (2.5)$$

Finally, mass and tangential momentum must be conserved across shocks, i.e.,

$$[\tilde{\rho}(\nabla \tilde{\Phi} - \frac{\partial \tilde{\mathcal{R}}}{\partial t})] \cdot \tilde{n} = 0 \quad \text{and} \quad [\tilde{\Phi}] = 0, \quad \tilde{X} \text{ on } Sh_{m,n} \quad (2.6)$$

Here the unit vectors \tilde{n} and $\tilde{\tau}$ are normal and tangential, respectively, to a surface and directed such that $\tilde{n} \times \tilde{\tau} = \tilde{e}_z$ points out from the page. The relative displacement vector, $\tilde{\mathcal{R}}$, measures the displacement of a point on a moving surface (blade, wake or shock) relative to its mean position (see Fig. 2). Note that, since we have assumed that changes in entropy and vorticity across shocks are negligible, the conservation laws, i.e., the Rankine-Hugoniot conditions, cannot all be enforced at shock surfaces. Instead, we have followed the usual practice in potential flow calculations and have required only that

mass and tangential momentum be conserved. Also, the explicit form given in Equation (2.6) for the tangential-momentum conservation law follows from the assumption that shocks terminate at sonic points.

In addition to the foregoing field equations and surface conditions, information on the uniform inlet and exit flow conditions must be specified. Steady and unsteady departures from these uniform conditions (e.g., departures due to steady and unsteady pressure variations) must be determined as part of the time-dependent solution.

The foregoing problem is a formidable one consisting of a nonlinear, time-dependent, partial differential equation along with conditions imposed on moving blade, shock and wake surfaces in which the instantaneous locations of shock and wake surfaces must, in principle, be determined as part of the solution. Although numerical solutions to this problem are of substantial interest, they would be of limited practical value for predicting blade flutter because of the substantial expense involved in obtaining the detailed unsteady response predictions needed. For aeroelastic design applications the traditional approach has been to examine limiting forms of the foregoing time-dependent nonlinear equation set with the intention of providing unsteady aerodynamic response information for small-amplitude unsteady excitations. One such approach, in which the unsteady flow is regarded as a small perturbation of a fully nonuniform mean flow, is described below.

3. THE LINEARIZED UNSTEADY AERODYNAMIC FORMULATION

The equations governing small-amplitude time-dependent departures from a nonuniform mean flow are determined by first expanding the unsteady flow variables into asymptotic series in ϵ , where $|\vec{R}| \sim \mathcal{O}(\epsilon) \ll 1$. Thus, for example, the unsteady velocity potential $\tilde{\Phi}(\vec{X}, t)$ is expressed in the form

$$\tilde{\Phi}(\vec{X}, t) = \Phi(\vec{X}) + \tilde{\phi}(\vec{X}, t) + \dots = \Phi(\vec{X}) + \text{Re}\{\phi(\vec{X})e^{i\omega t}\} + \dots \quad (3.1)$$

where $\Phi(\vec{X})$ is the potential of the mean or steady background flow, $\tilde{\phi}(\vec{X}, t) \sim \mathcal{O}(\epsilon)$ is the first-order (in ϵ) time-dependent potential and $\phi(\vec{X})$ is its complex amplitude. In addition, Taylor series expansions, e.g.,

$$\nabla \tilde{\Phi}|_S = \nabla \tilde{\Phi}|_s + (\vec{R} \cdot \nabla) \nabla \tilde{\Phi}|_s + \dots \quad (3.2)$$

where S and s denote the instantaneous and mean positions, respectively, of a moving surface, and relations between the unit tangent, $\vec{\tau}$, and normal, \vec{n} , vectors at a point on a moving surface and the corresponding vectors at the location of this point on the mean surface are applied to refer information at a moving blade, wake or shock surface to the mean position of this surface.

The equations governing the steady and the first-order unsteady flows are then obtained by substituting the foregoing expansions into the full time-dependent governing equations, equating terms of like power in ϵ and neglecting terms of higher than first-order in ϵ . Note that if we assume that $|\nabla \tilde{\Phi}| = V_{-\infty} + \mathcal{O}(\epsilon)$ where \vec{V} is the steady velocity and the subscript $-\infty$ refers to the upstream free-stream condition, the equations of classical linearized unsteady aerodynamic theory (Ref. 16) are recovered; while if we assume that $|\nabla \tilde{\Phi}| = \vec{V}_{-\infty} + \mathcal{O}(\bar{\epsilon})$, where $\epsilon \ll \bar{\epsilon} \ll 1$, we recover the equations of time-linearized transonic flow theory (Ref. 17). Here, we consider a more general case in which no restrictions are placed on the departures of the mean flow variables from their upstream free-stream values.

3.1 The Steady Background Flow

The equations governing the steady background flow follow after replacing the time-dependent flow properties, $\tilde{\Phi}$, \tilde{P} , $\tilde{\rho}$ and \tilde{A} , by their zeroth-order of steady counterparts, Φ , P , $\bar{\rho}$, and A , respectively, in Equations (2.2) through (2.6) and setting temporal derivatives equal to zero. Numerical procedures for determining two-dimensional steady potential flows through cascades have been developed extensively, particularly for flows with subsonic inlet and exit Mach numbers (i.e., $M_{\mp\infty} < 1$) (e.g., see Refs. 18, 19). In such calculations far-field boundary conditions are imposed at axial stations placed at finite distances upstream and downstream (i.e., at $\xi = \xi_{\mp}$) from the blade row.

In general, three of the far-field uniform velocity components, or their equivalents (e.g., Mach number $M_{\mp\infty}$, flow angle $\Omega_{\mp\infty}$, etc. must be prescribed to completely specify the steady boundary-value problem. The fourth or remaining component can be determined in terms of the three prescribed using an integral form of the mass conservation

law. However, conditions are often imposed at blade edges (e.g., a Kutta condition at sharp trailing edges) in lieu of prescribing an inlet and/or an exit free-stream property. In addition, the usual practice is to solve the conservative form of the mass-balance equation throughout the entire fluid domain while allowing for a discontinuity in the velocity potential across arbitrary periodic lines which emanate from the blade trailing-edge points and extend downstream. Thus, shock-jump conditions are usually not imposed, instead, shock phenomena are captured through the use of special differencing techniques. Mean wake, i.e., the downstream stagnation streamlines, and shock locations are determined *a posteriori* from the resulting steady solution.

3.2 The Linearized Unsteady Problem

It follows from the differential form of the mass conservation law, Equation (2.2), the Bernoulli relations, Equation (2.3), the corresponding steady equations and the asymptotic expansions for the flow variables that the linearized unsteady flow is governed by the field equations

$$i\omega\rho + \nabla \cdot (\bar{\rho}\nabla\phi + \rho\nabla\Phi) = 0 \quad (3.3)$$

and

$$\rho/\bar{\rho} = \gamma^{-1}p/P = \frac{2}{\gamma-1}a/A = -A^{-2}\frac{\bar{D}\phi}{Dt} \quad (3.4)$$

where ρ , p and a are the complex amplitudes of the first harmonic unsteady density, pressure and speed of sound propagation, respectively, and $\bar{D}/Dt = i\omega + \vec{V} \cdot \nabla$ is a mean flow convective derivative operator. Equations (3.3) and (3.4) can be combined to obtain a single differential equation, i.e.,

$$A^2\nabla^2\phi = \frac{\bar{D}^2\phi}{Dt^2} + (\gamma-1)\nabla^2\Phi\frac{\bar{D}\phi}{Dt} + \nabla(\nabla\Phi)^2 \cdot \nabla\phi/2 \quad (3.5)$$

which contains the velocity potential as the only dependent variable.

Conditions on the linearized unsteady perturbation at blade, B_m , wake, W_m , and shock, $Sh_{m,n}$, mean positions are obtained in a similar fashion. The resulting first-order flow tangency condition has the form

$$\nabla\phi \cdot \vec{n} = [i\omega\vec{r}_{B_m} + (\nabla\Phi \cdot \vec{\tau})(\vec{\tau} \cdot \nabla)\vec{r}_{B_m} - (\vec{r}_{B_m} \cdot \nabla)\nabla\Phi] \cdot \vec{n} \quad (3.6)$$

In addition, since the steady velocity and pressure are continuous and have continuous derivatives across blade wakes, i.e., the downstream stagnation streamlines, the first-order wake-jump conditions reduce simply to

$$[\nabla\phi] \cdot \vec{n} = 0 \quad \text{and} \quad \left[\frac{\bar{D}\phi}{Dt}\right] = 0 \quad (3.7)$$

Finally, the conservation laws for mass and tangential momentum yield the following linearized shock-jump conditions:

$$[\bar{\rho}\nabla\phi + \rho\nabla\Phi] \cdot \vec{n} = [\bar{\rho}](i\omega + (\nabla\Phi \cdot \vec{\tau})\vec{\tau} \cdot \nabla)(\vec{r}_{Sh_{m,n}} \cdot \vec{n}) + (\vec{r}_{Sh_{m,n}} \cdot \vec{n})\vec{\tau} \cdot \nabla([\bar{\rho}]\nabla\Phi \cdot \vec{\tau}) \quad (3.8a)$$

and, for a shock that terminates in the fluid

$$[\phi] = -\tilde{r}_{sh,m,n} \cdot \tilde{n} [\nabla \Phi] \cdot \tilde{n} \quad (3.8b)$$

where we have assumed that shocks terminate at sonic points. Equations (3.8a) and (3.8b) provide two relations for determining the jump in the unsteady potential, $[\phi]$, at the mean position of a shock and the shock displacement normal to the mean shock locus, $\tilde{r}_{sh,m,n} \cdot \tilde{n}$. These equations can be combined (see Equation (4.7) below) to provide a single relation governing the jump in the unsteady potential across a shock. Recall that blade mean positions and unsteady motions are prescribed, but that wake and shock mean positions and displacements must be determined as part of the steady and unsteady solutions, respectively. Wake motions, however, have no direct impact on the solution to the linearized unsteady problem nor, therefore, on the aerodynamic response at the blade surfaces.

We have assumed that the potential mean or steady flow is at most a small (i.e., of $O(\epsilon)$) perturbation from a uniform stream both far upstream ($\xi < \xi_-$) and far downstream ($\xi > \xi_+$) from the blade row. Thus, in these regions and to within the first-order approximation considered here, the unsteady field equation and wake-jump conditions can be reduced to the constant coefficient equations of classical linearized theory for which analytical solutions can be determined. These solutions (see Refs. 1, 20) describe the unsteady potential produced by acoustic disturbances in the far field and the vorticity convected along the blade wakes, and they can be matched to a near field numerical solution. They thus serve to complete the specification of the linearized unsteady boundary-value problem.

3.3 Aerodynamic Response at a Moving Blade Surface

The foregoing linearized unsteady boundary-value problem accounts for the effects of mean blade geometry, mean blade loading and transonic phenomena, including moving shocks, on the unsteady aerodynamic fluctuations arising from small-amplitude harmonic blade motions. The unsteady equations are linear, time-independent and contain variable coefficients which depend on a fully nonlinear isentropic and irrotational steady background flow. Numerical resolutions of the nonlinear steady and the linearized unsteady problems are required to determine the aerodynamic response information needed for aeroelastic applications, i.e., the unsteady pressures and global unsteady airloads acting on the blade surfaces. Because of the cascade geometry and the assumed form of the blade motions (i.e., periodic in η), such resolutions are required only over a single extended blade-passage region. In addition, since analytic far-field solutions can be determined, the numerical solution domain can be further restricted to a single extended blade-passage region of finite extent as shown in Fig. 3.

The pressures acting along the instantaneous position of the m th blade surface are given by

$$\tilde{P}_B(\tau, t) = P_B(\tau) + \text{Re}\{p_B(\tau)e^{i(\omega t + m\sigma)}\} + \sum_n p_{sh,m,n}(\tau, t) + \dots, \quad (3.9)$$

where τ is a coordinate measuring distance in the counterclockwise (or $\vec{\tau}$ -) direction along a blade surface, and the subscripts B and \mathcal{B} refer to the mean and instantaneous positions of the reference blade surface. The first two terms on the right-hand-side of Equation (3.9) are the steady and first-harmonic unsteady, i.e.,

$$p_{\mathcal{B}} = -\bar{\rho} \frac{\bar{D}\phi}{Dt} + (\vec{r}_{\mathcal{B}} \cdot \nabla)P, \quad \vec{X} \in \mathcal{B} \quad (3.10)$$

components of the fluid pressure acting at the m th moving blade surface, \mathcal{B}_m . The third term represents the anharmonic contribution to the unsteady surface pressure caused by the motions of shocks along the surface of the m th blade, and is determined by analytically continuing the solutions to the steady and the linearized unsteady boundary-value problems from the mean to the instantaneous shock locations (see Refs. 8, 21, 22).

Thus, for example,

$$p_{Sh}(\tau, t) = -\frac{Re\{r_{Sh,B}\}}{|Re\{r_{Sh,B}\}|} U[(\tau - \tau_{Sh})(\tau_{Sh} - \tau)] \quad (3.11)$$

$$\times ([P_B]_{Sh} + (\tau - \tau_{Sh})[\partial P_B / \partial \tau]_{Sh} + Re\{[p_B]_{Sh} e^{i(\omega t + m\sigma)}\} + \dots),$$

where $r_{Sh,B} = (\vec{r}_{Sh} - \vec{r}_B) \cdot \vec{\tau}$ is the complex amplitude of the relative displacement of the shock foot in the counterclockwise or $\vec{\tau}$ -direction along the moving blade surface, U is the unit step function and the subscripts Sh and \mathcal{Sh} refer to the instantaneous and mean shock locations, respectively. It should be noted that although the unsteady pressure disturbance is not everywhere harmonic, its regions of anharmonicity are small. Consequently, the first-order global coefficients are harmonic in time (Refs. 23, 24).

If we limit our consideration to the condition usually considered in turbomachinery aeroelastic calculations wherein each incremental two-dimensional blade section undergoes a rigid-body motion, i.e.,

$$\vec{r}_B(\vec{X}) = \vec{h} + \vec{\alpha} \times \vec{R}_P, \quad (3.12)$$

then the unsteady force and moment are the only global response parameters needed to analyze the aeroelastic behavior of the blading. In Equation (3.12) \vec{h} defines the amplitude and direction of blade translations, $\vec{\alpha} = \alpha \vec{e}_z$ defines the amplitude and direction of blade rotations, and \vec{R}_P is a position vector extending from the mean position of the reference blade axis of rotation (i.e., from the point X_P, Y_P) to points on the mean position of the reference blade surface. These rigid two-dimensional motions model bending and torsional vibrations of actual rotor blades.

The linearized unsteady force and moment acting on the reference ($m = 0$) blade are given by

$$\vec{f} = \vec{\alpha} \times \vec{F} - \oint_B p_{\mathcal{B}} \vec{n} d\tau + \sum_n r_{Sh_n,B} ([P_B] \vec{n}_B)_{Sh_n} \quad (3.13)$$

and

$$m_P = \oint_B p_{\mathcal{B}} \vec{R}_P \cdot d\vec{\tau} - \sum_n r_{Sh_n,B} ([p_B] \vec{R}_P \cdot \vec{r}_B)_{Sh_n} \quad (3.14)$$

where \vec{F} is the steady force, the moment is taken about a moving pitching axis located at $\vec{X}_p = \vec{X}_p + \vec{h}e^{i\omega t}$, \vec{f} and m_p are the complex amplitudes of the linearized unsteady force and moment, respectively, and the terms within the summations in Equations (3.13) and (3.14) account for the concentrated loads due to shock motion and are evaluated at the shock roots.

4. NUMERICAL ANALYSIS

A numerical resolution of the linear, variable-coefficient, unsteady, boundary-value problem is required over a single, extended, blade-passage region of finite extent. The unsteady differential equation, in this case Equation (3.5), must be solved in continuous regions of the flow subject to boundary or jump conditions imposed at the mean positions of the blade, wake and shock surfaces. Blade mean positions are prescribed, and the mean positions of wake (i.e., the downstream stagnation streamlines) and shock surfaces are determined as part of the steady solution. Finally, the unsteady near-field numerical solution must be matched to far-field analytical solutions at finite distances ($\xi = \xi_{\mp}$) upstream and downstream from the blade row. Since the unsteady numerical model, used herein, has been described in some detail in Refs. 6, 8 and 25, we will provide only a brief outline here. In this discussion we will consider, for simplicity, flows in which at most a single shock occurs in each blade passage. Subsequently, we will describe in some detail the construction and implementation of a new shock-conforming local mesh and a new composite solution procedure. These features enhance the accuracy of unsteady subsonic and transonic flow predictions, particularly the latter, and extend the range of application of the numerical solution procedure.

Because of the stringent and conflicting requirements placed on a computational mesh for cascade flows, an embedded mesh solution procedure was adopted in Refs. 6 and 8 for resolving linearized unsteady cascade flows. In particular a sheared *H*-type cascade mesh of moderate density was used to capture large-scale unsteady phenomena over an extended blade passage solution domain, and a local surface-fitted mesh of high density was used to resolve high-gradient phenomena such as that which occurs in the vicinity of a rounded blade leading edge in Ref. 6 or near a shock in Ref. 8. The cascade mesh covers an extended blade-passage solution domain; the local mesh covers, and extends well beyond, regions of high velocity gradient. For application to compressor cascades operating at high mean incidence the local mesh surrounds a blunt blade leading edge, and for a discontinuous transonic flow, it also contains the shock and the entire supersonic zone ahead of the shock.

As a result of the present effort two procedures are now available for coupling the solution obtained on the cascade mesh with that obtained on the local mesh. In the single-pass approach of Refs. 6 and 8 a solution is obtained first on the cascade mesh and then on the local mesh. The velocity potential distribution as determined on the cascade mesh is used to provide outer boundary condition information for the local mesh calculation. The solution to the unsteady boundary-value problem is then taken to be the local solution in the region covered by a local mesh and the cascade solution elsewhere. In this case the local solution is essentially a correction to the cascade solution, and this local correction does not impact the unsteady solution over the entire extended blade-passage region. Thus the single-pass approach assumes that errors in the original cascade mesh solution are confined to the region covered by the local mesh. As we shall see below, this assumption is a reasonable one for subsonic flow, but leads to erroneous predictions for a discontinuous transonic flow.

In the second approach, developed herein, a new composite solution procedure is employed. Here the discrete equations, written separately for the cascade and local meshes are coupled implicitly through special interface conditions, resulting in a single composite system of finite-difference equations that describe the unsteady flow over the entire solution domain, i.e., the union of the cascade and local-mesh domains. The resulting composite system of equations is then solved by direct matrix inversion. This new approach allows the resolution of flow features in one solution domain to influence the solution outside that domain. A detailed description of this procedure and the associated mesh-interface coupling conditions will be given below, but first we will review the mesh nomenclature and the discrete approximations which are common to both the single-pass and composite solution procedures.

4.1 Calculation Meshes

The cascade mesh (see Fig. 4a) is composed of axial lines ($\xi = \text{constant}$) which are parallel to the blade row and tangential curves which are percentile averages of the upper and lower boundaries. Downstream of the blade row the tangential mesh lines coincide with the mean-flow stagnation streamlines. The cascade mesh facilitates the imposition of the blade-to-blade conditions, e.g., $\phi(\vec{X} + m\vec{G}) = \phi(\vec{X})e^{im\sigma}$, and the matching of the analytic and numerical unsteady solutions at the far upstream ($\xi = \xi_-$) and downstream ($\xi = \xi_+$) boundaries of the extended blade-passage solution domain (Fig. 3). However, it does not yield an accurate resolution of the flow near rounded blade edges or near shocks, nor is it well-suited for the accurate implementation of transonic type-dependent differencing procedures.

Thus, a polar-type local mesh (see Fig. 4b) has been employed in Refs. 6 and 8 to resolve the flow around a blunt blade leading edge, in the vicinity of a shock and in the supersonic region adjacent to a blade surface and upstream of the shock. This mesh is composed of radial and circumferential lines, normal and roughly parallel, respectively, to the reference blade surface. The mean shock locus is approximated as a line normal to the mean blade surface which extends out from the point at which the steady shock impinges on this surface.

Under the present effort a new non-orthogonal surface-fitted local mesh has been developed. This mesh is constructed so that for a discontinuous transonic flow one mesh line is aligned with the mean shock locus over the entire length of the shock, thereby leading to a more accurate representation of shock effects. The method of construction of this mesh will be described in detail below. Both local-meshes contain a pair of "radial" lines, positioned at the mean shock location and referred to as the upstream and downstream shock mesh lines. These lines serve to represent information on the upstream and downstream sides of the shock. In the local mesh of Ref. 8 they are placed at the mean location of the shock foot, while in the new local mesh they coincide with the mean shock locus. The upstream and downstream shock mesh lines facilitate the imposition of the unsteady shock-jump conditions.

4.2 Difference Approximations

Algebraic approximations on both the cascade and local mesh to the various linear operators, which make up the unsteady boundary-value problem, are obtained using an implicit, least-squares, interpolation procedure (see Ref. 25). Thus, consider a linear differential operator \mathcal{L} which operates on a constant by multiplying that constant by q^0 . An algebraic approximation, $L\phi$, to $\mathcal{L}\phi$ at the mesh point Q_0 can be written in terms of the values of ϕ at Q_0 and at certain neighboring points, Q_1, \dots, Q_m , which together with Q_0 are called a neighbor set. This approximation can be expressed as

$$(\mathcal{L}\phi)_0 \approx (L\phi)_0 \equiv q^0 \phi_0 + \sum_{m=1}^M \beta_m (\phi_m - \phi_0) \quad (4.1)$$

where the difference coefficients, β_m , are evaluated in terms of a prescribed set of interpolating functions and a set of interpolating coefficients. The latter are determined by a weighted least-squares procedure. The neighbor sets are defined in a "centered" fashion for interior points and in a one-sided fashion for boundary points as shown in Fig. 4. A nine point centered or one-sided difference star is usually employed; however, a one-sided six point star is used at the blade surface in the calculation on the new nonorthogonal local mesh.

When approximating the unsteady field equation, Equation (3.5), one must distinguish between regions of subsonic flow where this equation is elliptic and supersonic flow where it is hyperbolic, and use a differencing scheme which is sensitive to its local character (see Refs. 26 and 27). Thus, at each point of the discrete domain the field equation is expressed in canonical form as

$$\mathcal{L}_0 \phi = (\mathcal{L}_1 + \mathcal{L}_2) \phi \quad (4.2)$$

where

$$\mathcal{L}_1 \phi = A^2(1 - M^2) \phi_{SS} = M^{-2}(1 - M^2)(\Phi_\xi^2 \phi_{\xi\xi} + 2\Phi_\xi \Phi_\eta \phi_{\xi\eta} + \Phi_\eta^2 \phi_{\eta\eta}) \quad (4.3a)$$

and

$$\mathcal{L}_2 \phi = A^2 \phi_{NN} + \dots = M^{-2}[\Phi_\eta^2 \phi_{\xi\xi} - 2\Phi_\xi \Phi_\eta \phi_{\xi\eta} + \Phi_\xi^2 \phi_{\eta\eta}] + \dots \quad (4.3b)$$

Here S and N are local canonical coordinates, i.e., the Cartesian coordinates aligned with and normal to, respectively, the local steady flow direction, and ξ and η (see Fig. 1) are used as computational coordinates. The principal part of the unsteady differential equation is shown explicitly in Equation (4.3), and the dots refer to the remaining terms. The local character of the unsteady differential equation depends on the local steady Mach number, and therefore it is a simple matter to construct a suitable type-dependent differencing scheme.

The linear operator \mathcal{L}_2 is always approximated by a central difference expression, but the difference approximation to the operator \mathcal{L}_1 depends upon the local steady Mach number and hence, on the local type of the unsteady field equation. Thus we set

$$\mathcal{L}_1 \phi|_{i,j} \approx L_1 \phi|_{i,j}, \quad M_{i,j} < 1 \quad (4.4a)$$

and

$$\mathcal{L}_1\phi|_{i,j} \approx L_1\phi|_{i-1,j}, \quad M_{i,j} > 1 \quad (4.4b)$$

where the indices i and j refer to the axial and tangential lines, respectively, of the cascade mesh or the radial and circumferential lines, respectively, of the local mesh, and L_1 is a central difference operator. Therefore at supersonic points the difference approximation to $\mathcal{L}_1\phi$ is retarded along the cascade tangential and the local circumferential mesh lines. The latter are assumed to align closely with the mean flow direction.

Unsteady shock phenomena are captured in the cascade calculation; i.e., the unsteady differential equation is approximated, using either Equation (4.4b) or Equation (4.4a) at the field points immediately upstream or downstream, respectively, of the mean shock location. Shocks are fitted into the local unsteady solution by imposing the jump condition

$$[(i\omega E + F)\phi] + [G\phi_n] + [H\phi_\tau] = 0, \quad (4.5)$$

which follows after combining Equations (3.8a) and (3.8b), at the shock points on the downstream shock mesh line. The functions E , F , G and H in Equation (4.5) depend on the mean flow variables and are given by

$$\begin{aligned} E &= [\bar{\rho}] - M_{-\infty}^2 \bar{\rho}^{(2-\gamma)} \Phi_n[\Phi_n], \\ F &= \frac{\partial}{\partial \tau}([\bar{\rho}]\Phi_\tau) - [\bar{\rho}]\Phi_\tau[\Phi_n]^{-1}[\Phi_{n\tau}], \end{aligned} \quad (4.6)$$

$$G = \bar{\rho}[\Phi_n](1 - M_{-\infty}^2 \bar{\rho}^{(1-\gamma)} \Phi_n^2)$$

and

$$H = \Phi_\tau([\bar{\rho}] - M_{-\infty}^2 \bar{\rho}^{(2-\gamma)} \Phi_n[\Phi_n]) = \Phi_\tau E$$

Equation (4.5) is approximated using one-sided difference expressions (first-order accurate on the upstream or supersonic side and second-order accurate on the downstream or subsonic side) to evaluate the normal derivatives of the unsteady potential at the shock mean position. At those points on the downstream shock mesh line at which the steady flow is continuous (i.e., beyond the end of the shock), the condition $[\phi] = 0$ is imposed. To assist in evaluating the numerical solution procedure, a shock capturing option has also been included in the local unsteady calculation. In this case, the condition $[\phi] = 0$ is imposed at all mesh points on the downstream shock mesh line.

It is important to note that the unsteady shock-jump condition involves jumps in the steady or mean-flow derivatives across the shock. In principle, this information should be available as part of an accurate mean-flow solution, with the jumps in the steady quantities determined as a result of a shock-fitting. However, in practice steady-flow solvers, including the one used in the present effort, employ shock capturing techniques which tend to smear the shock and eliminate the discontinuous changes in the flow quantities. Therefore, care must be taken to restore the required discontinuous steady information into such solutions. In the present effort steady shock-jump information is

determined using a first-order accurate extrapolation of the mean-flow variables from upstream and downstream of the smeared shock to the upstream and downstream sides, respectively, of the estimated mean shock position. The latter is defined as the locus of all points in the smeared shock at which $M = 1$. The errors associated with this approximation have been minimized by using a very dense steady calculation mesh in the vicinity of the shock, thereby reducing the distance over which the shock is smeared.

4.3 Inversion of Cascade and Local Mesh Equations

The systems of linear algebraic equations which approximate the linearized unsteady boundary-value problem on the cascade and local meshes are constructed as described in Refs. 6 and 8. Thus, at a supersonic field point (i, j) the unsteady differential equation is approximated using neighbor sets centered at this point and at the adjacent upstream mesh point $(i-1, j)$. However, at points on the local upstream shock mesh line derivatives tangential to the mean shock locus are evaluated only in terms of information provided along this mesh line to avoid crossing the shock. For points on the downstream shock mesh line either the shock-jump, Equation (4.5) or the continuity, $[\phi] = 0$, condition is approximated as described above. This treatment leads to a block-pentadiagonal system of linear algebraic equations of the form

$$\begin{aligned} C_1\phi_1 + D_1\phi_2 &= F_1 \\ A_i\phi_{i-2} + B_i\phi_{i-1} + C_i\phi_i + D_i\phi_{i+1} + E_i\phi_{i+2} &= F_i, \quad 2 \leq i \leq I-1 \\ B_I\phi_{I-1} + C_I\phi_I &= F_I \end{aligned} \quad (4.7)$$

where ϕ_i is a vector of ϕ -values on the i th cascade axial or local radial mesh line, and the submatrices A_i , B_i , C_i , D_i , and E_i are sparse being mostly scalar tridiagonal. Note that, with the exception of the points on the downstream side of a fitted shock, $A_i = 0$ at subsonic points and $E_i = 0$. With this structure the foregoing system of equations can be solved directly and efficiently using Gaussian elimination.

5. TRANSFINITE LOCAL MESH

One of the objectives of the present study is to develop a more accurate representation of unsteady shock phenomena in the local analysis by imposing the shock-jump conditions at the true predicted mean shock location. There are two possible approaches toward accomplishing this objective. On a mesh constructed without consideration of the mean shock location, an accurate discrete approximation in the vicinity of the shock would require subdividing those mesh cells that contain a segment of the mean shock locus and applying a discrete approximation to the unsteady shock-jump conditions within the subdivided cells. This approach would add a great deal of complexity to the local analysis since it requires tracking the location of the subdivided cells, formulating the jump conditions for a wide variety of possible cell subdivisions, and finally, inverting a system of discrete equations that does not possess a banded structure. However, since the mean shock locus is known from the steady calculation, a much better approach is to require that a local mesh line coincide with the mean shock locus, and subsequently replacing this line with upstream and downstream shock mesh lines. The shock jump relations could then be formulated and imposed along the shock mesh lines resulting in a system of discrete equations having the same block pentadiagonal structure at the shock as in the remainder of the flow field. With this an approach the complexity of modeling the shock in the unsteady analysis is reduced to a problem of mesh generation problem. Consequently, this second approach has been followed in the present study.

A variety of mesh generation techniques are available. Each involves a trade-off between the computational effort required to generate the mesh and the amount of control one has in defining the distribution of mesh points. The following mesh characteristics are important for achieving an accurate local unsteady solution: mesh lines should be clustered near the blade and shock surfaces, the mesh should be nearly orthogonal, and derivatives of the mesh spacings should vary smoothly. For transonic unsteady applications there is the additional constraint that one mesh line should coincide with the mean shock location. Unlike the other requirements which primarily deal with the mesh distribution along the outer boundaries of the local mesh domain, this new requirement imposes a constraint within the interior of the local mesh.

In view of the foregoing requirements we have employed a direct algebraic mesh generation scheme using a transfinite or multivariate interpolation to construct the local mesh. This allows for a great deal of control in distributing mesh points and for a convenient means of constraining the mesh so that it will conform to one or more internal boundaries. Further, it has been found to be very efficient in terms of both the storage requirements and the amount of computation time required to generate the mesh. Finally, this approach can be easily extended to satisfy additional constraints. A good description of algebraic mesh generation techniques, including the method of transfinite interpolation, is given in Ref. 28. In the present effort the generalized transfinite interpolation procedure described in Ref. 29 has been used.

In the remainder of this section we provide a brief outline of the principles of transfinite interpolation. This is followed by a detailed description of the application of these princi-

ples to the generation of local surface-fitted meshes which conform to a single embedded shock surface. The extension to multiple embedded shock surfaces is straightforward, but will not be considered here.

5.1 Interpolation Procedure

The theory of transfinite interpolation described by Eriksson (Ref. 29) is based on a very general form of multivariate interpolation. In two dimensions we consider a function $f(u, v) = [x(u, v), y(u, v)]$ where the parameters u and v are defined over the rectangular region $u_1 \leq u \leq u_p$ and $v_1 \leq v \leq v_q$. The function f is assumed to be known on certain lines, $u = u_k$ and $v = v_k$, i.e.,

$$f(u_k, v) = a_k(v) \quad k = 1, 2, \dots, p$$

and

$$f(u, v_k) = b_k(u) \quad k = 1, 2, \dots, q$$

Further, if desired, it can be assumed that one or more normal derivatives of f are known on these lines, i.e.,

$$\frac{\partial^n}{\partial u^n} f(u_k, v) = a_k^{(n)}(v) \quad \text{for } k = 1, 2, \dots, r, \quad n = 1, 2, \dots, p_k$$

and

$$\frac{\partial^n}{\partial v^n} f(u, v_k) = b_k^{(n)}(u) \quad \text{for } k = 1, 2, \dots, s, \quad n = 1, 2, \dots, q_k$$

To interpolate between the given lines we define a set of univariate blending functions $\alpha_k^{(n)}(u)$, $k = 1, 2, \dots, r$, $n = 0, 1, 2, \dots, p_k$ and $\beta_k^{(n)}(v)$, $k = 1, 2, \dots, s$, $n = 0, 1, 2, \dots, q_k$ which satisfy the conditions

$$\frac{\partial^m}{\partial u^m} \alpha_k^{(n)}(u_\ell) = \delta_{k\ell} \delta_{nm} \quad \text{and} \quad \frac{\partial^m}{\partial v^m} \beta_k^{(n)}(v_\ell) = \delta_{k\ell} \delta_{nm}, \quad (5.3)$$

where $\delta_{k\ell} = 1$ for $k = \ell$ and $\delta_{k\ell} = 0$ for $k \neq \ell$. Using transfinite interpolation, the function $f(u, v)$ can be expressed in the form

$$f(u, v) = f_1(u, v) + \sum_{k=1}^r \sum_{n=0}^{p_k} \beta_k^{(n)}(v) [b_k^{(n)}(u) - \frac{\partial^n}{\partial v^n} f_1(u, v_k)] , \quad (5.4)$$

where

$$f_1(u, v) = \sum_{k=1}^r \sum_{n=0}^{p_k} \alpha_k^{(n)}(u) a_k^{(n)}(v) \quad (5.5)$$

This function defines a transformation from the rectangular region $u_1 \leq u \leq u_p$, $v_1 \leq v \leq v_q$ in (u, v) space to some arbitrarily shaped region in (x, y) space. While this transformation can be expressed as a single equation, Equations (5.4) and (5.5) are used to illustrate that it can be viewed as a series of univariate interpolations in the u and v directions, respectively. Each step in this series can be viewed as the application of a projection operator which projects the function f between known lines.

The transfinite interpolation procedure outlined above can be viewed as providing an efficient mapping from a uniform rectilinear mesh in u, v -space to a curvilinear mesh spanning a region of arbitrary shape in x, y -space. Control over the distribution of mesh points is governed by the number of initial data lines ($u_i = \text{constant}$ or $v_i = \text{constant}$), the choice of which normal derivatives of f , if any, are to be specified on these lines, the specified values of f and its derivatives along these lines, and the choice of blending functions between the initial data lines. For most applications it is sufficient to limit the initial data lines to the lines bounding the mesh domain, e.g., the outer mesh boundaries and the blade surface. In this case control over the mesh distribution is achieved by defining the distribution of mesh points along the outer boundary (definition of f) and by specifying any number of normal derivatives at these points. Such an approach can be applied directly to generate a local mesh for unsteady subsonic flow. For a discontinuous transonic flow the foregoing procedure must be extended to include an additional interior line ($v = \text{constant}$) that represents the mean shock locus.

5.2 Mesh Generation Procedure

To generate a shock conforming local mesh we first prescribe the region to be covered. This domain is then divided into two subregions separated by a line that coincides with the mean shock locus and is referred to herein as the shock line. Next the mesh point distributions around the outer boundary of local mesh region and along the shock line are defined. Finally, the transfinite interpolation procedure is used to determine the mesh within the local region.

For example, a typical local mesh domain is shown in Fig. 5a. The extent of this domain is defined in terms of starting (v_1) and ending (v_3) lines which are constructed normal to the blade surface (u_1). The outer "circumferential" boundary (u_2) is defined as the locus of points at a fixed normal distance from the blade surface and lying between the radial lines v_1 and v_3 . The "radial" and circumferential extents of the local region are chosen so that this region contains the mean shock locus, the supersonic region upstream of the shock and any important flow features due to blade surface geometry. The resulting local mesh region is then subdivided using a third line (v_2) which coincides with the mean shock locus and extends from the end of the shock to the outer boundary u_2 . The mesh boundary lines v_1 , v_3 , u_1 and u_2 are also used as the initial data lines in the transfinite interpolation procedure. In the (u, v) plane (see Fig. 5b) the blade surface and the outer circumferential boundary are taken as two $u = \text{constant}$ initial data lines (note there are no internal $u = \text{constant}$ data lines). In the other coordinate direction the two bounding data lines, v_1 and v_3 , and the internal data line, v_2 , are specified. These correspond to the radial starting line, the shock line, and the radial ending line (defined as $v = \text{constant}$ initial data lines).

A mesh point distribution is defined along each of the data lines as follows. Along the blade surface (u_1) a one-dimensional blending function which is weighted in terms of blade surface curvature and distance from the foot of the shock is used. This blending function is tailored to allow a clustering of mesh points in regions of high blade curvature

and near the shock with a smooth variation in the mesh spacings between these regions. Along the outer boundary (u_2) a similar blending function provides clustering of mesh points in the vicinity of the shock line. Along the starting line (v_1), shock line (v_2) and ending line (v_3) the mesh is exponentially clustered toward the blade surface. The mapping function $f(u, v)$ in Equation (5.1) is then determined by assuming that the mesh spacing is uniform in the u, v -plane. To allow for more control of the mesh distributions near and along the blade surface boundary, we also impose approximate expressions for the first three normal derivatives of f (see Equation (5.2)). It is not possible to provide an exact specification of these derivatives since the function mapping the u, v -plane onto the x, y -plane is known only along certain lines within the domain. Thus, following Eriksson (Ref. 29) the normal derivatives are modeled by assuming that a good approximation to these derivatives is obtained by representing the blade locally as an ellipse. For an ellipse defined by the equation $x^2 + y^2/e^2 = a^2$ these derivatives are given by

$$\begin{aligned}\frac{\partial x}{\partial u} &= kex, & \frac{\partial y}{\partial u} &= \pm k\sqrt{a^2 - x^2} \\ \frac{\partial^2 x}{\partial u^2} &= k^2x, & \frac{\partial^2 y}{\partial u^2} &= \pm k^2e\sqrt{a^2 - x^2} \\ \frac{\partial^3 x}{\partial u^3} &= k^3ex \quad \text{and} \quad \frac{\partial^3 y}{\partial u^3} &= \pm k^3\sqrt{a^2 - x^2},\end{aligned}\tag{5.6}$$

where the scaling factor k determines the concentration of mesh points near the surface. In practice the constants e and a may be varied smoothly so that a nearly orthogonal mesh is obtained near the blade. Normal derivatives are not specified along the remaining boundary lines (u_2, v_1, v_2 , and v_3).

With the appropriate boundary lines specified and initial data defined along these lines the transfinite interpolation operator of Equations (5.4) and (5.5) takes the form

$$\begin{aligned}f(u, v) &= f_1(u, v) + \beta_1(v)(f(u, v_1) - f_1(u, v_1)) + \beta_2(v)(f(u, v_2) - f_1(u, v_2)) \\ &\quad + \beta_3(v)(f(u, v_3) - f_1(u, v_3))\end{aligned}\tag{5.7}$$

and

$$\begin{aligned}f_1(u, v) &= \alpha_1(u)f(u_1, v) + \alpha_1^{(1)}(u)\frac{\partial}{\partial u}f(u_1, v) \\ &\quad + \alpha_1^{(2)}(u)\frac{\partial^2}{\partial u^2}f(u_1, v) + \alpha_1^{(3)}(u)\frac{\partial^3}{\partial u^3}f(u_1, v) + \alpha_2(u)f(u_2, v)\end{aligned}\tag{5.8}$$

At this point a suitable set of blending functions α_k and β_k for the interpolations in the u and v directions must be defined. Since these functions are only required to satisfy conditions at certain discrete points, there are an infinite number of possible functions

from which to choose. In the present study we have found that the following functions give good mesh distributions

$$\begin{aligned}\alpha_1(u) &= 1 - G(u), \quad \alpha_1^{(1)}(u) = u - G(u), \quad \alpha_1^{(2)}(u) = \frac{1}{2}u^2 - \frac{1}{2}G(u) \\ \alpha_1^{(3)}(u) &= \frac{1}{6}u^3 - \frac{1}{6}G(u), \quad \alpha_2(u) = G(u)\end{aligned}\tag{5.9}$$

and

$$G(u) = \frac{e^{k_2 u} - 1 - k_2 u - (k_2 u)^2/2 - (k_2 u)^3/6}{e^{k_2} - 1 - k_2 - k_2^2/2 - k_2^3/6}.$$

For $v_1 \leq v \leq v_2$

$$\begin{aligned}w &= \frac{v - v_1}{v_2 - v_1}, \quad \beta_2(v) = (1 - w)w^{k_3} + w(1 - (1 - w)^{k_4}), \\ \beta_1(v) &= 1 - \beta_2(v) \quad \text{and} \quad \beta_3(v) = 0\end{aligned}\tag{5.10}$$

For $v_2 \leq v \leq v_3$

$$w = \frac{v - v_2}{v_3 - v_2}, \quad \beta_1(v) = 0,$$

$$\beta_3(v) = (1 - w)w^{k_4} + w(1 - (1 - w)^{k_5}) \quad \text{and} \quad \beta_2(v) = 1 - \beta_3(v)$$

After substituting these expressions into Equations (5.7) and (5.8) one obtains the final expression for the transfinite interpolation operator. The constants k_2 , k_3 , k_4 and k_5 in the above expressions allow control of mesh line clustering near the blade and shock surfaces.

6. COMPOSITE SOLUTION PROCEDURE

In recent years we have seen a rapid development of embedded or composite mesh solution procedures for the accurate resolution of geometrically complex flow problems. The basic premise behind such approaches is that current discrete approximations and solution algorithms have been demonstrated and verified for a wide range of model problems. Therefore, the application of these prediction methods to realistic flow situations reduces to a problem of mesh generation. Attempts to generate suitable meshes often meet with conflicts between desired qualities. Turbomachine cascades provide an excellent example of this conflict since upstream and downstream of the cascade a periodic mesh is desirable, while near a blade surface a dense nearly orthogonal body-conforming mesh gives the most accurate results. One solution is to decompose a geometrically complex flow field into one or more simpler zones. Meshes of different topologies may then be generated within each zone to satisfy the desired local constraints. The overall flow solution would then be determined as a composite of the solutions in each of the one or more zones. The key to obtaining such composite solutions is the development of procedures for matching solutions across zones.

In general, solution procedures for composite mesh structures can be classified as one of two types—multigrid procedures (see Refs. 30–33) or zonal procedures (Refs. 34–36). In the multigrid approach, the composite mesh is constructed as a series of increasingly finer meshes usually of a similar topology (i.e., one or more local meshes embedded in a global mesh structure) with the finest levels existing only in local regions of the flow field. The coupling of the solutions within the different embedded regions is accomplished using a multigrid solution algorithm. In the zonal approach, solutions in different mesh zones are patched together through the application of interface conditions at zonal mesh boundaries. Different mesh topologies are often used in different zones and adjoining meshes either butt together or overlap. There may be a global mesh with one or more embedded local mesh regions or simply a patchwork of different mesh zones.

The mesh structure used in the present unsteady analysis consists of a combination of a global cascade mesh and a local body fitted mesh. Since these meshes differ topologically, a zonal solution procedure for overlapping meshes is the favored approach. Thus, the composite mesh is constructed by overlaying the cascade and local meshes. In the region of intersection of the two meshes (i.e., the region covered by the local zone) we eliminate all cascade points except those which fall within a predefined overlap zone which is adjacent to the outer boundary of the local mesh. The resulting composite mesh structure is shown schematically in Fig. 6. The unsteady potential equation, Equation (3.5), is approximated at each point of the cascade mesh which lies outside the inner boundary of the overlap zone and at each point of the local mesh. Special coupling conditions are imposed at the cascade mesh points that lie within the overlap zone and at the local mesh points lying on the outer boundary of the local region.

The majority of the zonal schemes for overlapping meshes presented in the literature employ iterative or relaxation type solution procedures both within each mesh zone and as the mechanism for coupling the solutions in the various zones. The coupling is imple-

mented by interpolating the solution within one zone to the boundary of an adjoining zone. These boundary values are then frozen during the iterations in the latter zone. By cycling periodically through all mesh zones a globally converged result is achieved. The success of such an approach is dependent on the convergence rate of the relaxation scheme used in each zone, which for classical relaxation methods requires that the discrete equation system for each zone be diagonally dominant. In the present application the discrete systems for the cascade- and local-mesh zones are, in general, not diagonally dominant due to the discrete representations of the boundary conditions. For this reason these systems are solved directly using Gaussian elimination. As noted in the previous section, the determination of a solution on a single mesh (cascade or local) using this approach is straightforward and very efficient because of the banded structure of the difference equations.

The composite cascade/local discrete equation system does not possess a banded structure because of the coupling conditions required to join the solutions in the different mesh zones. Although the banded structure is lost, the composite system of equations is very sparse. Therefore, it is possible to conveniently store and efficiently solve such a system by adopting a general sparse matrix representation for the coefficient matrix. Here, only the non-zero elements of the matrix and their corresponding location in the full matrix are stored. For the present application we use the Yale Sparse Matrix Format described in Refs. 37 and 38. This format allows us to take advantage of an existing set of routines for manipulating and inverting large unstructured matrices, and results in a very efficient solution procedure for the composite-mesh system of unsteady equations.

In the remainder of this section we will describe the formulation and assembly of the composite equation system including the coupling conditions. This will be followed by a brief description of the Yale Sparse Matrix Format and Gaussian Elimination routines. In the following sections of this report we will demonstrate the composite solution procedure for selected unsteady subsonic and transonic flows. To illustrate the importance of using the composite solution procedure, which allows the accurate resolution of flow features in the local mesh region to impact the global cascade solution, we will compare the present composite solutions with those obtained using the single-pass or local-correction solution procedure of Refs. 6 and 8.

6.1 Composite-Mesh Equations

To construct the composite system of discrete equations for the linearized unsteady problem, it is convenient to first identify mesh points as either cascade-mesh solution points, local-mesh solution points, cascade-mesh coupling points or local-mesh coupling points. This classification is based upon where the cascade and local mesh points lie relative to a prescribed overlap zone. The latter is defined conveniently in terms the local mesh indices by stepping in n cells from the outer boundary of the local mesh, as shown in Fig. 7a. As presently implemented the width of the overlap zone can be different along different segments of the outer boundary of the local mesh. Once the overlap zone is specified, cascade mesh points are classified as being solution points if

they lie exterior to the interior boundary of the overlap zone (i.e., the outer boundary of the local mesh region) or as coupling points if they lie within two mesh points from the interior boundary of the overlap zone. The two mesh point range on the latter class allows for an upwind difference approximation to be applied at the cascade solution points lying near the outer boundary of the local region. The remaining points of the cascade mesh are eliminated resulting in the mesh shown in Fig. 7b. Similarly, those local mesh points lying within the outer boundary of the local mesh are classified as solution points and those on this outer boundary are called coupling points. Upon combining the cascade and local solution and coupling points we obtain the composite mesh shown in Fig. 6.

At cascade and local solution points the discrete approximations to the unsteady equations are determined as described for the cascade and local meshes, respectively, in §4. Thus the block tri- or pentadiagonal structure of Equation (4.7) is preserved at cascade mesh and local mesh solution points. The discrete equations at cascade mesh coupling points are determined as follows. For each coupling point we locate the corresponding local mesh cell which contains this point. This local cell is then triangulated on the shortest diagonal. Within the triangle containing the cascade mesh coupling point a bilinear interpolation operator is constructed to define the value of the unsteady potential at the cascade mesh coupling point in terms of its values at three surrounding local mesh points making up the triangle. For example, if the cascade coupling point was found to be located in a triangle defined by points (i, j) , $(i + 1, j)$ and $(i, j + 1)$ on the local mesh, this operator would be expressed as follows:

$$\phi_{I,J} = W_1\phi_{i,j} + W_2\phi_{i,j+1} + W_3\phi_{i+1,j} ,$$

where

$$\begin{aligned} W_1 &= [(y_{i+1,j} - y_{i,j+1})(x_{i,j+1} - x_{I,J}) - (x_{i+1,j} - x_{i,j+1})(y_{i,j+1} - y_{I,J})]/\Delta , \\ W_2 &= 1 + [(y_{i+1,j} - y_{i,j+1})(x_{i,j+1} - x_{I,J}) - (x_{i+1,j} - x_{i,j+1})(y_{i,j+1} - y_{I,J})]/\Delta , \\ W_3 &= -[(y_{i,j} - y_{i,j+1})(x_{i,j+1} - x_{I,J}) - (x_{i,j} - x_{i,j+1})(y_{i,j+1} - y_{I,J})]/\Delta , \end{aligned} \quad (6.1)$$

and

$$\Delta = (x_{i+1,j} - x_{i,j+1})(y_{i,j} - y_{i,j+1}) - (x_{i,j} - x_{i,j+1})(y_{i+1,j} - y_{i,j+1}) .$$

Here the upper case subscripts, I and J , are cascade mesh indices and lower case subscripts, i and j , are local mesh indices.

A similar interpolation operator is constructed to relate the unsteady potential at each local mesh coupling point to its values at points which define the cascade mesh cell enclosing the coupling point. In this case, since one family of cascade mesh lines is parallel, the following four point bilinear interpolation operator is used:

$$\phi_{i,j} = W_1\phi_{I,J} + W_2\phi_{I,J+1} + W_3\phi_{I+1,J+1} + W_4\phi_{I+1,J} ,$$

$$W_1 = (1 - W_x)(1 - W_y), \quad W_2 = (1 - W_x)W_y, \quad W_3 = W_xW_y, \quad \text{and} \quad W_4 = W_x(1 - W_y)$$

$$\begin{aligned}
W_x &= (x_{i,j} - x_{I,J}) / (x_{I+1,J} - x_{I,J}) \\
W_y &= (y_{i,j} - y_A) / (y_B - y_A) \\
y_A &= (1 - W_x)y_{I,J} + W_x y_{I+1,J} \\
y_B &= (1 - W_x)y_{I,J+1} + W_x y_{I+1,J+1}
\end{aligned} \tag{6.2}$$

The inclusion of these coupling equations into the system of discrete equations destroys the previous block pentadiagonal structure. Although each coupling equation involves points which are spatially close to the coupling point under consideration, the former are not necessarily neighbors in the composite equation system. Therefore, the final system of discrete equations contains a coefficient matrix whose band width is much greater than five. Consequently special storage and inversion techniques are required to achieve an efficient solution.

6.2 Inversion of Composite Equation System

There has been a significant amount of research in recent years directed toward developing efficient storage and solution techniques for linear systems of equations that contain large unstructured sparse coefficient matrices. The composite set of discrete equations for the linearized unsteady problem falls into this class. The approach taken to solve such systems is to first recast the large sparse matrix into a compact vector description (or sparse matrix format) where only non-zero elements of the original matrix and one or more pointer vectors are stored. The sparse matrix format is defined so as to minimize storage requirements while maximizing the computational efficiency of matrix manipulations (e.g., multiplication, transposition, inversion, etc.). General routines for performing these matrix manipulations are written in terms of the sparse matrix description. For the present application we have employed a sparse matrix package developed by Eisenstat, et. al. (Refs. 37, 38) at Yale University. This work has been assembled into a package of routines call the Yale Sparse Matrix Package, with each routine written in the Yale Sparse Matrix Format. Its use allows us to take advantage of a vast development effort and places us in a position to implement future improvements. Since the original Yale package was written for real equations, it was necessary under the present effort to extend this package for the solution of complex equation systems.

Once the composite system of unsteady equations is cast into the appropriate format, it can be solved using the very efficient Gaussian elimination routine contained in the Yale package. Here the Gaussian elimination is broken down into two steps. First a symbolic factorization of the original matrix is performed based on its sparsity pattern and then used to efficiently invert the matrix. If the sparsity pattern is the same from one solution to the next, the symbolic factorization need only be performed once and stored for future use. Since the sparsity pattern in the present unsteady analysis is determined by the composite mesh structure and the steady flow properties, the symbolic factorization must only be performed one time for parametric studies involving changes only in the frequency, interblade phase angle or mode of the blade motion. After inversion, the discrete solution for the unsteady potential is transferred from the Yale sparse matrix representation to

the corresponding cascade and local mesh points for evaluation of unsteady aerodynamic response parameters.

7. DEMONSTRATION OF SOLUTION PROCEDURES

Our purpose in this section is to demonstrate the effects of implementing the transfinite or shock-conforming local mesh and the composite-mesh solution procedure into the linearized unsteady aerodynamic analysis of Refs. 6 and 8. We will restrict our consideration to unsteady flows, excited by prescribed small-amplitude harmonic blade motions, through a two-dimensional compressor ($M_{-\infty} \leq M_{\infty}$) cascade operating at subsonic inlet and exit conditions. The example cascade has a stagger angle, Θ , of 45° and a gap/chord ratio, G , of unity. The blades are constructed by superposing the thickness distribution of a modified NACA four-digit series airfoil on a circular-arc camber line. The thickness distribution, $T(x)$, is given by

$$T(x) = H_T[2.969x^{1/2} - 1.26x - 3.516x^2 + 2.843x^3 - 1.036x^4], \quad 0 \leq x \leq 1. \quad (7.1)$$

where H_T is the nominal blade thickness. The coefficient of the x^4 term in Equation (7.1) differs from that used in the standard airfoil definition (i.e., -1.015) so that the example blades close in wedge-shaped trailing edges. The camber distribution is given by

$$C(x) = H_C - R + [R^2 - (x - 0.5)^2]^{1/2}, \quad 0 \leq x \leq 1, \quad (7.2)$$

where H_C (> 0) is the height at midchord and $R = (2H_C)^{-1}(H_C^2 + 0.25)/2$ is the radius of the circular-arc camber line. Thus, the surface coordinates for the reference ($m = 0$) blade are given by

$$[X, Y]_{B,\pm} = [x \mp 0.5T(x) \sin \theta, C(x) \pm 0.5T(x) \cos \theta], \quad 0 \leq x \leq 1, \quad (7.3)$$

where $\theta = \tan^{-1}(dC/dx)$. For the present application we set $H_T = 0.06$ and $H_C = 0.05$ to study the unsteady aerodynamic response to a vibrating cascade of cambered NACA 0006 airfoils.

We consider two different uniform inlet operating conditions. In one case the inlet Mach number, $M_{-\infty}$, and flow angle, $\Omega_{-\infty}$, are 0.7 and 55° , respectively; in the other, $M_{-\infty} = 0.8$ and $\Omega_{-\infty} = 58^\circ$. The steady flows through the cascade are assumed to satisfy a Kutta condition at blade trailing edges and therefore, only inlet uniform-flow information must be specified. For $M_{-\infty} = 0.7$ and $\Omega_{-\infty} = 55^\circ$, the mean or steady flow through the cascade is entirely subsonic; for $M_{-\infty} = 0.8$ and $\Omega_{-\infty} = 58^\circ$, it is transonic with a single normal shock occurring in each blade passage. The predicted blade-surface Mach number distributions, as determined using the full-potential analysis of Ref. 19 in which shocks are captured in transonic calculations, are shown in Fig. 8. The subsonic mean flow stagnates on the pressure surface of the blade at $x = 0.0005$ and the Mach number reaches a maximum value of 0.916 on the suction surface at $x = 0.109$. The exit Mach number and flow angle are 0.446 and 40.2° , respectively. The transonic flow stagnates at $x = 0.002$ on the pressure surface and the normal shock emanates from the suction surface at $x = 0.258$. The Mach numbers at the base of the shock are 1.282 on the upstream side and 0.816 on the downstream side, and the exit Mach number and flow angle are 0.432 and 40.3° , respectively.

Predictions are given below for the unsteady aerodynamic response at the reference ($m = 0$) blade surface including first harmonic unsteady pressure differences, i.e., $\Delta p(x) = p_B(x, y_-) - p_B(x, y_+)$, unsteady aerodynamic moments, m_P , and, where appropriate, shock displacements, $r_{sh,B}$, for blades undergoing pure pitching (torsional) oscillations about their midchord points, i.e., $X_P, Y_P = 0.5, 0$. These motions are assumed to occur at unit frequency, $\omega = 1$, an interblade phase angle σ of 180 degrees and a complex amplitude α of $(1, 0)$. Predicted unsteady potential contours will also be presented to illustrate unsteady solutions over extended blade-passage domains. Note that if $Im\{\alpha\} = 0$, the real and imaginary parts of a reference blade complex response parameter represent the response components that are in- and out-of-phase, respectively, with the reference blade displacement.

The linearized unsteady flow solutions were determined on an H -type cascade mesh and on transfinite and polar local meshes. The H -type mesh consisted of 100 axial lines $\xi = \text{constant}$ which are parallel to the blade row and 30 tangential curves which lie at percentile averages of the "circumferential" distances between the upper and lower boundaries of the extended blade-passage solution domain. This mesh extended from one axial chord upstream to one axial chord downstream from the blade row (i.e., $-1 \leq \xi / \cos \Theta \leq 2$). For the most part uniform mesh spacings were used with $\Delta \xi = 0.04 \cos \Theta$ and $\Delta \eta = 4\%$ of the distance along axial lines between the upper and lower boundaries, but axial mesh lines were concentrated near blade edges and over the first 30 percent of blade chord where axial spacings of $\Delta \xi = 0.01 \cos \Theta$ were used. Tangential lines were concentrated near the upper and lower boundaries, i.e., near the blades and their wakes, of the solution domain. The small axial mesh spacings over the forward 30 percent of the blades were used in an effort to capture shock phenomena with the H -mesh calculation.

The local meshes consisted of 12 circumferential and 100 "radial" lines. The former wrapped around the leading edge of the reference blade and extended from radial lines emanating from the upper and lower surfaces of the blade at $\xi = 0.5 \cos \Theta$. The radial lines extended outward from the airfoil to one-half the minimum distance (i.e., the throat) between adjacent blades. The circumferential lines were concentrated near the blade surface and the radial lines were concentrated near a shock, if present.

7.1 Single-Pass Solutions

Response predictions based on the single-pass solution procedure are shown in Figs. 9-11. These results were obtained from three different unsteady calculations: (a) a cascade mesh calculation, (b) a single-pass calculation using the polar-type local mesh and (c) a single-pass calculation using the transfinite local mesh. Shock phenomena are captured in the cascade mesh calculation, i.e., the field equation, Equation (3.5), is solved throughout the interior of the extended blade-passage solution domain. The local-mesh transonic results shown in Fig. 10 have also been determined by shock capture; i.e., by requiring that the unsteady potential be continuous ($[\phi] = 0$) at the shock in the local calculation. The local-mesh transonic results reported in Fig. 11 have been determined by shock fitting; i.e., by imposing the unsteady shock-jump condition, Equation (4.5), in

the local mesh calculation.

The response predictions for the subsonic ($M_\infty = 0.7$, $\Omega_\infty = 55$ deg) NACA 0006 cascade shown in Fig. 9 reveal that the unsteady flow in the neighborhood of the rounded blade leading edge cannot be predicted properly using the cascade mesh alone. Indeed, the cascade-mesh pressure-difference predictions are erroneous over approximately the first ten percent of blade chord. A local-mesh calculation greatly reduces such errors and predicts an analytic behavior for Δp in the vicinity of the leading edge in which both the real and imaginary components of the pressure difference are zero at the leading edge point and reach local extrema very close (i.e., at approximately $x = 0.004$) to this point. The two local solutions yield nearly identical pressure differences, but there are discrepancies close to the leading edge. The transfinite local-mesh calculation gives the better solution because it provides the better mesh point distribution in the immediate vicinity of the blade leading edge. Note, however, that the unsteady moments predicted by the two single-pass calculations are in close agreement.

Response predictions for the transonic ($M_\infty = 0.8$, $\Omega_\infty = 58$ deg) NACA 0006 cascade are shown in Figs. 10 and 11. The local solutions reported in Fig. 10 have been determined by shock capture. Hence, the velocity potential is continuous across the shock and the motion of the shock is neglected. Note however, that since we evaluate unsteady pressures at a shock using one-sided difference approximations, our shock-captured pressure differences will be discontinuous at shocks. For the transonic example the cascade-mesh calculation fails to provide an accurate resolution of the flow both in the vicinity of the blade leading edge and in the vicinity of the normal shock which impinges on the blade suction surface at $x = 0.258$. Although the cascade mesh used was rather dense with $\Delta\xi = 0.01 \cos \Theta$ over the first thirty percent of blade chord, the unsteady flow in the vicinity of the shock and in the supersonic region upstream of the shock cannot be resolved accurately because the axial lines of the cascade mesh are highly skewed relative to the shock. The local-mesh allows a much more accurate resolution of both unsteady leading edge and shock phenomena, as is indicated by the results depicted in Figs. 10b and 10c. Except for small differences near the blade leading edge and near the root of the shock, both the polar and transfinite local meshes provide very similar single-pass pressure difference predictions. Thus, although the radial lines of the transfinite local mesh conform more closely to the mean-shock position, this feature does not seem to offer an important advantage in a single-pass calculation in which the unsteady potential is assumed to be continuous across shocks.

Response predictions for the transonic NACA 0006 cascade based on single-pass calculations in which shocks are fitted, i.e., the shock-jump condition is imposed in the local calculation, are shown in Fig. 11. Here, the cascade mesh result is identical to that shown in Fig. 10 and has been included only for the reader's convenience. If shocks are fitted, the unsteady potential will be discontinuous at the mean shock location. The relative displacement of a shock along a blade surface and hence, the shock induced unsteady airloads depend upon the jump in the unsteady potential at the shock root. As seen by a comparison of the first harmonic pressure difference distributions given in Figs. 10 and 11,

the condition imposed at a shock has a strong impact on the single-pass predictions for the unsteady surface pressures downstream of the shock. The shock-captured and shock-fitted unsteady solutions yield pressure differences that are in close agreement upstream but differ substantially downstream of the mean shock location. This occurs because the mechanism for allowing physical information downstream of a shock to impact a solution upstream of a shock is very limited in a single-pass calculation.

Although the pressure differences downstream of the shock differ substantially, the shock-fitted (Fig. 11) and the shock-captured (Fig. 10) unsteady moment predictions are in fairly close agreement. Recall that the shock-fitted unsteady solution yields both harmonic and anharmonic local unsteady responses, but that the anharmonic loads are neglected in a shock-captured calculation. However, the first-order global unsteady airloads predicted by both solutions are harmonic. The results shown in Figs. 10 and 11 indicate that if shock motions are neglected in the unsteady calculation, the first-harmonic unsteady pressures downstream of the shock will compensate for the missing anharmonic shock load.

The two local solutions considered in Fig. 11 give slightly different unsteady pressure differences downstream of the shock and significantly different shock-displacements along the blade surface. These differences indicate the great sensitivity of a discontinuous unsteady transonic solution to the numerical modeling of the shock. Since the "radial" lines of the transfinite local mesh conform to the mean shock locus, it is to be expected that this mesh should provide the better solution for a discontinuous transonic flow.

Unsteady potential contours for the example subsonic and transonic NACA 0006 cascades are shown in Figs. 12 and 13, respectively. These contours were determined from single-pass calculations using the transfinite local mesh. The shock-jump condition (4.5) was imposed in the transonic calculation. In the single-pass procedure the solution on the cascade mesh fixes the values of ϕ on the outer boundary of the local mesh. Thus, the potential contours will be continuous at this boundary but, in general, their slopes will be discontinuous. These discontinuities are indicative of errors being present in a single-pass solution. Slope discontinuities are apparent in the potential contours shown in Figs. 12 and 13, particularly in the contours shown in Fig. 13 for the unsteady transonic flow.

At this point we have demonstrated several aspects of the numerical solution procedure. In particular, we have illustrated the improvements in unsteady flow resolution near rounded blade leading edges and near shocks that can be achieved using a local mesh calculation. In addition, the effects of imposing the shock-jump condition (4.5) in the local unsteady calculation have been demonstrated. A comparison of the single-pass shock fitted and shock captured unsteady solutions shows that the local unsteady aerodynamic response downstream of a shock is profoundly influenced by the conditions imposed at the shock. Finally, single-pass solutions obtained using polar and transfinite local meshes have been presented for subsonic, continuous transonic and discontinuous transonic flows. The two local meshes yield very similar response predictions for the subsonic and continuous transonic examples, but somewhat different predictions for the

discontinuous transonic example. Such differences are to be expected since the transfinite mesh has been constructed and implemented so that mean shock phenomena could be modeled more accurately in linearized unsteady calculations.

7.2 Composite Solutions

With the single-pass solution procedure the detailed resolution of the flow in the local mesh region cannot impact the solution over the remainder of the extended blade passage solution domain. As we shall see, this places a serious limitation on the accuracy of single-pass calculations, particularly for transonic flows in which shocks extend well into the blade passage. In contrast, with the composite solution procedure the cascade- and local-mesh finite-difference equations are solved simultaneously, thereby allowing the accurate resolution of the flow in the local region to impact the entire unsteady solution.

Unsteady potential contours determined from composite solutions for the example subsonic and transonic NACA 0006 cascade are shown in Figs. 14 and 15, respectively. The transfinite local mesh was used in both calculations and shock jump conditions were imposed in the transonic calculation. The composite calculations yield potential contours that have continuous slopes at the outer boundary of the local mesh. This is an indication that errors inherent to the single-pass procedure are eliminated using the composite-mesh solution procedure. A comparison of the single-pass (Fig. 12) and composite (Fig. 14) potential contours for the subsonic cascade indicates that the two procedures yield very similar unsteady flow fields with the composite procedure predicting a somewhat greater variation in the potential upstream of the blade row. However, a similar comparison of the single-pass (Fig. 13) and composite (Fig. 15) potential contours for the transonic cascade reveals that there are dramatic differences between the results obtained from the two procedures. In particular, the composite-mesh solution gives much greater variations in the potential upstream and downstream of the shock and in the region upstream of the blade row. The latter are caused by a propagating acoustic response disturbance. The composite solution yields a response disturbance of much greater amplitude than the single-pass solution. The results in Figs. 13 and 15 indicate that the detailed resolution of the unsteady flow in the vicinity of a shock can have a profound effect on the flow throughout the extended blade-passage solution domain.

Unsteady pressure difference distributions for the subsonic NACA 0006 cascade as determined from composite solutions on the polar and transfinite local meshes are shown in Figs. 16a and 16b, respectively. A comparison of these with the corresponding single-pass predictions shown in Figs. 9b and 9c reveals that the differences between the single-pass and composite predictions for the subsonic unsteady pressure difference distributions are small and occur primarily near the leading edge of the blade. Consequently, the differences between the single-pass and composite predictions for the unsteady aerodynamic moment are rather large. The differences between the polar and transfinite local mesh composite predictions for the unsteady pressure differences and the unsteady moment are quite small and mirror those between the corresponding single-pass predictions.

Although a composite calculation will provide a more accurate resolution of an un-

steady subsonic flow than a single-pass calculation, it appears that the two procedures will predict very similar overall unsteady flow properties. Also, composite subsonic solutions determined on the polar and transfinite local meshes will show only small quantitative differences. For a transonic flow, however, composite and single-pass predictions can differ rather dramatically as indicated by the potential contours shown in Figs. 13 and 15. Substantial differences between composite solutions determined on the polar and transfinite local mesh will also occur as we shall see below.

Unsteady pressure difference distributions for the transonic NACA 0006 cascade as determined from composite solutions on the polar and transfinite local meshes are shown in Figs. 17 and 18. The results in Fig. 17 have been determined by shock capture; those in Fig. 18, by shock fit. A comparison of the two composite solutions depicted in Fig. 17 with the corresponding single-pass solutions depicted in Fig. 10 shows that the composite and single-pass procedures yield qualitatively similar unsteady pressure differences. However, the influence of the shock is much more pronounced in the composite results. The shock-captured composite solutions on the polar (Fig. 17a) and transfinite (Fig. 17b) local meshes give very similar unsteady pressure difference and unsteady aerodynamic moment predictions.

In contrast, there are dramatic differences between the results of the shock-fitted composite (Fig. 18) and single-pass (Fig. 11) solutions and between the results of the shock-fitted polar and transfinite local mesh composite solutions. These occur because the composite procedure allows the motion of the shock to influence the predicted unsteady flow field over the entire extended blade passage domain, whereas the single-pass procedure limits the effect of the shock motion to the local mesh domain. Note that for the blade motion considered ($\omega = 1$, $\sigma = 180$ deg) the shock displacement excites a relatively large amplitude acoustic response disturbance far upstream of the blade row (see Fig. 15).

The single-pass and composite calculations on the polar local mesh provide qualitatively similar unsteady pressure difference behaviors along the blade, but the composite calculation predicts enhanced shock effects. However, the single-pass and composite calculations on the transfinite local mesh yield very different behaviors for the out-of-phase component of the unsteady pressure difference both upstream and downstream of the shock. There are also dramatic differences between the single-pass and composite predictions for the unsteady aerodynamic moments and relative shock displacements.

The shock-fitted (Fig. 18) and shock-captured (Fig. 17) composite unsteady moment predictions differ to a much greater extent than the corresponding (Figs. 11 and 10, respectively) single-pass predictions. This suggests that it is important to fit shocks in a composite solution scheme to properly predict unsteady airloads. Also the differences between the composite solutions on the polar and transfinite local meshes (Fig. 18) again suggest the sensitivity of the linearized unsteady solution to the numerical modeling of shock effects. Since the shock mesh lines of the polar local mesh do not coincide with the mean shock position, shock phenomena are more accurately modeled using a transfinite local mesh calculation.

In this section we have attempted to demonstrate the merits of using a composite solution procedure and a transfinite local mesh to resolve linearized unsteady subsonic and transonic cascade flows. For subsonic flow, a comparison of composite solutions on a transfinite local mesh and single-pass solutions on a polar local mesh, i.e., the new and the old solution procedures, respectively, indicates that the two procedures predict very similar overall unsteady flow fields and blade pressure difference distributions, $\Delta p(x)$. However, the predicted Δp distributions differ in the vicinity of a blade leading edge, and therefore give rise to quite different unsteady aerodynamic moment predictions. For transonic flow, the composite procedure allows the detailed resolution of the flow near a shock to impact the predicted unsteady field throughout the entire solution domain — a feature missing from the single-pass procedure. Consequently, a comparison of composite and single-pass unsteady transonic solutions shows that shock phenomena are much more important than previously indicated by single-pass solutions.

Transonic composite solutions are quite sensitive to the physical conditions imposed at a shock and to the numerical modeling of these conditions. Our results indicate that it is important to fit shocks in unsteady transonic solutions and to represent shock phenomena as accurately as possible. Thus, the implementation of a transfinite local mesh in which radial lines conform to the shape of the mean shock locus is a step in the right direction. Unfortunately, the nonlinear full potential solution (Ref. 19) used to provide the steady background flow information for our unsteady transonic calculations was obtained using a single-pass calculation on a polar local mesh in which shocks are captured. In the future, an effort should be made to develop a cascade full potential analysis with transfinite local mesh and composite mesh solution capabilities in which shocks are fitted into steady solutions.

8. GLOBAL UNSTEADY AERODYNAMIC RESPONSE BEHAVIOR

We proceed to examine the global unsteady aerodynamic response behavior of the subsonic and transonic NACA 0006 cascades. For purposes of comparison, we will also consider two flat-plate cascades. These have the same stagger angle ($\Theta = 45$ deg) and blade spacing ($G = 1$) and operate at the same inlet Mach numbers as the subsonic ($M_\infty = 0.7$) and transonic ($M_\infty = 0.8$) NACA 0006 cascades. However, the mean positions of the flat-plate blades are aligned with the inlet free stream direction (i.e., $\beta_\infty = 45$ deg), and therefore the steady flows through the flat plate cascade are uniform, i.e., $M = M_\infty$, where M is the local steady Mach number.

We will restrict our consideration to unsteady flows excited by prescribed single-degree-of-freedom, small-amplitude, harmonic blade motions. These include pure translations (bending) normal to blade chord with $h_y = (1, 0)$ and pure rotations (torsion) about an axis at midchord, i.e., $X_P, Y_P = 0.5, 0$ with $\alpha = (1, 0)$. The stability of the translations normal to blade chord depends upon the sign of the out-of-phase component of the normal or lift force. Thus, for example, if $Im\{f_y\} > 0$, the airstream supplies energy to the blade motion and this motion is unstable according to linearized theory. Similarly, the stability of the rotational blade motions depends upon the sign of the out-of-phase moment. These motions are unstable if $Im\{m_p\} > 0$ (Ref. 39).

The aerodynamic response at a moving blade surface is tied to the far-field acoustic response produced by the blade motion. For this reason blade motions are often classified according to the different types of far-field acoustic response behavior that they produce (Ref. 20). For example, blade motions are classified as subresonant if all acoustic response disturbances attenuate with increasing axial distance from the blade row and as superresonant (m, n) if m and n such disturbances persist in the far upstream and far downstream regions, respectively, and carry energy away from the blade row. A blade motion that produces at least one acoustic response disturbance in either the far upstream or far downstream region that persists and carries energy parallel to the blade row is said to be resonant. A resonant blade motion produces a far-field acoustic response disturbance that travels at circumferential wave number $\kappa_\eta = G^{-1}\sigma_{\mp\infty}^\mp$, where the subscripts refer to the far upstream ($-\infty$) or far downstream ($+\infty$) regions of the flow, and the superscripts indicate that there are two resonance conditions associated with each of these regions. If the mean flow is uniform, then the upstream and downstream resonant interblade phase angles are identical, i.e., $\sigma^\mp = \sigma_{-\infty}^\mp = \sigma_{+\infty}^\mp$, and the same number of acoustic response disturbances will persist in both the far upstream and the far downstream regions, i.e., $m = n$.

For the example subsonic NACA 0006 cascade the resonant interblade phase angles (in degrees) are $\sigma_{-\infty}^- = -26.93\omega$, $\sigma_{-\infty}^+ = 117.12\omega$, $\sigma_{+\infty}^- = -31.80\omega$ and $\sigma_{+\infty}^+ = 59.79\omega$. For the transonic configuration they are $\sigma_{-\infty}^- = -28.94\omega$, $\sigma_{-\infty}^+ = 201.7\omega$, $\sigma_{+\infty}^- = -35.92\omega$ and $\sigma_{+\infty}^+ = 66.22\omega$. The NACA 0006 blade motions at interblade phase angles lying between the lowest ($\sigma_{+\infty}^-$) and highest ($\sigma_{-\infty}^+$) resonant interblade phase angles, except those at $\sigma = \sigma_{-\infty}^-$ and $\sigma = \sigma_{+\infty}^+$ are superresonant. If the range $\sigma_{-\infty}^+ - \sigma_{+\infty}^-$ exceeds 360 deg, then the blade motions at all interblade phase angles, except $\sigma = \sigma_{\mp\infty}^\mp \pm 360n$ deg,

where $n = 0, \pm 1, \pm 2, \dots$, are superresonant. The resonant conditions for the flat-plate cascade operating at $M_\infty = 0.7$ are $\sigma^- = -29.41\omega$ and $\sigma^+ = 107.26\omega$; for the flat-plate cascade operating at $M_\infty = 0.8$ they are $\sigma^- = -32.97\omega$ and $\sigma^+ = 177.02\omega$.

Global unsteady response predictions are presented below over an interblade phase angle range extending from -90 deg to 270 deg to minimize the artificial breaks in the curves that would occur over the superresonant regions of blade vibration. Note that blade motions at $\sigma \pm 360n$ deg produce identical unsteady aerodynamic responses. The NACA 0006 response predictions were determined from composite mesh solutions to the linearized unsteady boundary-value problem. These solutions were determined using a transfinite local mesh and by imposing the shock-jump condition, Equation (4.5), in the unsteady transonic calculations. The flat-plate predictions were obtained from solutions on the cascade mesh alone. The meshes used were as described in §7, except that the cascade mesh contained only 84 axial lines. Since, for our present purposes, we did not have to resolve shock phenomena in the cascade mesh calculation, there was no need to pack axial mesh lines over the forward thirty percent of blade chord. Axial mesh lines were concentrated near blade edges, however, because the cascade mesh was the only one used for the flat-plate solutions. The uniform spacings between axial and tangential mesh lines cited in §7 are sufficiently small so that the acoustic response disturbances produced by unsteady excitations at frequencies up to 2 could be resolved accurately over the entire range of interblade phase angles.

Unsteady lift and moment predictions for pure bending and pure torsional motions of the flat-plate and NACA 0006 cascades are shown in Figs. 19 and 20. The out-of-phase lift responses to pure bending vibrations at $M_\infty = 0.7$ and $\omega = 1.0$ and at $M_\infty = 0.8$ and $\omega = 0.5$ are considered in Fig. 19; the out-of-phase moments due to pure torsional vibrations at $M_\infty = 0.7$ and $\omega = 1.5$ and at $M_\infty = 0.8$ and $\omega = 1.0$ in Fig. 20. The vertical lines above and below the curves in these figures indicate the interblade phase angles at which the NACA 0006 and flat-plate blade motions, respectively, produce a resonant far-field acoustic response disturbance. Note that abrupt changes in the global unsteady aerodynamic response behavior occur at the resonant interblade phase angles.

The flat-plate blade motions considered in Figs. 19 and 20 are subresonant for $\sigma \in [-90 \text{ deg}, \sigma^-)$ and $\sigma \in (\sigma^+, 270 \text{ deg}]$ and superresonant (1,1) for $\sigma \in (\sigma^-, \sigma^+)$. The NACA 0006 motions are subresonant for $\sigma \in [-90 \text{ deg}, \sigma_{+\infty}^-)$ and $\sigma \in (\sigma_{-\infty}^+, 270 \text{ deg}]$, superresonant (0,1) for $\sigma \in (\sigma_{+\infty}^-, \sigma_{-\infty}^-)$, superresonant (1,1) for $\sigma \in (\sigma_{-\infty}^-, \sigma_{+\infty}^+)$, and superresonant (1,0) for $\sigma \in (\sigma_{+\infty}^+, \sigma_{-\infty}^+)$. Both the flat-plate and NACA 0006 motions are stable, i.e., $Im\{f_v\} < 0$ for the pure bending motions (Fig. 19) and $Im\{m_p\} < 0$ for the pure torsional motions (Fig. 20). With the exception of the blade motions at interblade phase angles near the resonance conditions, the nonuniform mean flow effects associated with the NACA 0006 cascade are generally destabilizing. Note that such effects produce substantial differences between the NACA 0006 and flat-plate moment responses to the subresonant torsional motions at $M_\infty = 0.7$ and $\omega = 1.5$ and at $M_\infty = 0.8$ and $\omega = 1.0$.

Predictions for the out-of-phase lift due to bending vibrations of the flat-plate and NACA 0006 blades at frequencies, ω , of 0.5, 1.0, 1.5 and 2.0 are shown in Figs. 21 and 22,

respectively. Results for the out-of-phase moment due to torsional blade vibrations at these frequencies are shown in Figs. 23 and 24. Although the curves in Figs. 21 through 24 show reasonable trends with increasing vibration frequency, they also reveal the rather complicated aerodynamic response behavior associated with vibrating cascades. To a great extent, this results from the different far-field acoustic response behaviors produced by the different types of blade motion (i.e., subresonant, superresonant (1,0), etc.). Note that for $M = 0.8$ the flat-plate blade motions at $\omega = 2$ and $\sigma = \sigma^+ - 360 \text{ deg} = -5.96 \text{ deg}$ produce resonant acoustic response disturbances far upstream and downstream of the blade row. In this case the flat-plate blade motions are superresonant (2,2) for $\sigma(\sigma^-, \sigma^+ - 360 \text{ deg})$ and superresonant (1,1) at the other non-resonant interblade phase angles. Similarly, the transonic NACA 0006 blade motions at $\omega = 1.5$ and $\sigma = \sigma_{-\infty}^+ - 360 \text{ deg} = -57.45 \text{ deg}$ and at $\omega = 2.0$ and $\sigma = \sigma_{-\infty}^+ - 360 \text{ deg} = 43.4 \text{ deg}$ produce resonant acoustic response disturbances (with $\kappa_\eta = \sigma_{-\infty}^+$) far upstream of the blade row. At $M_\infty = 0.8$ and $\omega = 1.5$ the superresonant NACA 0006 blade motions produce at most one propagating acoustic response disturbance far upstream of the blade row; however, at $\omega = 2$ the superresonant blade motions at $\sigma(\sigma_{-\infty}^-, \sigma_{-\infty}^+ - 360 \text{ deg})$ produce two propagating acoustic response disturbances in the far upstream region.

The bending motions considered in Figs. 21 and 22 are stable and the stability margin generally increases with increasing vibration frequency. The non-resonant bending vibrations of the subsonic NACA 0006 blades at the three lower frequencies usually have smaller stability margins than the corresponding (i.e., $M = 0.7$) flat-plate vibrations. This trend does not apply to the bending motions at $\omega = 2$, where there is a range of interblade phase angles $\sigma(\sigma_{-\infty}^+, \sigma_{-\infty}^- + 360 \text{ deg})$ over which the stability margin for the NACA 0006 bending motions is much greater than that for the flat plate motions. In particular, over this range the lift forces opposing the bending motions of the NACA 0006 blades are quite substantial. At the higher Mach number, $M_\infty = 0.8$, the bending motions of the transonic NACA 0006 cascade generally have a greater stability margin than those of the corresponding flat-plate cascade for $\sigma < \sigma_{+\infty}^+$, and at $\omega = 1.5$ and $\omega = 2.0$ for $\sigma > \sigma_{+\infty}^+$. The NACA 0006 blades have a smaller stability margin than the flat-plate blades for $\sigma_{-\infty}^- \lesssim \sigma \lesssim \sigma_{+\infty}^+$, and at the two lower frequencies, $\omega = 0.5$ and $\omega = 1.0$, for $\sigma_{+\infty}^+ \lesssim \sigma \lesssim \sigma_{-\infty}^-$. There are substantial differences between the lift responses of the two cascades when $\omega = 1.5$ or $\omega = 2.0$ and $\sigma_{+\infty}^+ \lesssim \sigma \lesssim \sigma_{-\infty}^- + 360 \text{ deg}$, where the NACA 0006 blade motions are superresonant (1,0) and the flat-plate motions are, for the most part, superresonant (1,1).

The moment responses to the pure torsional motions of the flat-plate (Fig. 23) and NACA 0006 (Fig. 24) blade motions also indicate that the stability margin generally increases with increasing frequency. Or, stated more precisely, the stability margin generally increases with increasing frequency when the motions at a given interblade phase angle are of the same type, i.e., subresonant, superresonant (1,1), etc. The moment responses to the torsional blade motions of the subsonic ($M_\infty = 0.7$) and transonic ($M_\infty = 0.8$) NACA 0006 cascades generally lie closer to the stability boundary ($\text{Im}\{m_p\} = 0$) than the moment responses to the motions of the corresponding flat-plate

cascades. However, a torsional motion of the transonic NACA 0006 cascade at $\omega = 0.5$ and an interblade phase angle in the vicinity of $\sigma_{-\infty}^+$ produces a large moment that opposes the blade motion. This somewhat surprising result is due to the large shock loads that are predicted for the torsional vibrations at $\omega = 0.5$ and σ near $\sigma_{-\infty}^+$ of the transonic NACA 0006 cascade.

Recall that for a discontinuous transonic flow there are two contributions to each global unsteady airload, one arising from the first harmonic unsteady surface pressure response and the other from the anharmonic unsteady surface pressures associated with shock motions. The out-of-phase components of the shock loads produced by the motions of the transonic NACA 0006 cascade are shown in Fig. 25. In particular, the out-of-phase unsteady lift, i.e., $Im\{f_{y,sh}\} = Im\{r_{sh,B}\}([P_B]\vec{n}_B) \cdot \vec{e}_y$, is shown in Fig. 25a for pure bending vibrations at $\omega = 0.5, 1.0, 1.5$ and 2.0 , and the out-of-phase unsteady moment, i.e., $Im\{m_{p,sh}\} = -Im\{r_{sh,B}\}([P_B] \cdot \vec{R}_P \cdot \vec{\tau}_B)_{sh}$, in fig. 25b for pure torsional vibrations at these frequencies. For the example transonic NACA 0006 cascade, the jump in the steady pressure, $[P_B]$, as felt by an observer moving across the shock in the counterclockwise (or $\vec{\tau}-$) direction is -0.477 at the foot of the shock. The lift and moment due to the shock displacement are given by $f_{y,sh} = -0.474r_{sh,B}$ and $m_{p,sh} = -0.111r_{sh,B}$, respectively, where $r_{sh,B}$ is the shock displacement along the blade surface in the $\vec{\tau}-$ direction. The results in Fig. 25 reveal that the shock loads can be quite severe and that they have a destabilizing effect on pure bending and pure torsional vibrations over a broad range of frequencies and interblade phase angles.

Curves for the unsteady lift (Fig. 22b) and unsteady lift due to shock motion (Fig. 25a) show similar behaviors for the bending motions at $\omega = 0.5$. At the three higher frequencies such curves show substantially different behaviors, particularly for interblade phase angles lying between the resonant values $\sigma = \sigma_{+\infty}^+$ and $\sigma = \sigma_{-\infty}^+$. Similarly, the curves for the unsteady moment (Fig. 24b) and the unsteady moment due to shock displacement (Fig. 25b) show similar behaviors at $\omega = 0.5$ and $\omega = 1.0$, but the curves for the two higher frequencies show very different behaviors, again particularly for $\sigma \in (\sigma_{+\infty}^+, \sigma_{-\infty}^+)$. Such trends indicate that shock loads tend to dominate the global unsteady aerodynamic response at lower vibration frequencies.

9. CONCLUDING REMARKS

The linearized unsteady aerodynamic analysis described in this report accounts for the effects of real blade geometry, mean blade loading and operation at transonic Mach numbers on the unsteady aerodynamic response to the vibrations of an isolated two-dimensional cascade. Here, the unsteady flow is regarded as a small perturbation of a fully nonuniform isentropic and irrotational mean or steady flow. Thus, the steady flow is determined as a solution of a full-potential boundary-value problem and the linearized unsteady flow as a solution of a time-independent linear variable-coefficient boundary-value problem in which the coefficients depend on the underlying steady flow. The steady and unsteady problems can be solved sequentially to determine the mean and fluctuating components, respectively, of the fluid dynamic properties throughout a required solution domain, i.e., a single extended blade passage region of finite extent in the axial-flow direction.

Unsteady linearizations relative to nonuniform steady flows offer great potential for meeting the needs of aeroelastic designers for efficient unsteady aerodynamic analyses that contain the essential physics of complex turbomachinery flows. However, it has been recognized (Refs. 1 and 2) that before this potential can be fully realized, significant improvements in numerical solution procedures for both the steady and linearized unsteady flows are needed, so that reliable response information can be provided for the wide range of geometric configurations and flow conditions at which blade vibrations are of practical concern. Some needed capabilities include the ability to predict transonic flows (i.e., subsonic flows with embedded supersonic regions) through compressor and fan-type cascades operating at positive or negative mean incidence, supersonic flows with complex moving shock patterns and the high frequency unsteady flows driven by incident entropic, vortical and acoustic excitations.

The work described in the present report contributes to the numerical analysis of linearized unsteady flows around compressor blades operating at high subsonic inlet Mach number and high mean incidence. In particular, two major advances to the existing numerical analysis of Refs. 6 and 8 have been provided. One involves the construction and implementation of a new transfinite local mesh so that unsteady shock phenomena can be modeled more accurately; the other, the development of a composite mesh solution procedure so that the detailed resolution of the local flow field can impact the unsteady solution over an entire extended blade-passage domain.

The transfinite local mesh is constructed so that "radial" lines conform to mean shock positions, which are determined from a nonlinear steady solution. This feature allows an accurate imposition of the unsteady shock-jump conditions and therefore an accurate determination of unsteady shock loads. We also find that because of the mesh control allowed by the transfinite interpolation procedure, the transfinite local mesh yields a better resolution of unsteady phenomena in the vicinities of rounded blade leading edges than the polar local mesh used in previous work.

The composite solution procedure eliminates major weaknesses inherent to the single-pass solution procedure described in Refs. 6 and 8. In the latter the cascade and local

mesh equations are solved separately with the cascade mesh solution establishing the potential distribution on the outer boundary of the local mesh. Thus, the boundary-condition information employed in the local calculation is inaccurate. Also, there is no mechanism for the detailed local solution to affect the unsteady solution beyond the local mesh domain. In contrast, with the composite procedure the cascade and local mesh equations are solved simultaneously. This allows an accurate resolution of the flow over the entire extended blade-passage solution domain, and, in particular, the high flow gradients in the local region to impact the entire unsteady solution. The composite approach is particularly important for transonic flows in which shocks extend well into blade passages. An added benefit associated with the composite procedure is that there is no need to pack cascade mesh lines in the vicinities of blade leading edges or shocks since the cascade-mesh solution is not used to establish a boundary condition for the local mesh calculation. Thus, uniform spacings, which are determined based on a knowledge of the acoustic response in the far field (see Ref. 20), can be prescribed in constructing a cascade mesh to be used in a composite solution procedure.

The numerical results presented in this report illustrate various features of the linearized unsteady aerodynamic analysis. The results for the NACA 0006 cascade presented in §7 indicate the improved resolution of unsteady phenomena at blade leading edges and at shocks that can be achieved using a local mesh calculation. They also demonstrate the importance of using a composite mesh solution procedure especially for a discontinuous transonic flow and the sensitivity of the overall unsteady solution to the physical and numerical modeling of shock effects. The results for the NACA 0006 and flat-plate cascades presented in §8 illustrate, to a limited extent, the effects of nonuniform mean flow phenomena on global unsteady aerodynamic response behavior. In particular, these results indicate that nonuniform mean flow effects tend to destabilize blade motions that occur at the frequencies typical of those at which subsonic positive incidence flutter is encountered. Also, the shock loads produced by single-degree-of-freedom vibrations of the NACA 0006 blades are destabilizing for a broad range of frequencies and interblade phase angles.

The development and implementation of the transfinite local mesh and the composite mesh solution capability are important advances in our ability to predict linearized unsteady cascade flows. However, additional improvements are still needed. More robust full potential analyses are required so that nonlinear steady transonic calculations will converge more rapidly, and so that steady flows through fans operating at non-zero mean incidence can be predicted (see also Refs. 11 and 13). Also, in view of the relative importance of unsteady shock loads and the sensitivity of linearized unsteady flow solutions to the numerical modeling of shock effects, procedures for determining nonlinear steady solutions with fitted shocks should be developed. Finally, it is anticipated that more realistic predictions for shock locations and shock displacements (Ref. 40) could be achieved if the nonisentropic effects associated with shocks were incorporated into cascade nonlinear steady and linearized unsteady potential flow analyses.

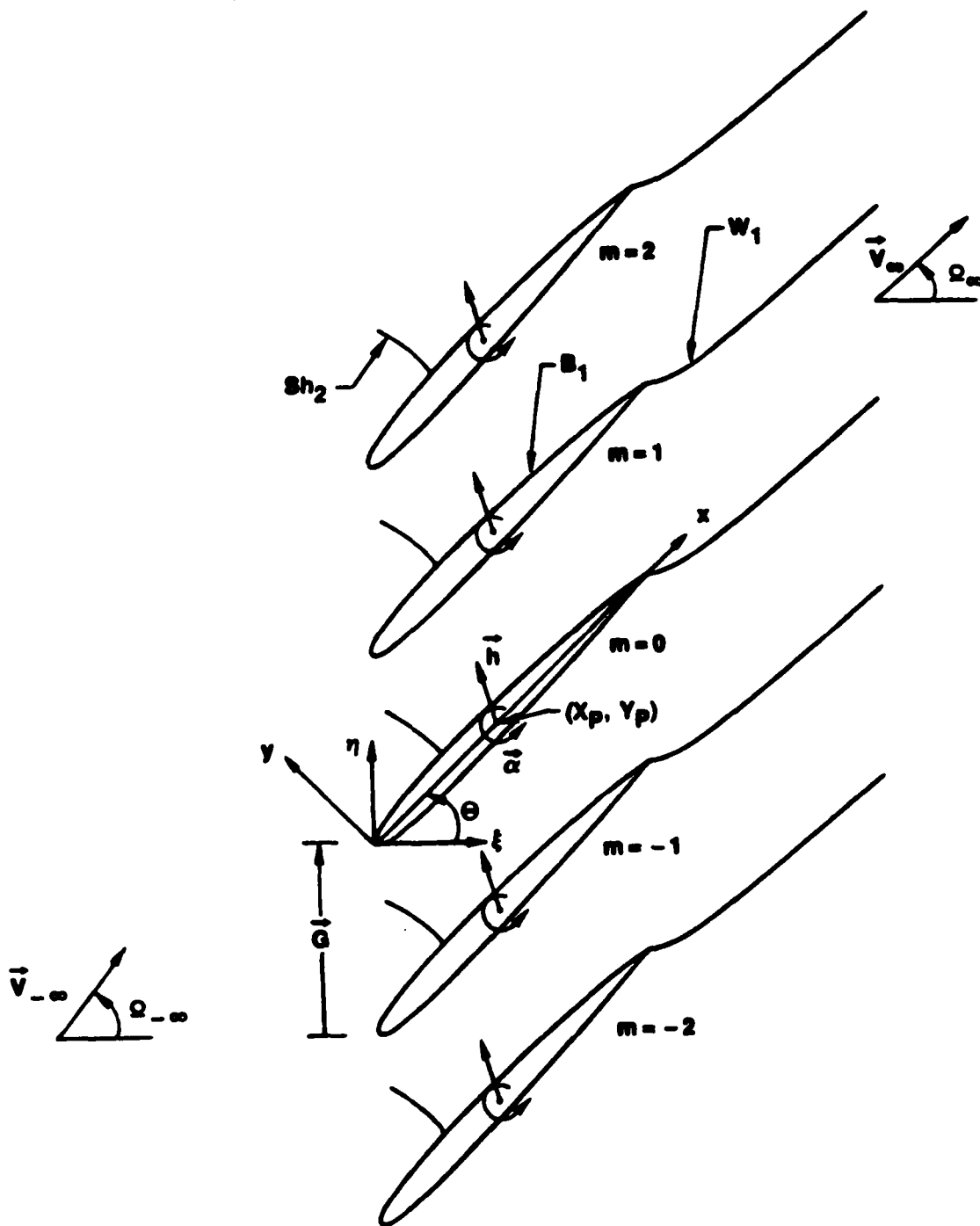


Figure 1. Two-dimensional vibrating transonic compressor cascade; $M_\infty < M_\infty < 1$.

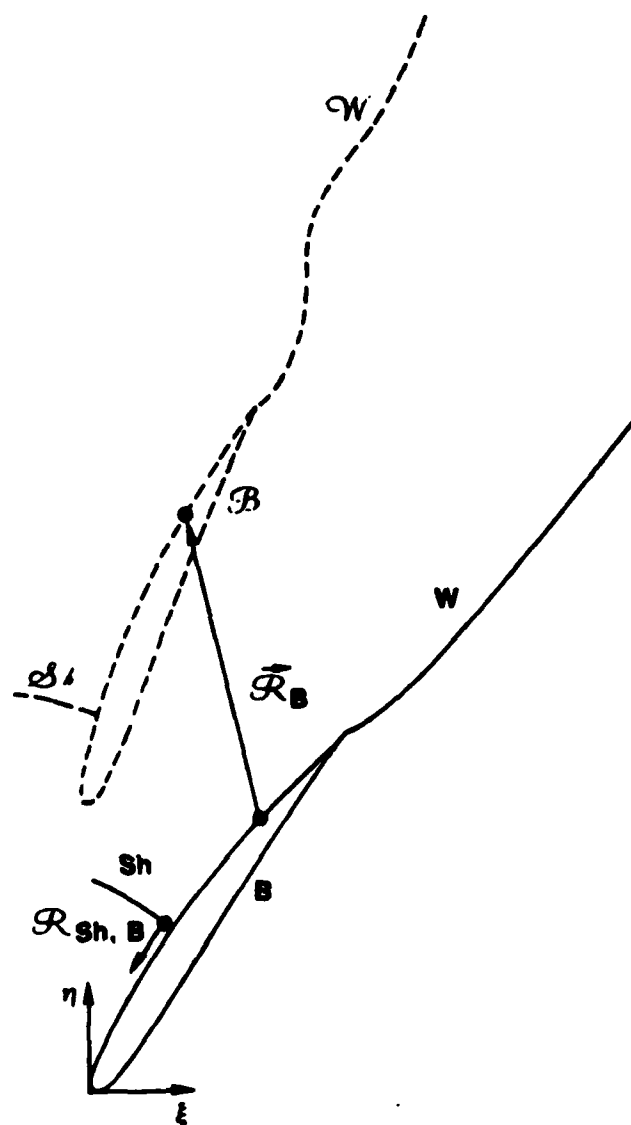


Figure 2. Steady state, ———, and instantaneous, - - - -, blade, wake and shock mean positions.

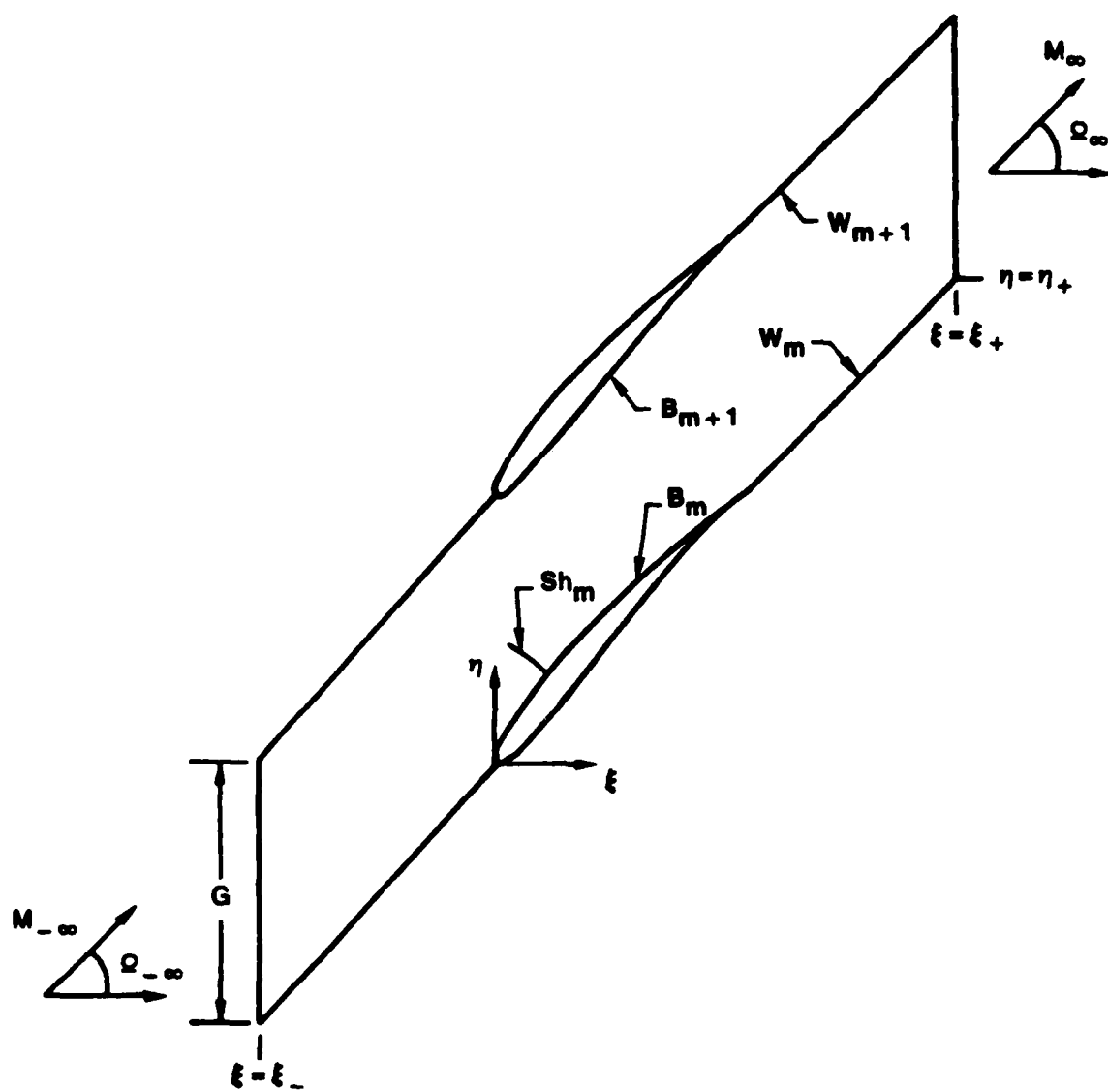


Figure 3. Numerical solution domain: extended blade-passage region of finite extent.

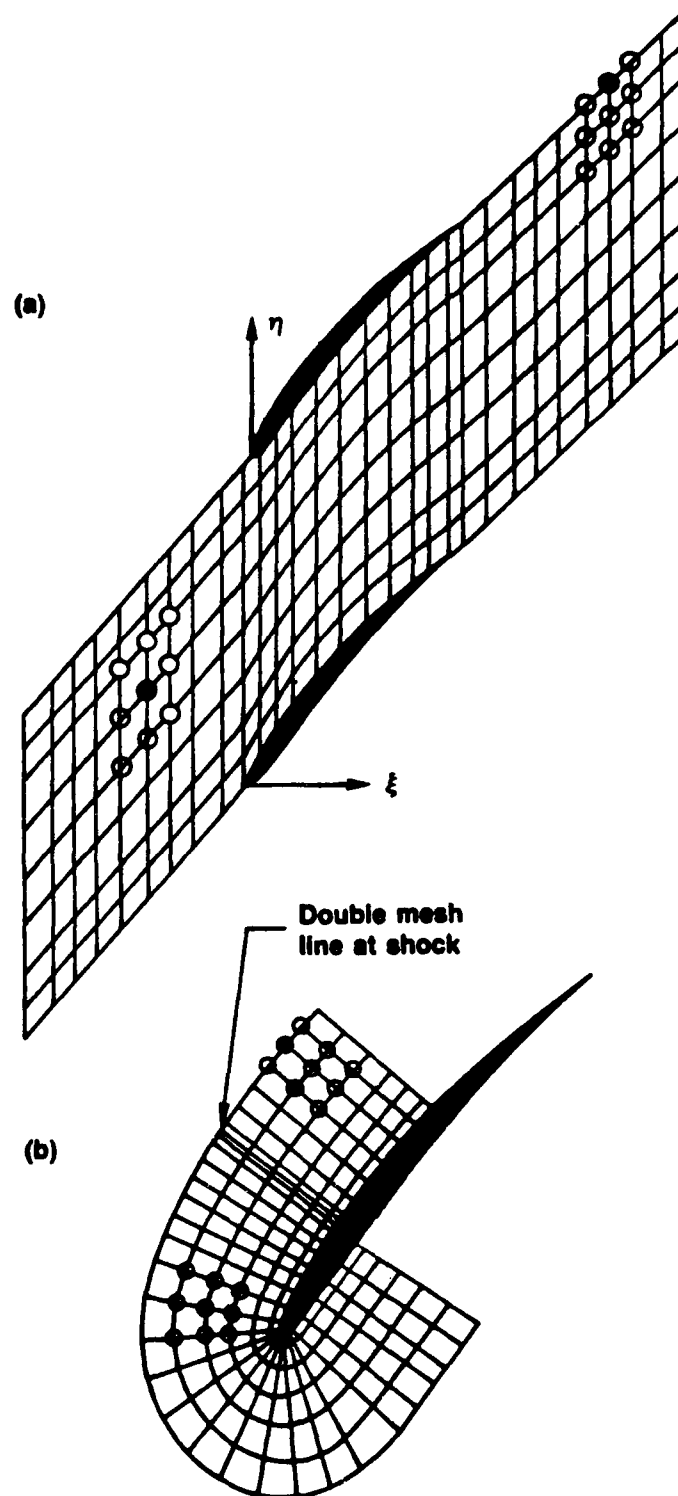


Figure 4. Calculation meshes for unsteady cascade flows: (a) cascade mesh; (b) polar-type local mesh: ● calculation point; ○ neighbor point.

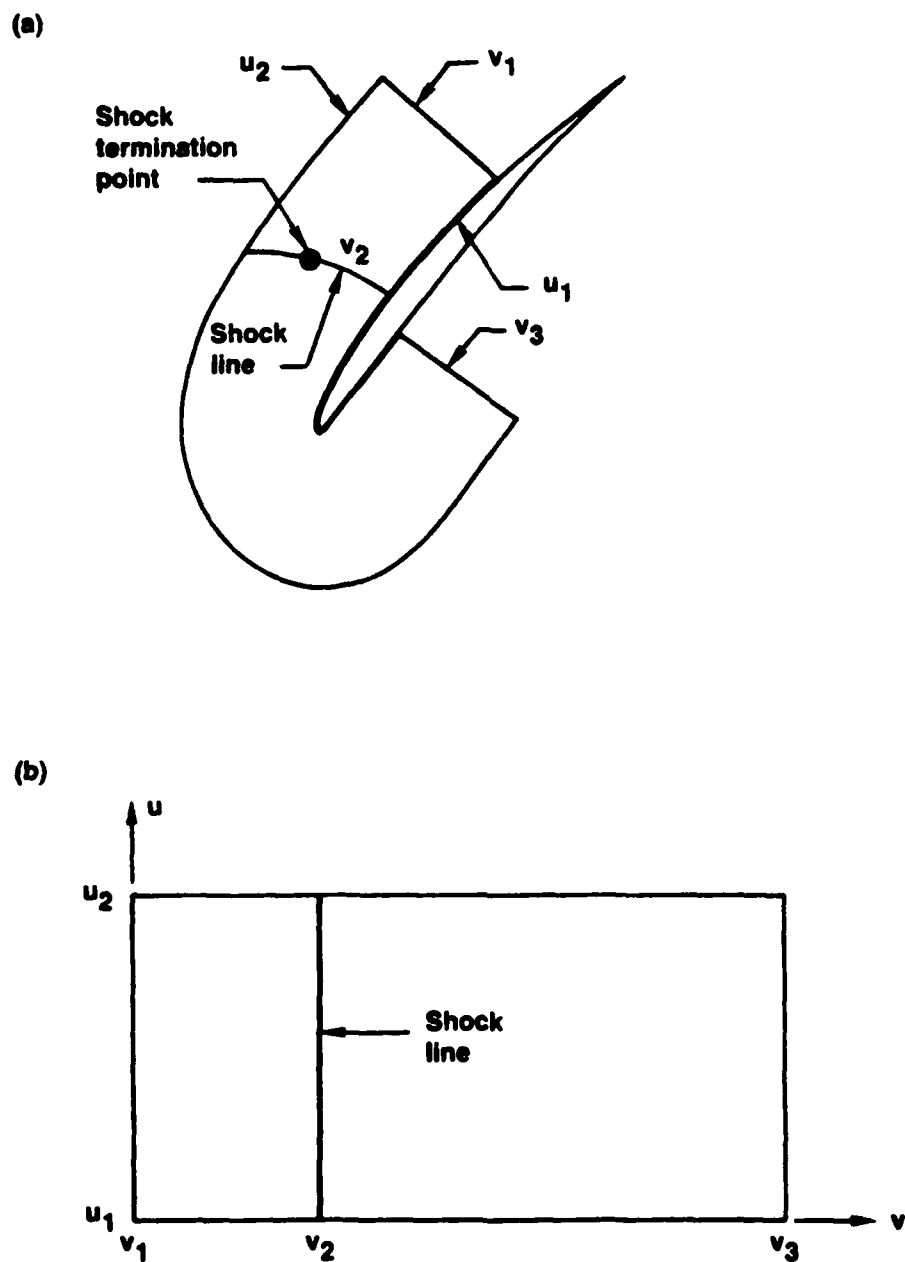


Figure 5. Typical local-mesh domain: (a) physical domain; (b) parametric domain.

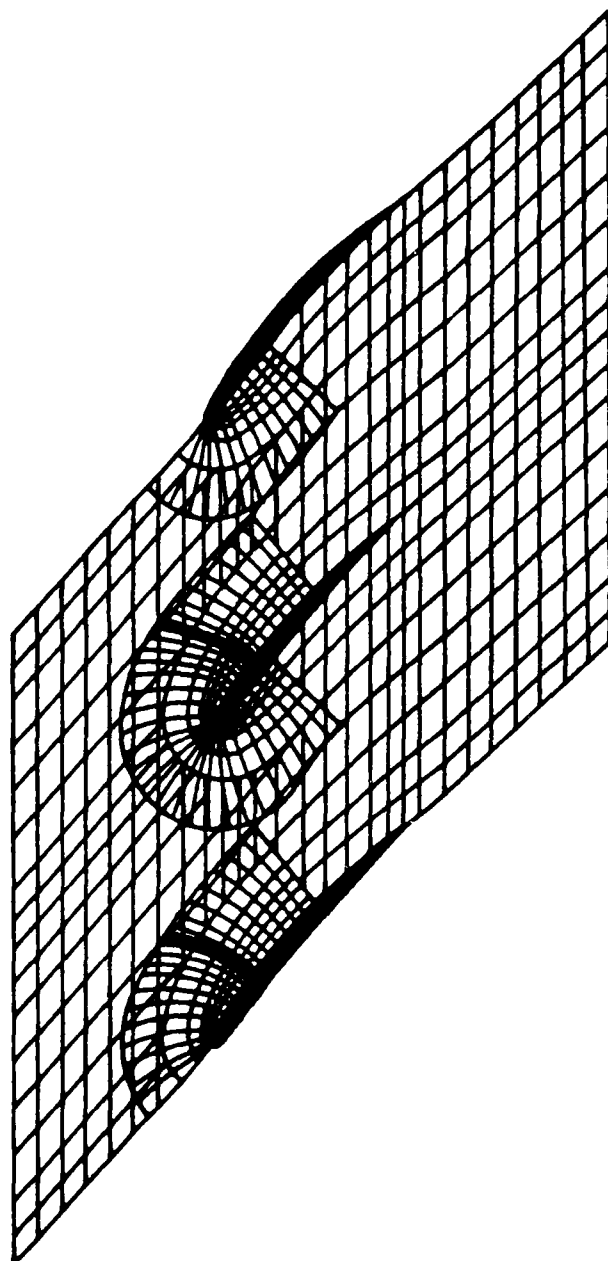


Figure 6. Schematic of composite mesh.

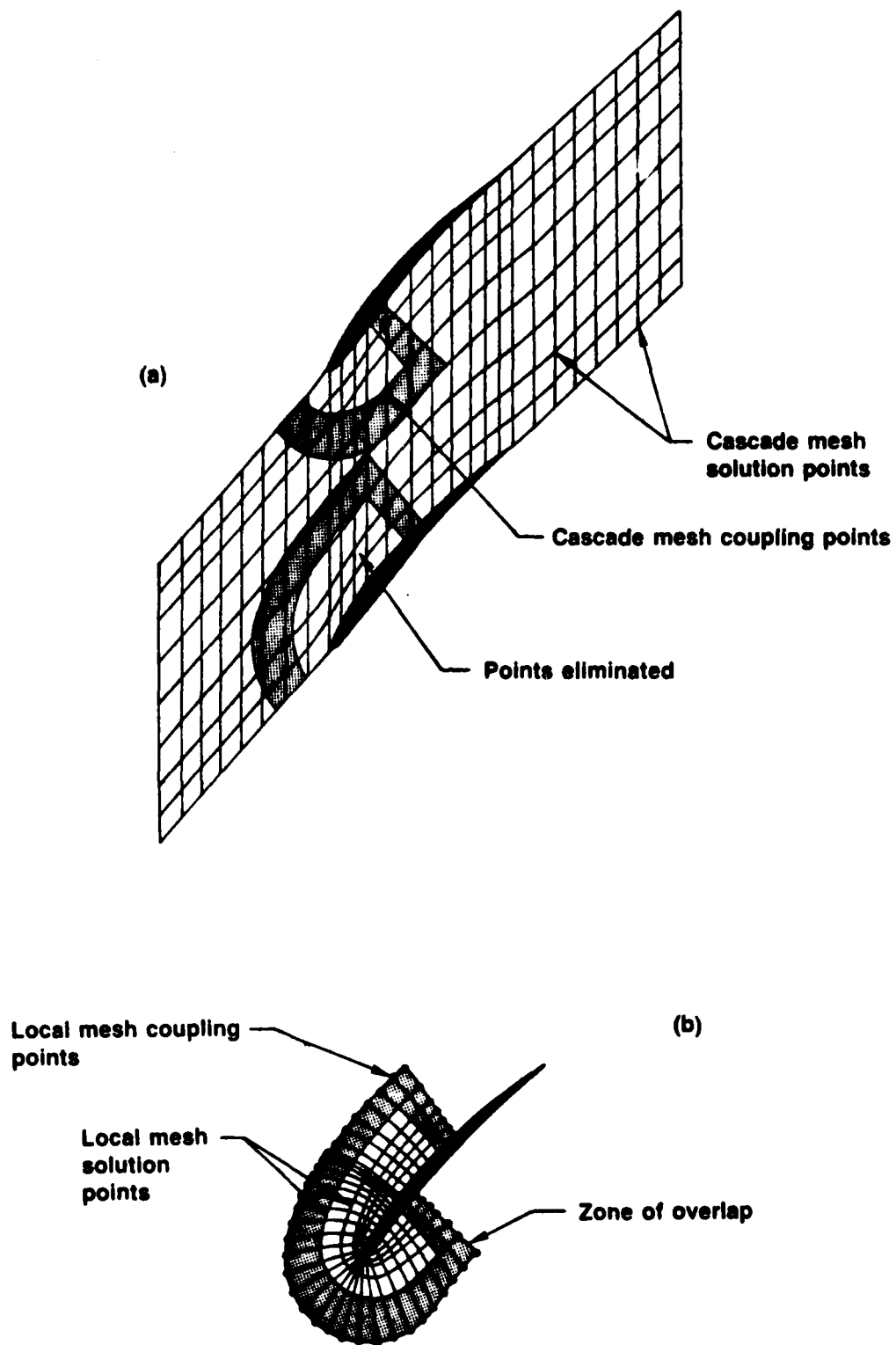


Figure 7. Mesh point classification: (a) local mesh; (b) cascade mesh.

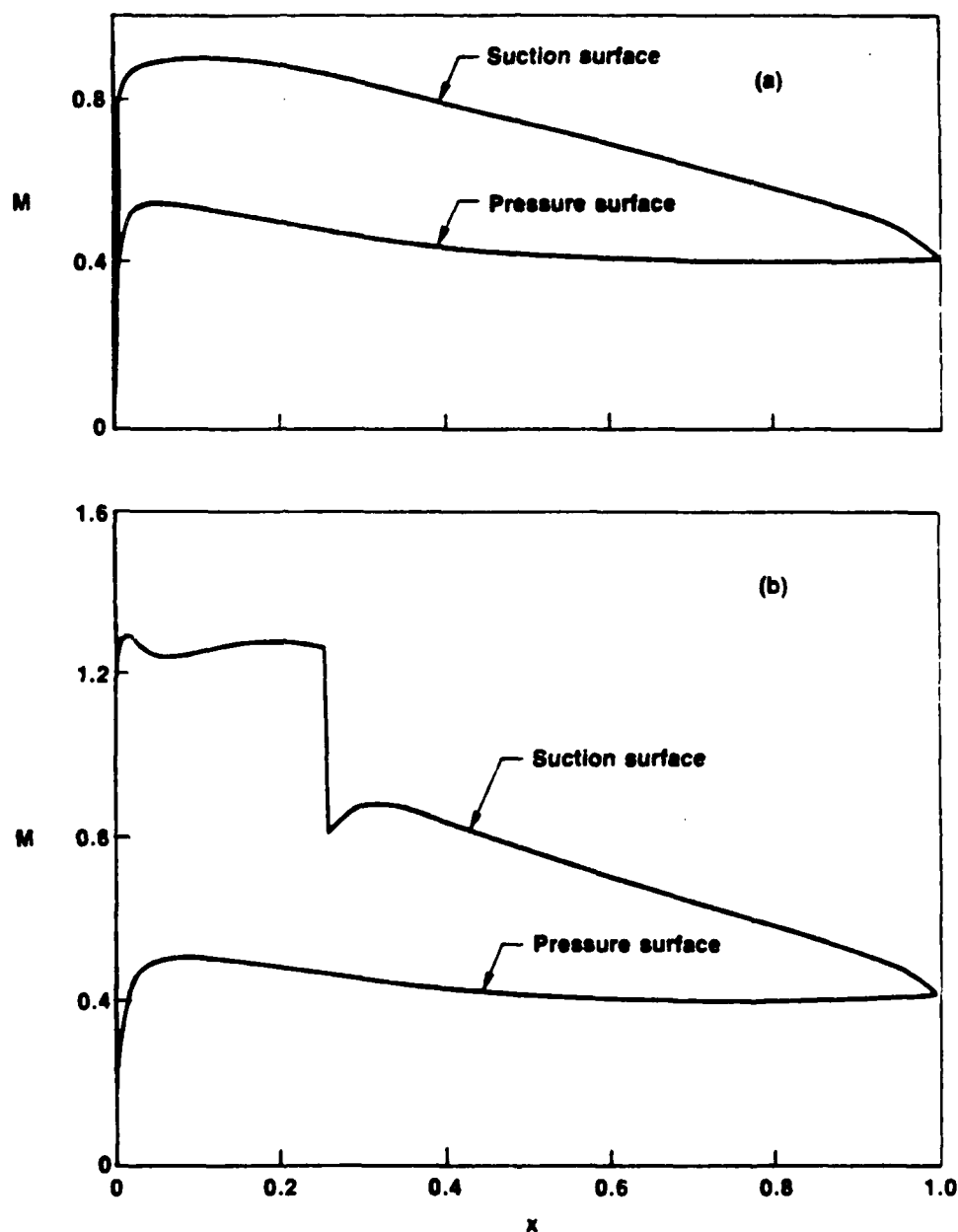


Figure 8. Surface Mach number distributions for the example NACA 0006 cascade: (a) subsonic flow; $M_{\infty} = 0.7$, $\Omega_{\infty} = 55^\circ$; (b) transonic flow; $M_{\infty} = 0.8$, $\Omega_{\infty} = 58^\circ$.

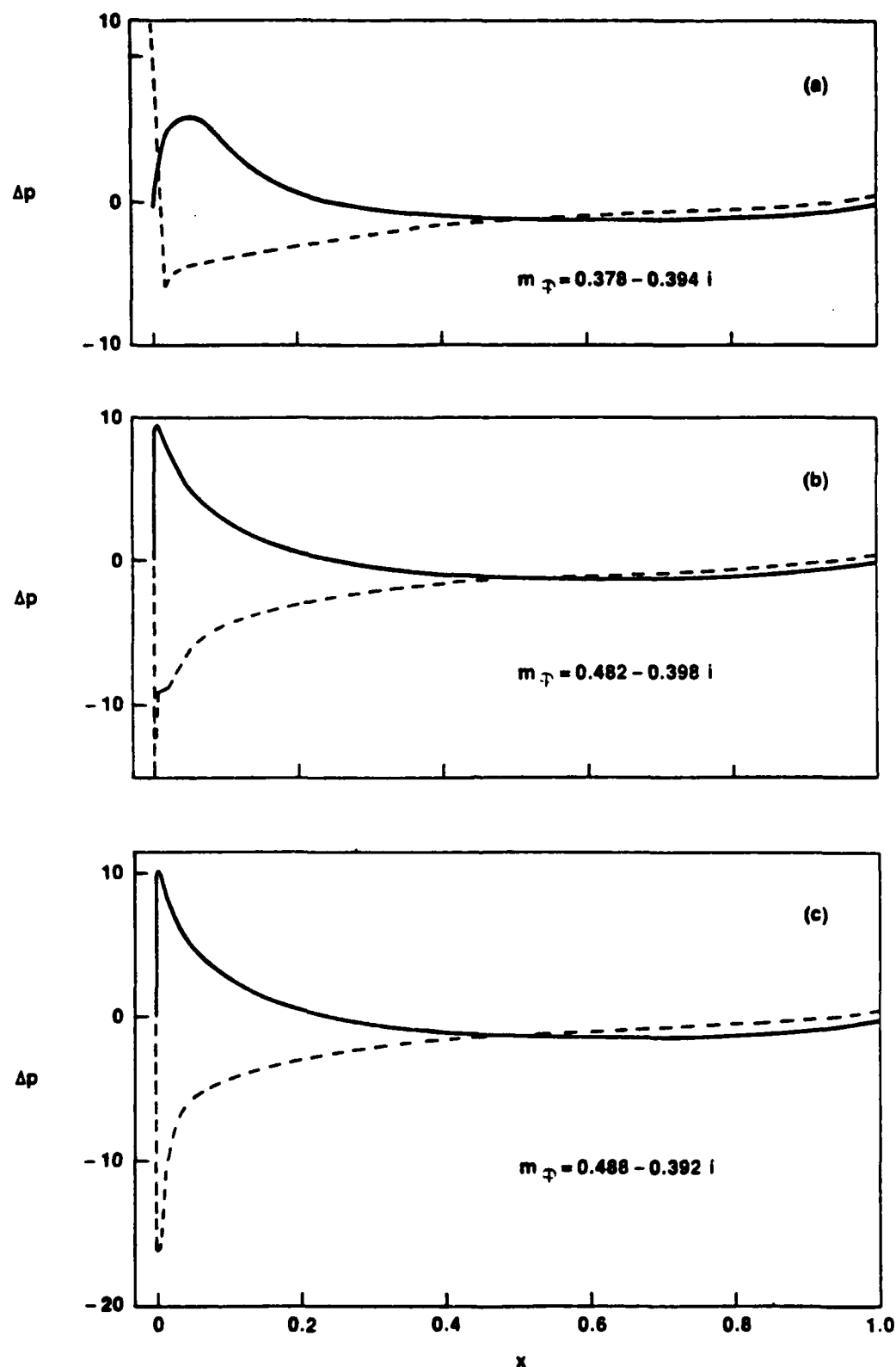


Figure 9. Unsteady pressure difference distributions due to torsional blade vibrations of the subsonic NACA 0006 cascade; $\alpha = (1, 0)$, $\omega = 1$, $\sigma = 180$ deg: (a) cascade-mesh solution; (b) single-pass solution using polar local mesh; (c) single-pass solution using transfinite local mesh: - - - in-phase component (real part); — out-of-phase component (imaginary part).

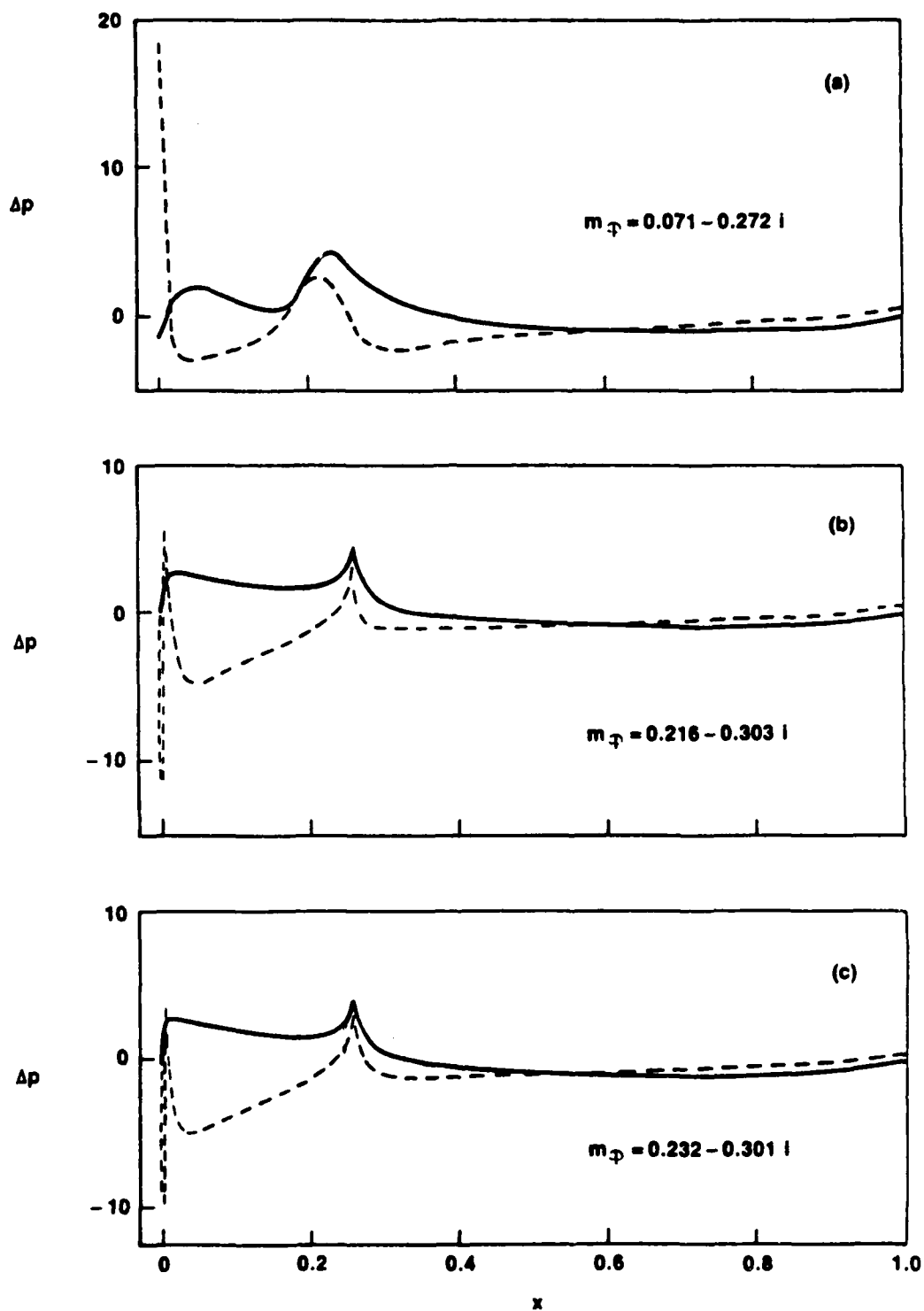


Figure 10. Unsteady pressure difference distributions due to torsional blade vibrations of the transonic NACA 0006 cascade; $\alpha = (1, 0)$, $\omega = 1$, $\sigma = 180$ deg: (a), (b), (c), --- and — as in Figure 9: shocks are captured in the local calculations.

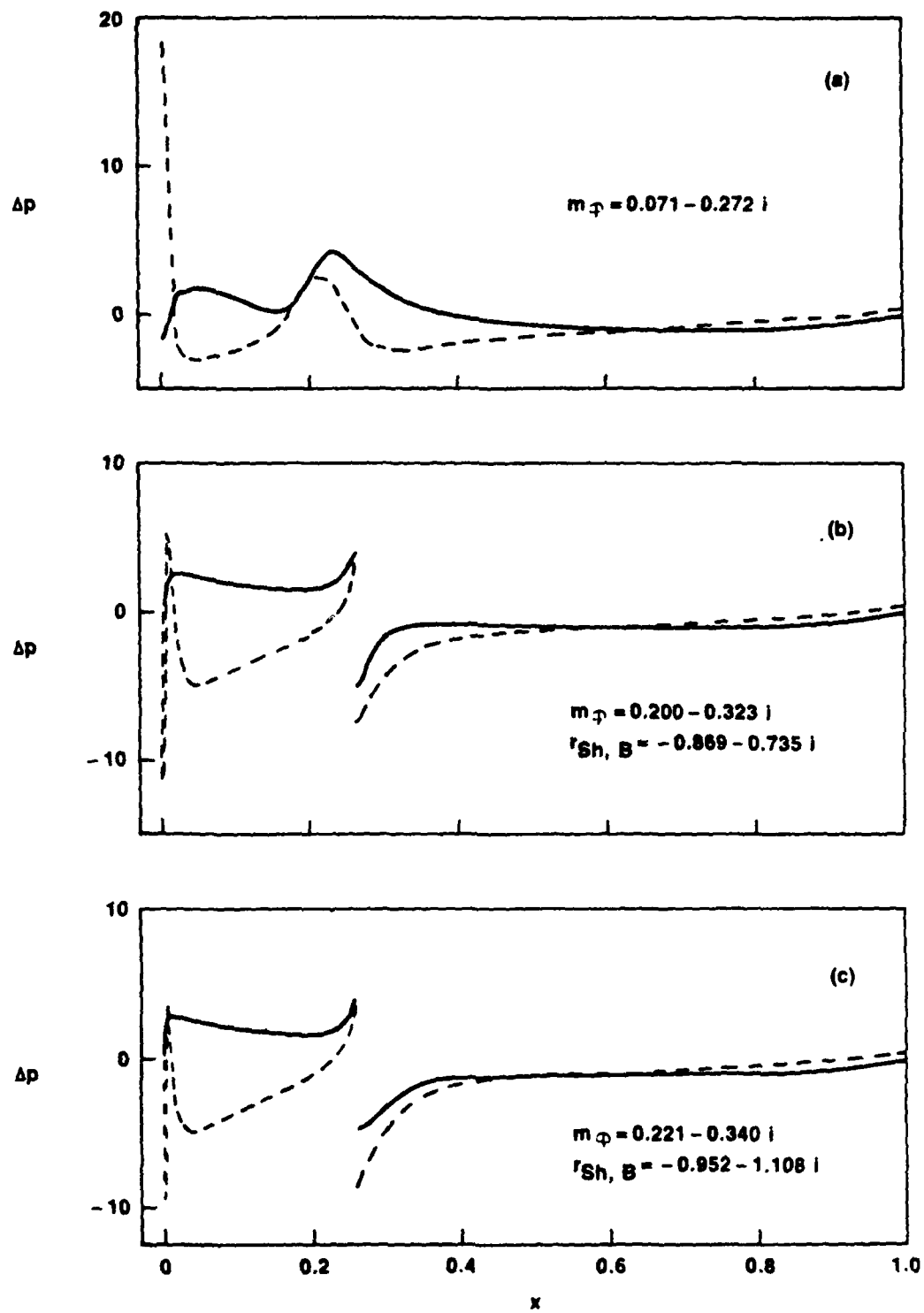


Figure 11. Unsteady pressure difference distributions due to torsional blade vibrations of the transonic NACA 0006 cascade; $\alpha = (1, 0)$, $\omega = 1$, $\sigma = 180$ deg: (a), (b), (c), — — — and — as in Figure 9; shocks are fitted in the local calculations.

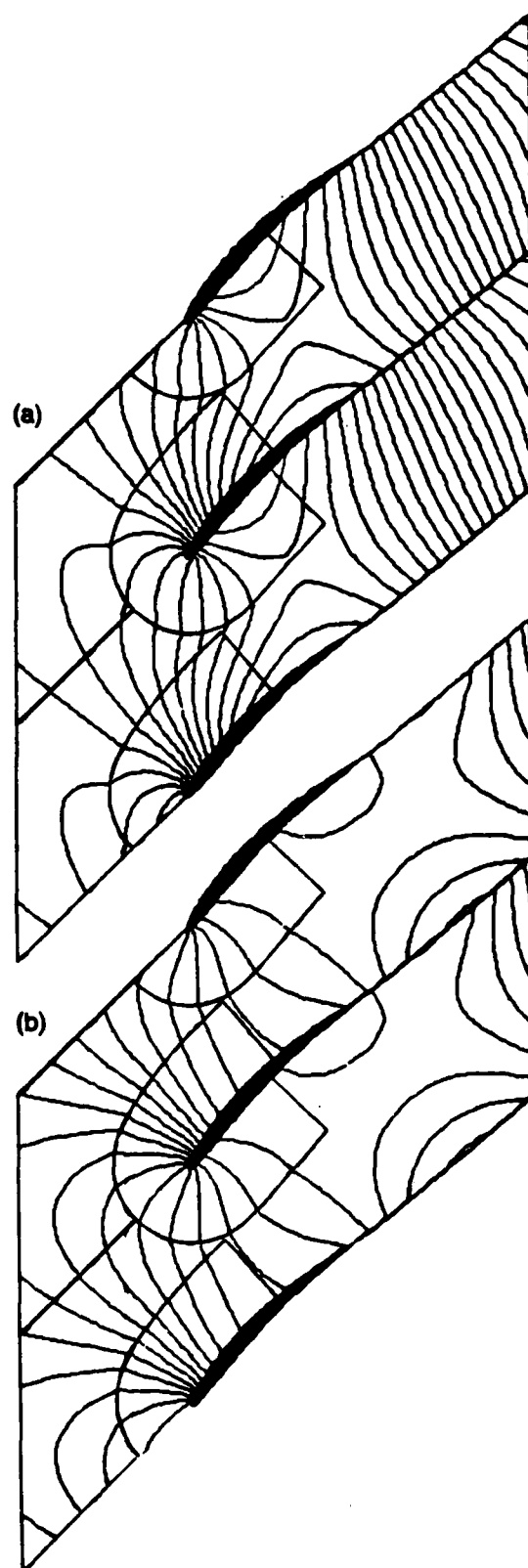


Figure 12. Single-pass solution for the unsteady potential contours due to torsional blade vibrations of the subsonic NACA 0006 cascade; $\alpha = (1, 0)$, $\omega = 1$, $\sigma = 180$ deg: (a) in-phase component (real part of ϕ); (b) out-of-phase component (imaginary part of ϕ).

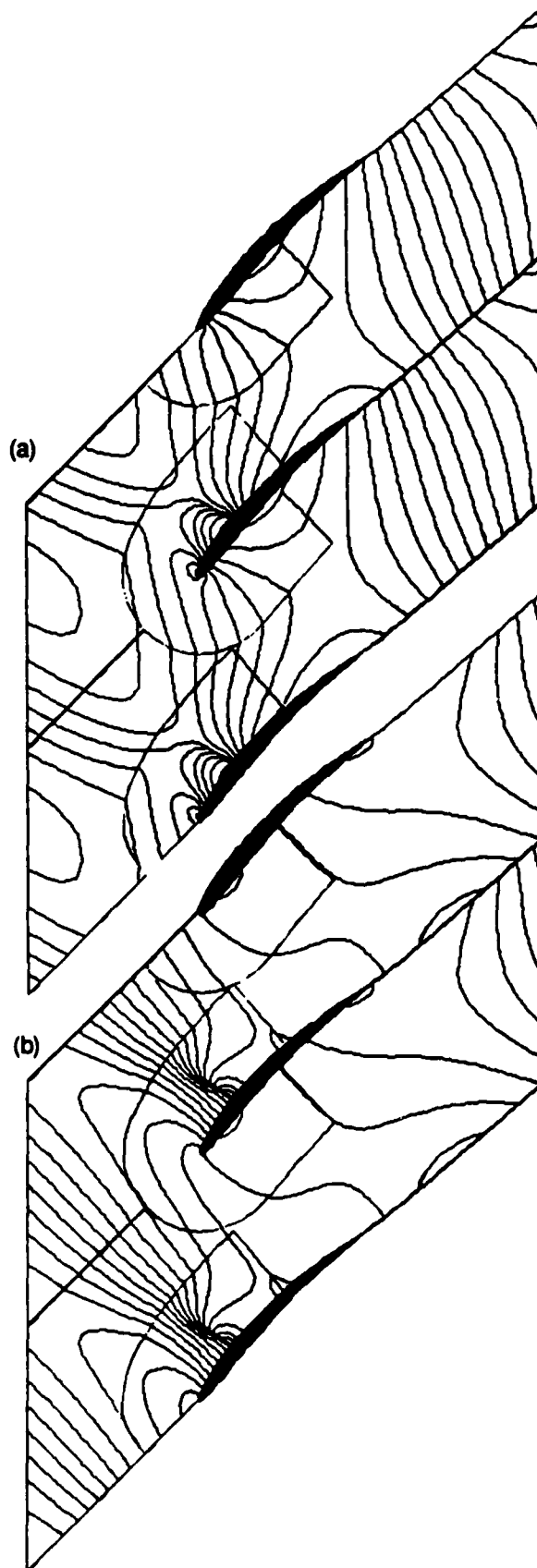


Figure 13. Single-pass solution for the unsteady potential contours due to torsional blade vibrations of the transonic NACA 0006 cascade; $\alpha = (1, 0)$, $\omega = 1$, $\sigma = 180$ deg: (a) and (b) as in Figure 12.

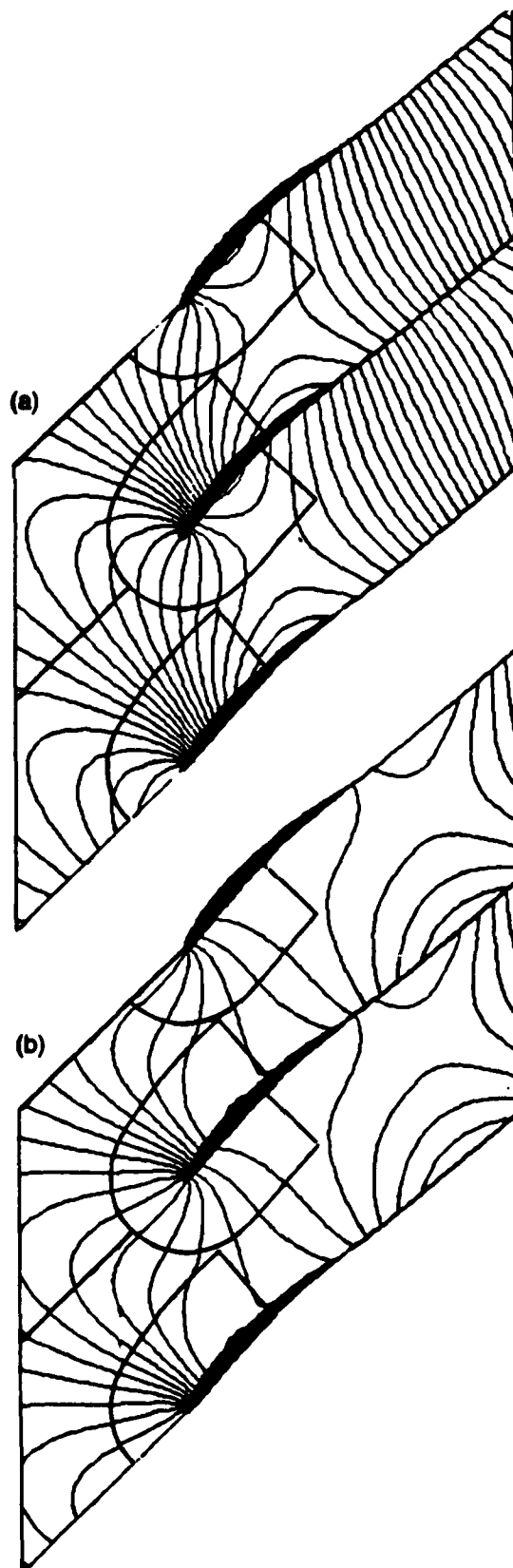


Figure 14. Composite solution for the unsteady potential contours due to torsional blade vibrations of the subsonic NACA 0006 cascade; $\alpha = (1, 0)$, $\omega = 1$, $\sigma = 180$ deg: (a) and (b) as in Figure 12.

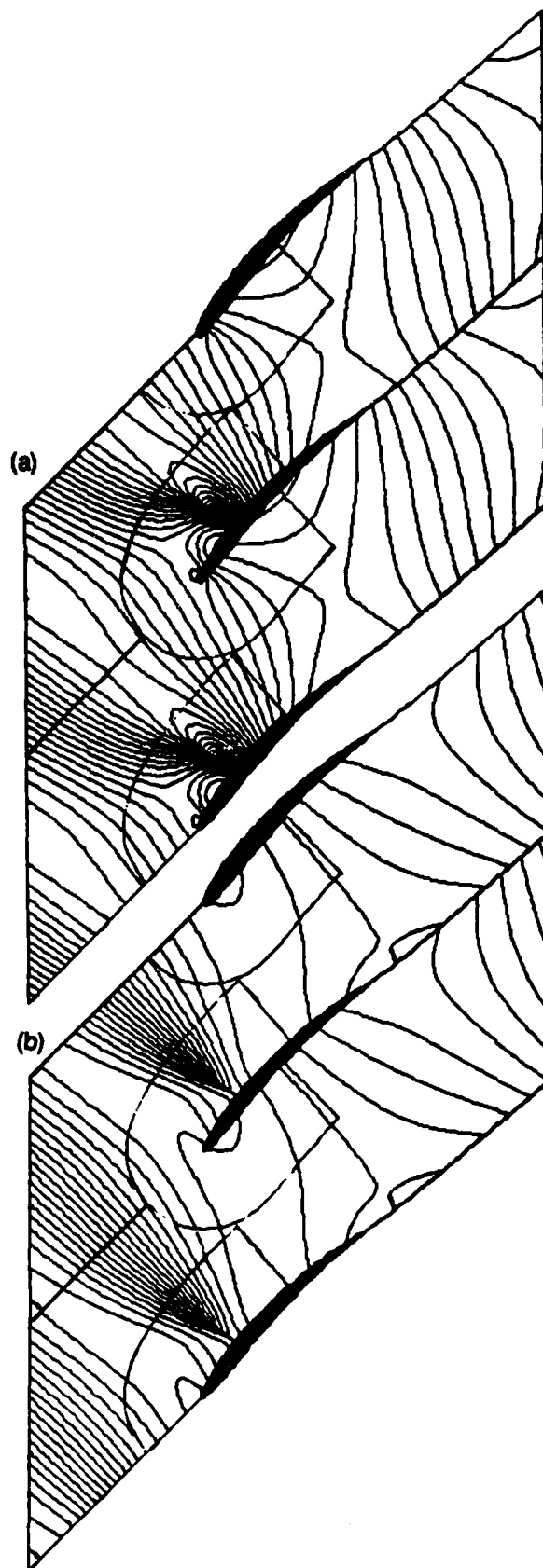


Figure 15. Composite solution for the unsteady potential contours due to torsional blade vibrations of the transonic NACA 0006 cascade; $\alpha = (1,0)$, $\omega = 1$, $\sigma = 180$ deg: (a) and (b) as in Figure 12.

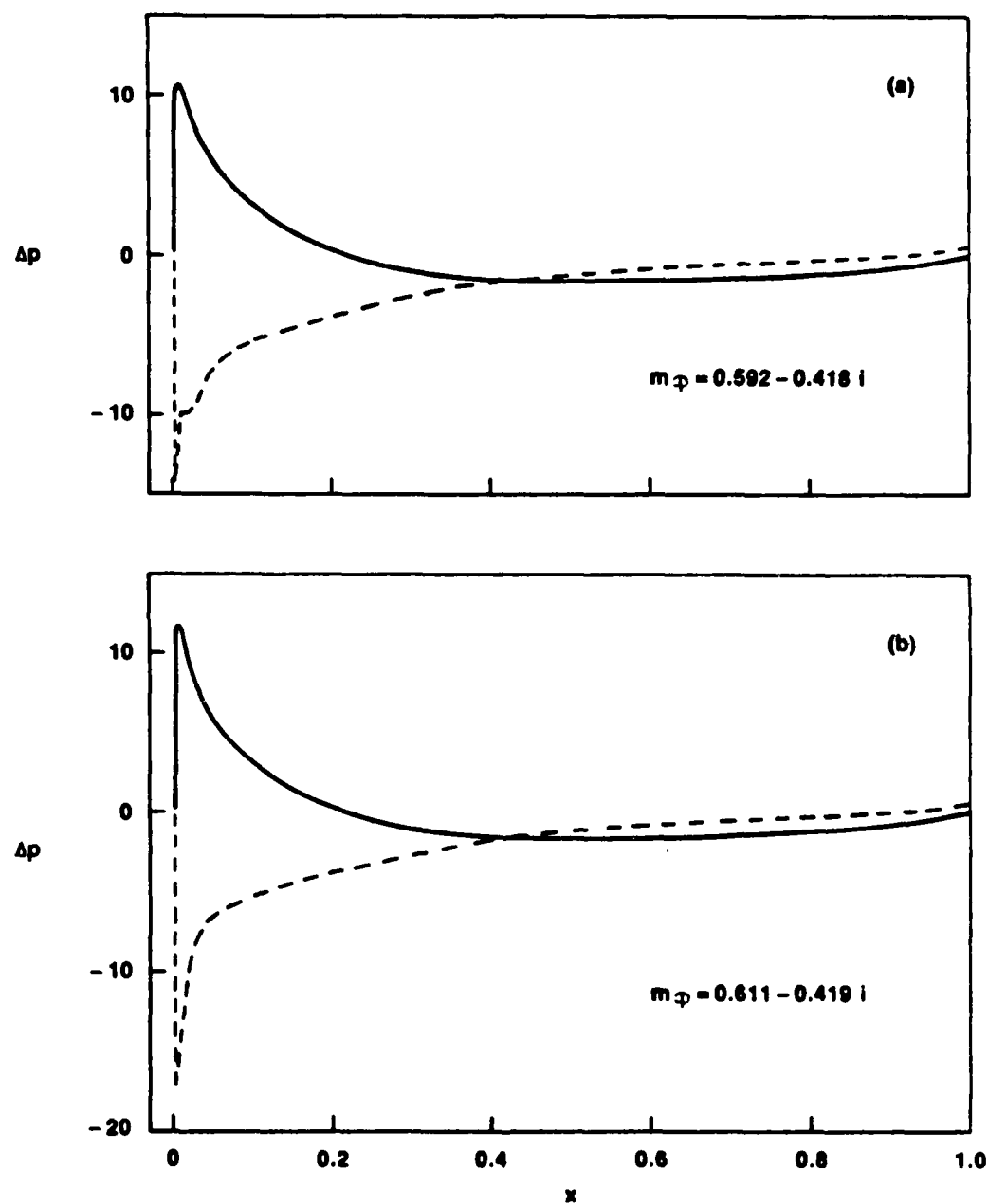


Figure 16. Unsteady pressure difference distributions due to torsional blade vibrations of the subsonic NACA 0006 cascade: $\alpha = (1, 0)$, $\omega = 1$, $\sigma = 180$ deg: (a) composite solution using polar local mesh; (b) composite solution using transfinite local mesh: - - - in-phase component; — out-of-phase component.

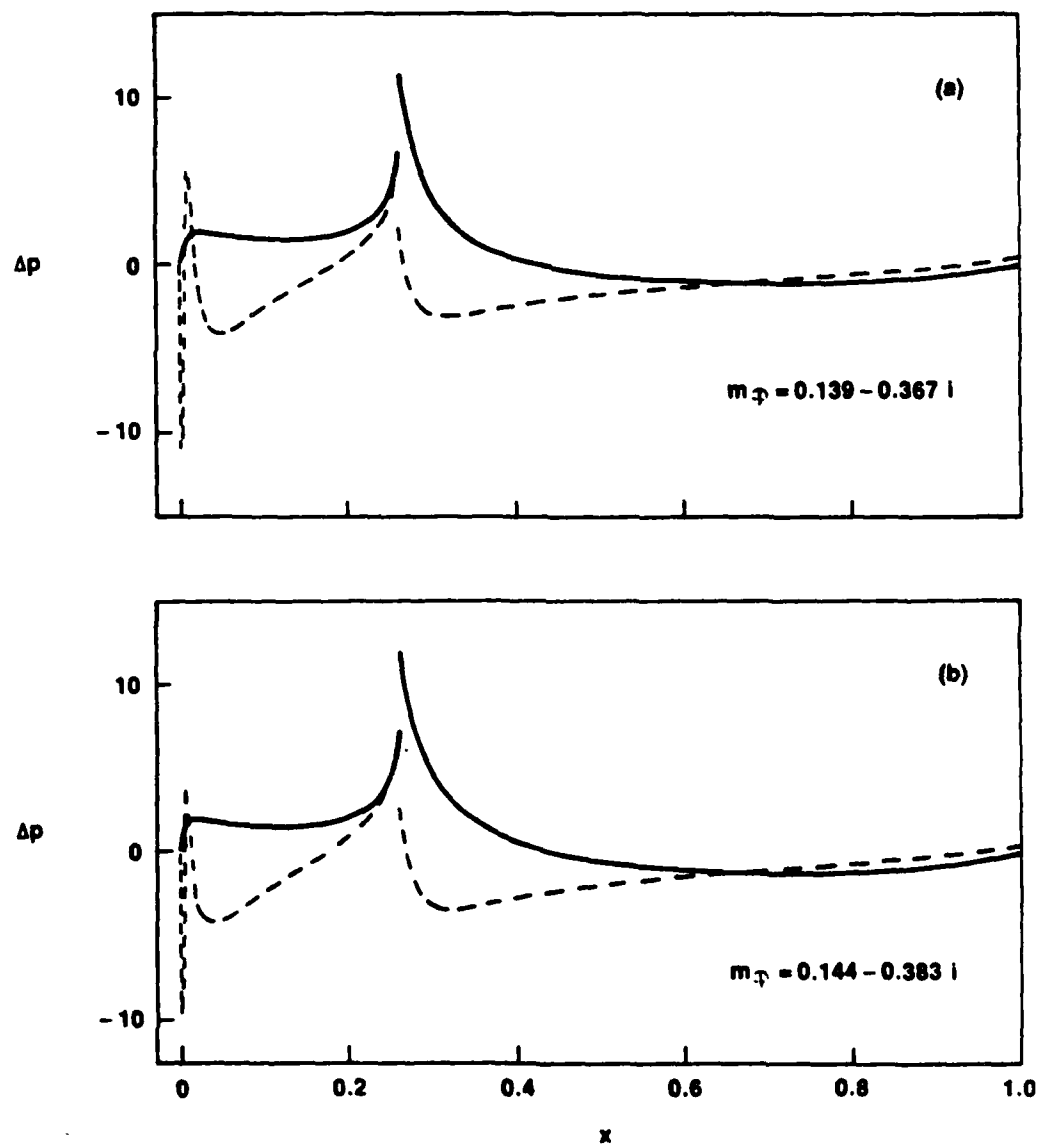


Figure 17. Composite solutions for the unsteady pressure difference distributions due to torsional blade vibrations of the transonic NACA 0006 cascade; $\alpha = (1, 0)$, $\omega = 1$, $\sigma = 180$ deg: (a), (b), — — — and — as in Figure 16: shocks are captured in the unsteady calculation.

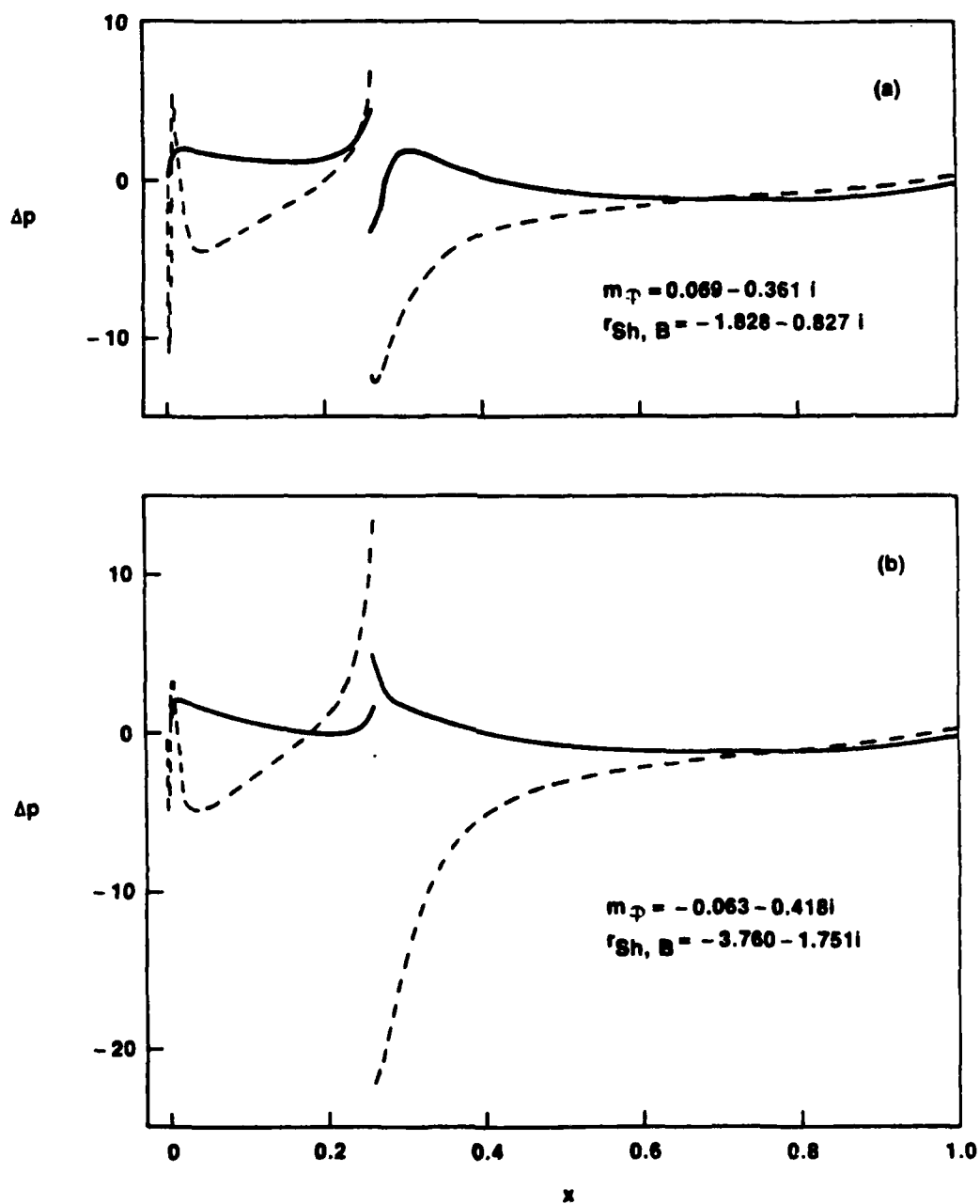


Figure 18. Composite solutions for the unsteady pressure difference distributions due to torsional blade vibrations of the transonic NACA 0006 cascade; $\alpha = (1, 0)$, $\omega = 1$, $\sigma = 180$ deg: (a), (b), --- and — as in Figure 16: shocks are fitted in unsteady calculation.

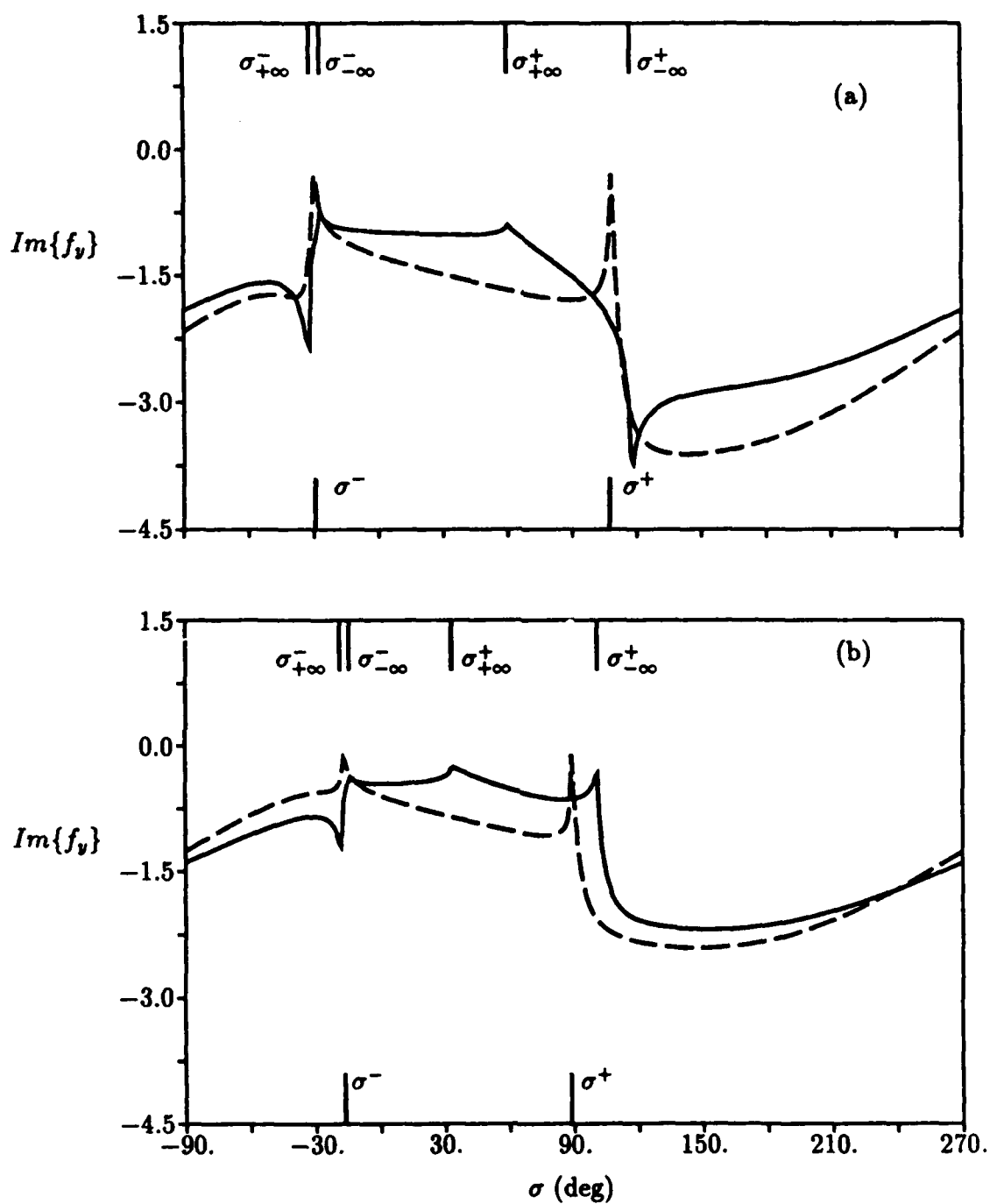


Figure 19. Out-of-phase component of unsteady lift vs interblade phase angle for pure bending vibrations of the NACA 0006, —, and flat-plate, ---, cascades:
 (a) $M_{\infty} = 0.7$, $\omega = 1$; (b) $M_{\infty} = 0.8$, $\omega = 0.5$.

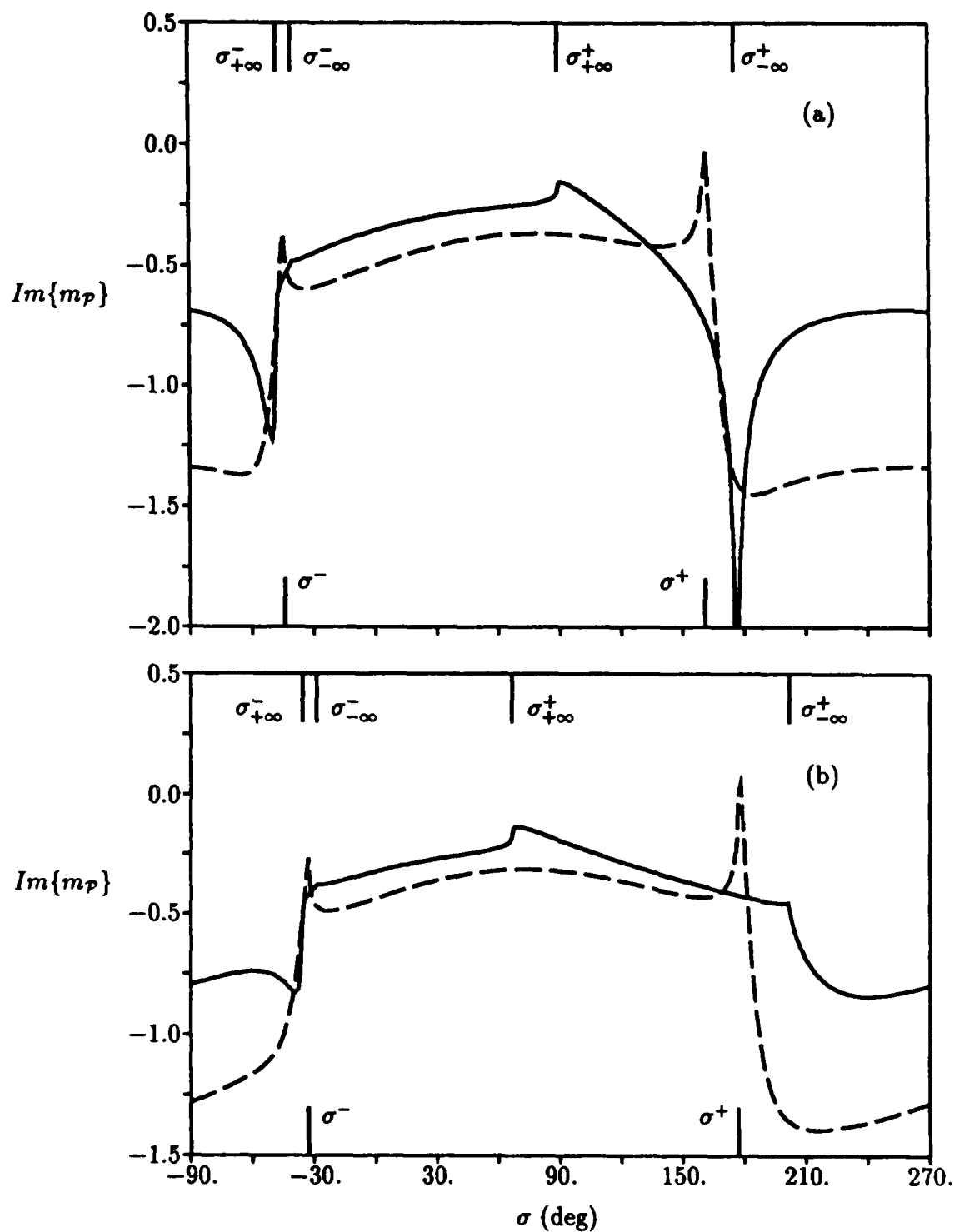


Figure 20. Out-of-phase component of unsteady moment vs interblade phase angle for pure torsional blade vibrations of the NACA 0006, —, and flat-plate, ---, cascades:
 (a) $M_{\infty} = 0.7$, $\omega = 1.5$; (b) $M_{\infty} = 0.8$, $\omega = 1.0$.

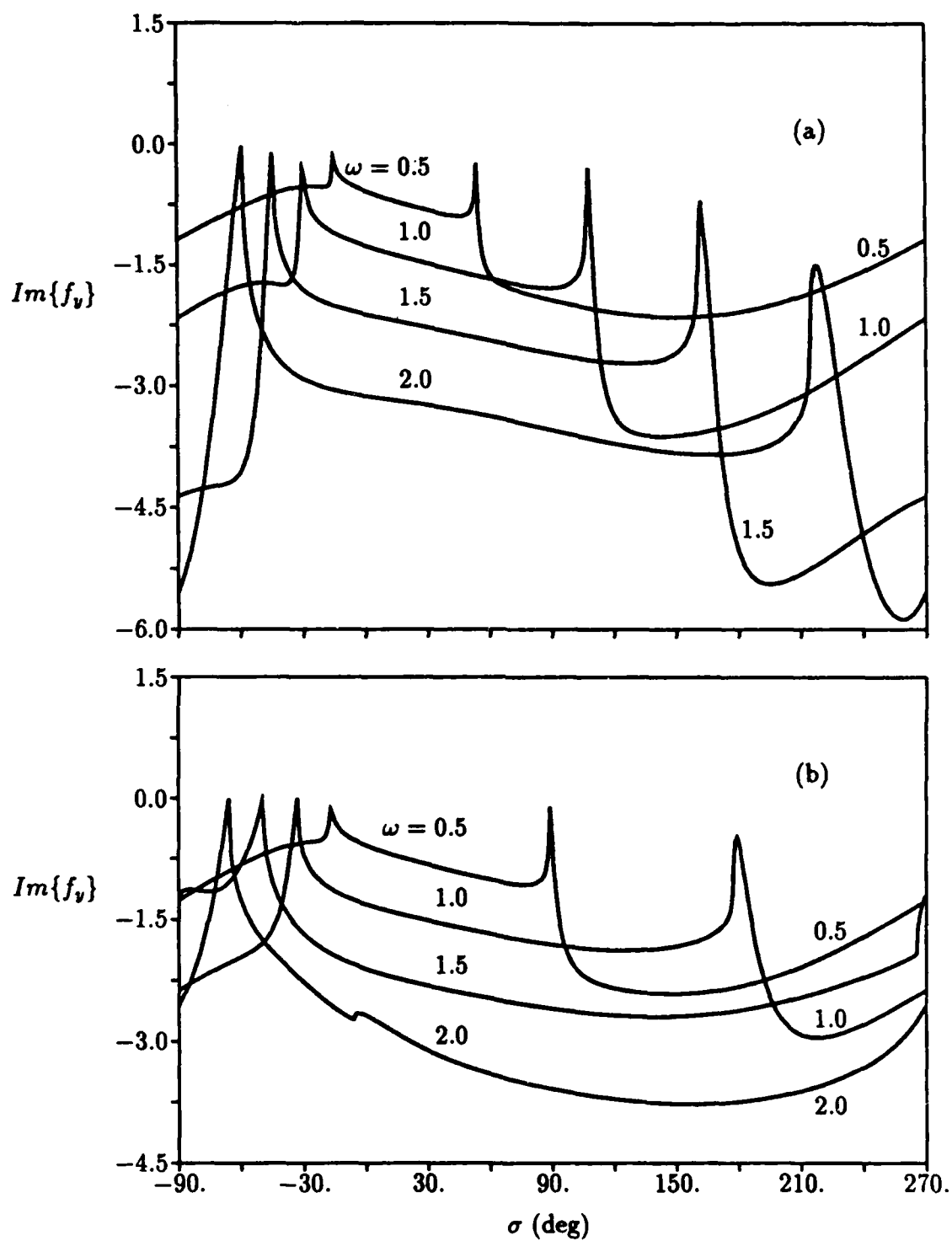


Figure 21. Out-of-phase component of unsteady lift vs interblade phase angle for pure bending vibrations of the flat-plate cascade at $\omega = 0.5, 1.0, 1.5$ and 2.0 : (a) $M_\infty = 0.7$; (b) $M_\infty = 0.8$.

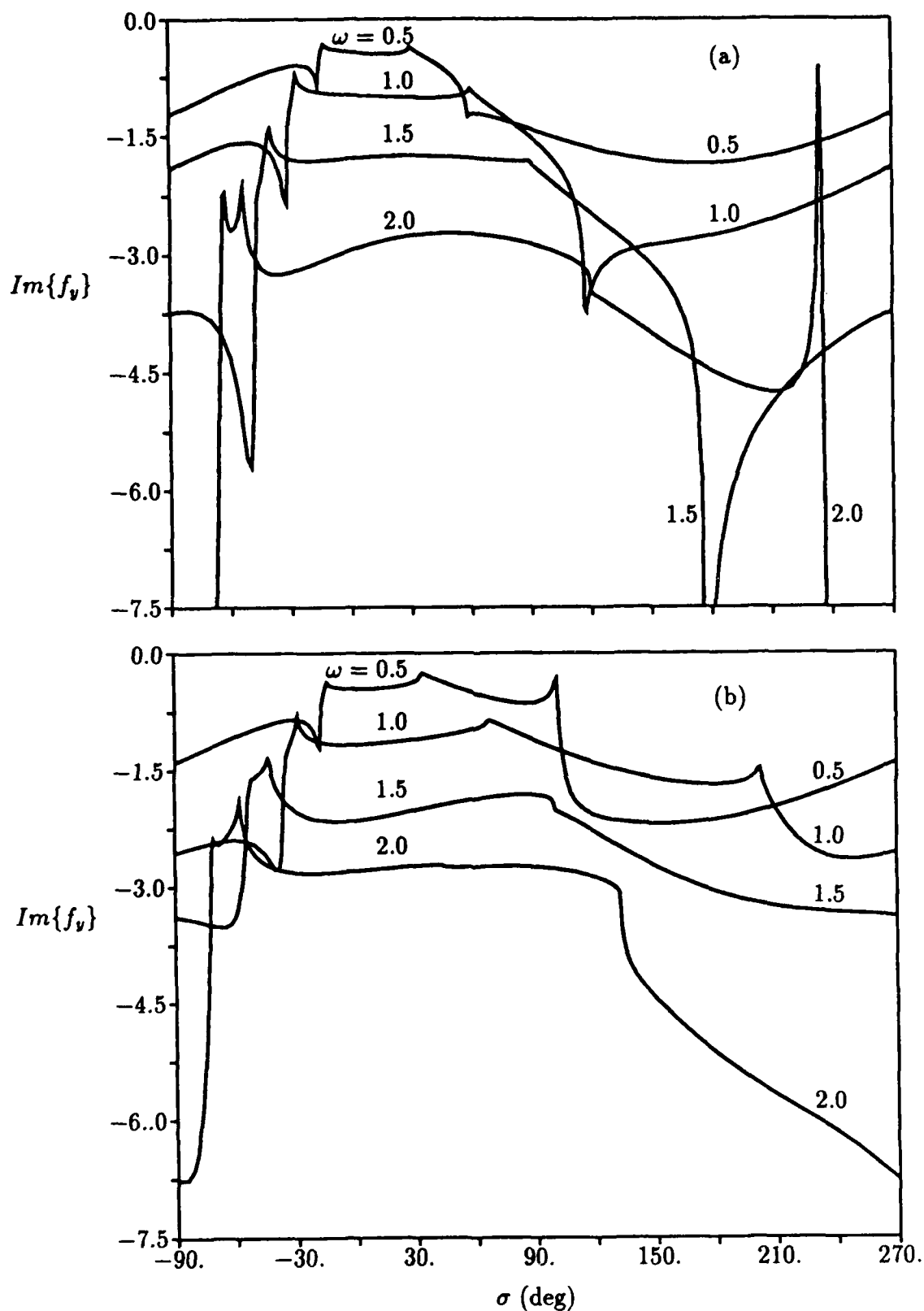


Figure 22. Out-of-phase component of unsteady lift vs interblade phase angle for pure bending vibrations of the NACA 0006 cascade at $\omega = 0.5, 1.0, 1.5$ and 2.0 :
 (a) $M_\infty = 0.7$; (b) $M_\infty = 0.8$.

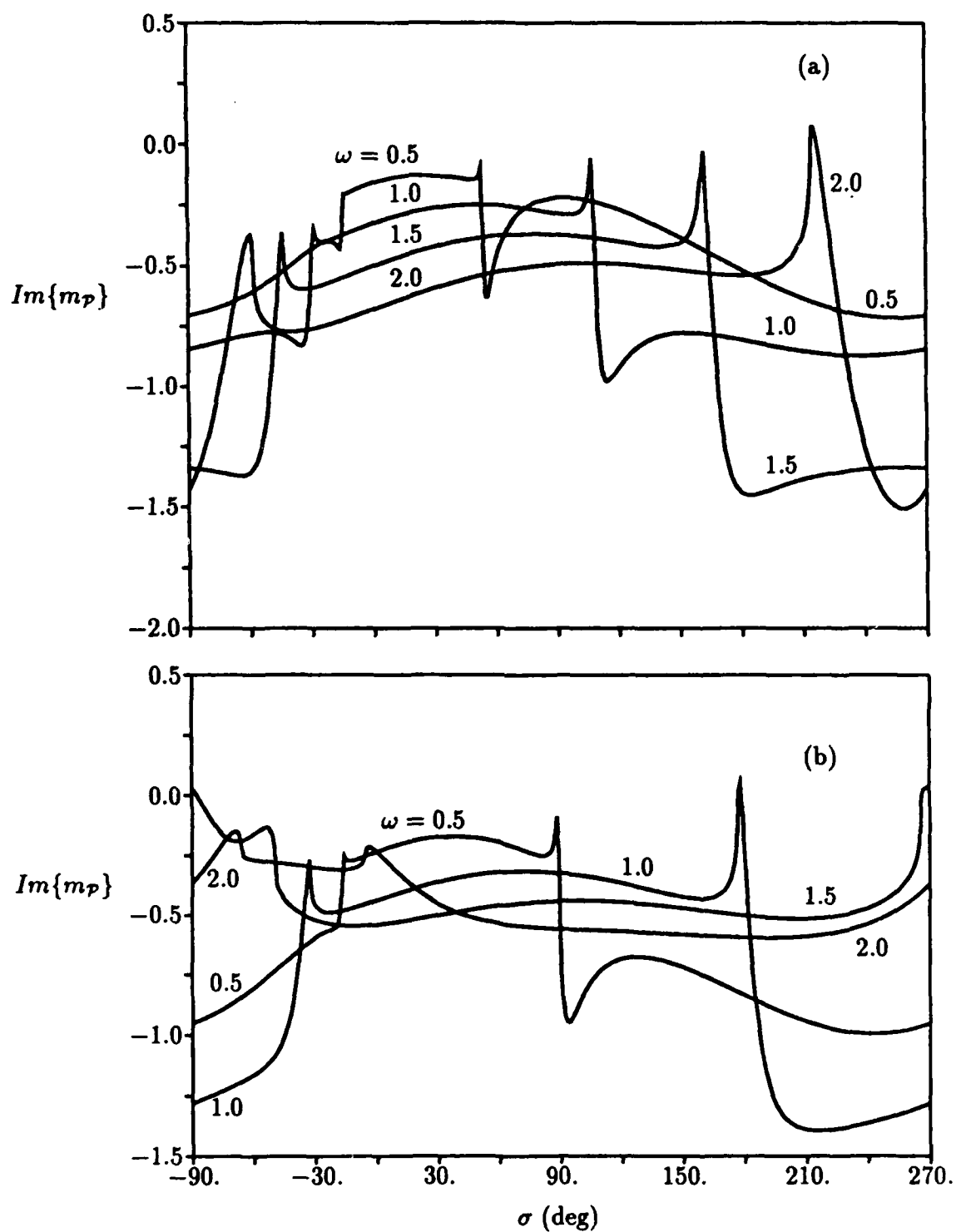


Figure 23. Out-of-phase component of unsteady moment vs interblade phase angle for pure torsional vibrations of the flat-plate cascade at $\omega = 0.5, 1.0, 1.5$ and 2.0 : (a) $M_\infty = 0.7$; (b) $M_\infty = 0.8$.

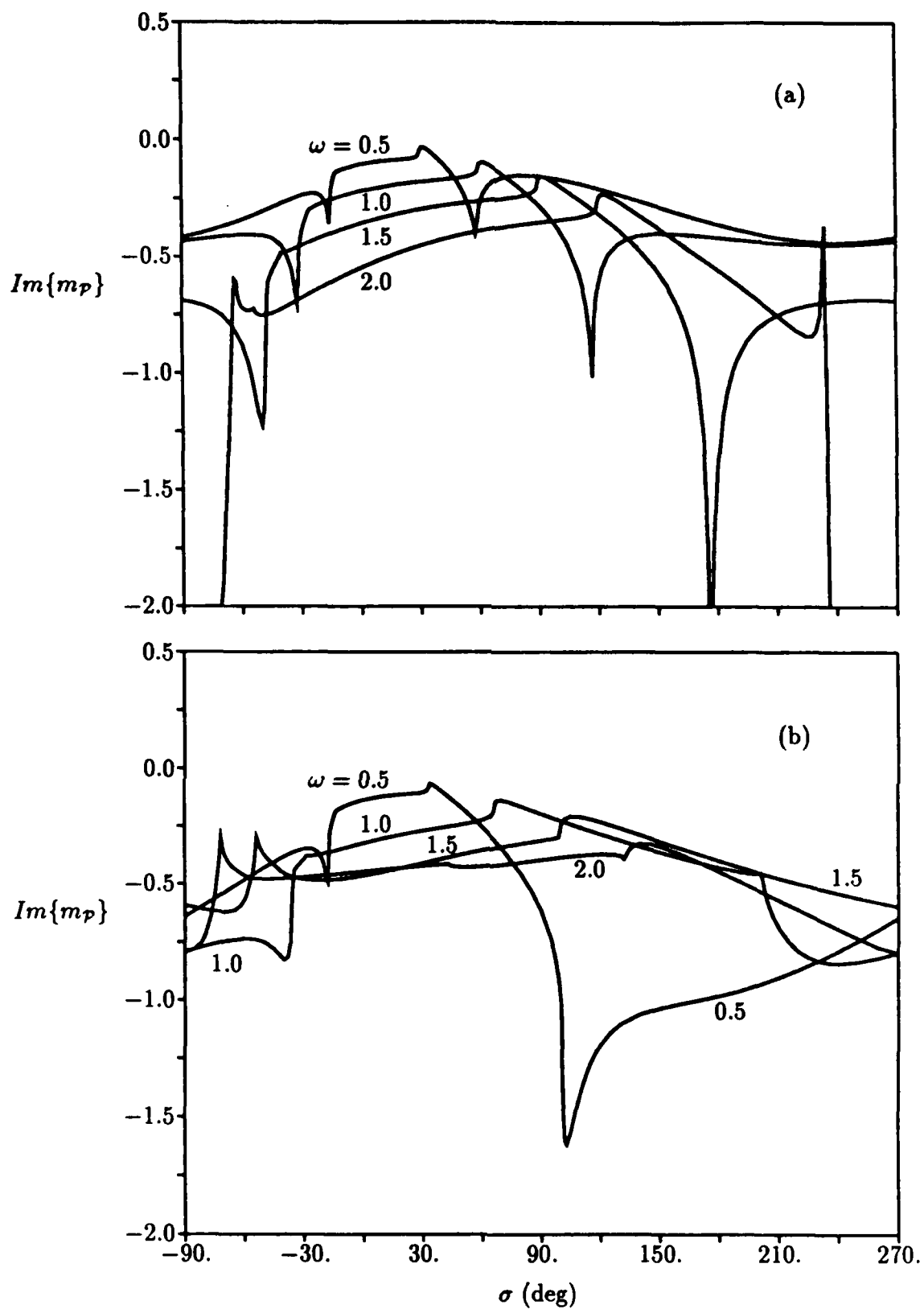


Figure 24. Out-of-phase component of unsteady moment vs interblade phase angle for pure torsional vibrations of the NACA 0006 cascade at $\omega = 0.5, 1.0, 1.5$ and 2.0 :
(a) $M_\infty = 0.7$; (b) $M_\infty = 0.8$.

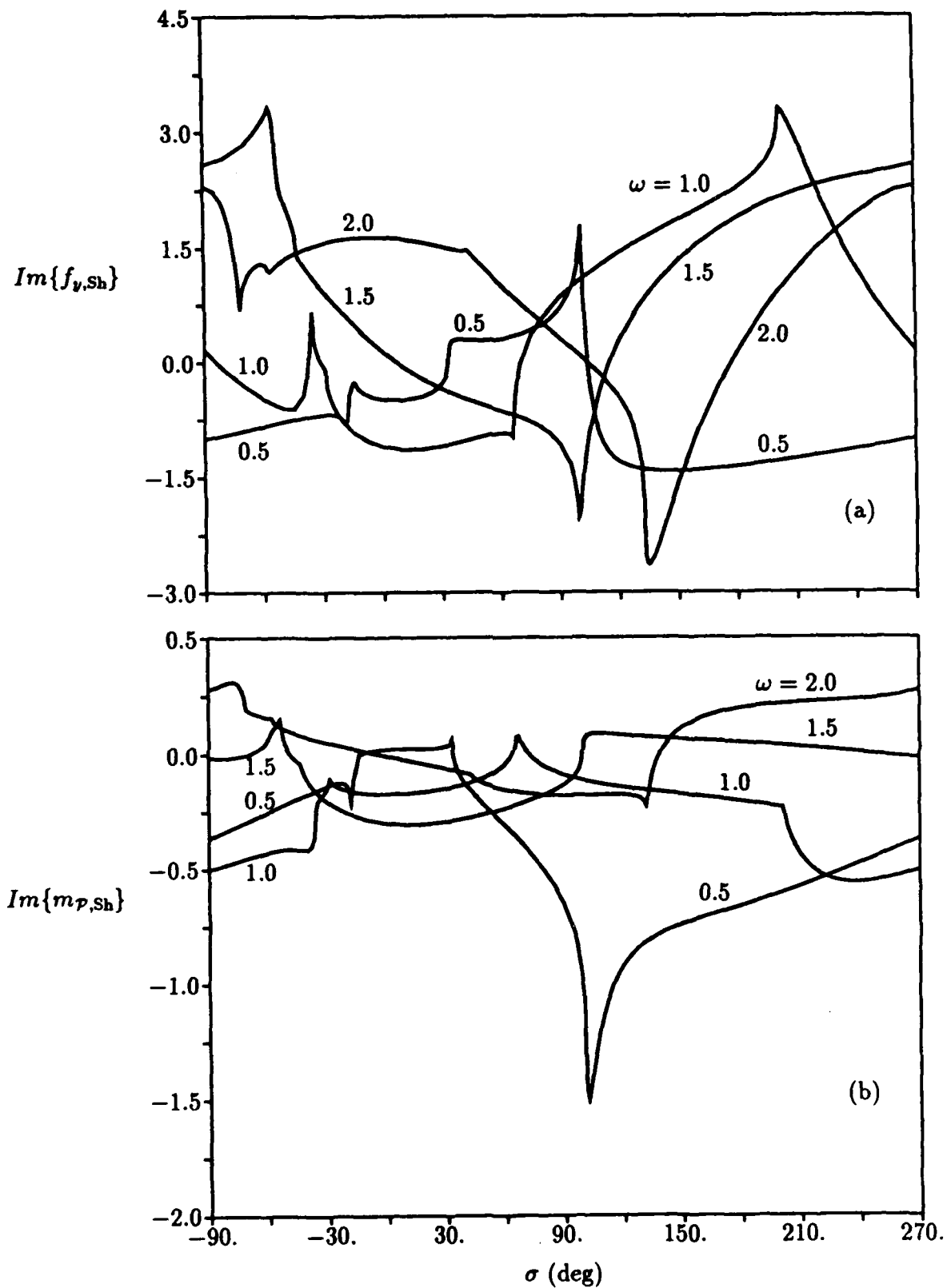


Figure 25. Out-of-phase components of the shock loads due to single-degree-of-freedom blade motions of the transonic NACA 0006 cascade: (a) lift force due to bending; (b) moment due to torsion.

REFERENCES

1. Verdon, J. M., "Linearized Unsteady Aerodynamic Theory," chapter II in *AGARD Manual on Aeroelasticity in Axial-Flow Turbomachines*, Vol. 1, *Unsteady Turbomachinery Aerodynamics*, M. F. Platzer and F. O. Carta (eds.), AGARD-AG-298, March 1987.
2. Verdon, J. M., "Unsteady Aerodynamics for Turbomachinery Aeroelastic Applications," UTRC Report R86-151774-1, June 1986, also to appear in *Unsteady Transonic Aerodynamics*, D. Nixon (ed.), *Progress in Astronautics and Aeronautics*, AIAA, New York, 1988.
3. Atassi, H. and Akai, T. J., "Aerodynamic and Aeroelastic Characteristics of Oscillating Loaded Cascades at Low Mach Number, I. Pressure Distribution, Forces and Moments," *Trans. ASME A: Journal of Engineering for Power*, Vol. 102, No. 2, April 1980, pp. 344-351.
4. Caruthers, J. E., "Aerodynamic Analysis of Cascaded Airfoils in Unsteady Rotational Flow," *Proc. 2nd Intl. Symp. on Aeroelasticity in Turbomachines*, P. Suter (ed.), Juris-Verlag, Zurich., 1981, pp. 31-64.
5. Whitehead, D. S. and Grant, R. J., "Force and Moment Coefficients for High Deflection Cascades," *Proc. 2nd Intl. Symp. on Aeroelasticity in Turbomachines*, P. Suter (ed.), Juris-Verlag Zurich, 1981, pp. 85-127.
6. Verdon, J. M. and Caspar, J. R., "Development of a Linear Unsteady Aerodynamic Analysis for Finite-deflection Subsonic Cascades," *AIAA Journal*, Vol. 20, No. 9, September 1982, pp. 1259-1267.
7. Whitehead, D. S., "The Calculation of Steady and Unsteady Transonic Flow in Cascades," Cambridge Univ. Engineering Dept. Report CUED/A-Turbo/TR 118, 1982.
8. Verdon, J. M. and Caspar, J. R., "A Linearized Unsteady Aerodynamic Analysis for Transonic Cascades," *Journal of Fluid Mechanics*, Vol. 149, December 1984, pp. 403-429.
9. Fleeter, S., "Aeroelasticity Research for Turbomachine Applications," *Journal of Aircraft*, Vol. 16, No. 5, May 1979, pp. 320-326.
10. Fleeter, S. and Jay, R. L., "Unsteady Aerodynamic Measurements in Flutter Research," chapter VIII in *AGARD Manual on Aeroelasticity in Axial-Flow Turbomachines*, Vol. 1, *Unsteady Turbomachinery Aerodynamics*, M. F. Platzer and F. O. Carta (eds.), AGARD-AG-298, March 1987.
11. Usab, W. J., Jr., and Verdon, J. M., "On the Application of a Linearized Unsteady Potential Flow Analysis to Two-Dimensional Fan-Tip Cascades," *Transactions of the ASME, Journal of Turbomachinery*, Vol. 108, NO. 1, July 1986, pp. 59-67.
12. Shaw, L. M., Boldman, D. R., Buggele, A. E. and Buffam, D. J., "Unsteady Pressure Measurements on a Biconvex Airfoil in a Transonic Oscillating Cascade," ASME

30th International Gas Turbine Conference and Exhibit, Houston, Texas, Paper 85-GT-212, March 18-21, 1985.

13. Verdon, J. M. and Usab, W. J., Jr., "Application of a Linearized Unsteady Aerodynamic Analysis to Standard Cascade Configurations," NASA CR 3940, prepared under Contract NAS3-22257 for Lewis Research Center, November 1985.

14. Fransson, T. H. and Suter, P., "Two-Dimensional and Quasi Three-Dimensional Experimental Standard Configurations for Aeroelastic Investigations in Turbomachine-Cascades," Report LTA-TM-83-2, Ecole Polytechnique Federale de Lausanne, 1983.

15. Fransson, T. H., "Workshop on Aeroelasticity in Turbomachine-Cascades," *Cambridge Symposium Proceedings: Unsteady Aerodynamics of Turbomachines and Propellers*, September 1984, pp. 361-395.

16. Miles, J. W., *The Potential Theory of Unsteady Supersonic Flow*, Cambridge University Press, 1959.

17. Landahl, M., *Unsteady Transonic Flow*, Pergamon Press, 1961.

18. McNally, W. D. and Sockol, P. M., "Computational Methods for Internal Flows with Emphasis on Turbomachinery," NASA Tech. Memo. 82764, November 1981.

19. Caspar, J. R., "Unconditionally Stable Calculation of Transonic Potential Flow Through Cascades Using an Adaptive Mesh for Shock Capture," *Trans. ASME A: Journal of Engineering for Power*, Vol. 105, No. 3, July 1983, pp. 504-513.

20. Verdon, J. M., "The Unsteady Flow in the Far Field of an Isolated Blade Row," UTRC Report R87-957333-1 prepared under Contract N00014-85-C-0702 for the Naval Air Systems Command, April, 1987, also submitted for publication to the *Journal of Fluids and Structures*.

21. Williams, M. H., "Linearization of Unsteady Transonic Flows Containing Shocks," *AIAA Journal*, Vol. 17, No. 4, April 1979, pp. 394-397.

22. Hounjet, M. H. L., "Transonic Panel Method to Determine Loads on Oscillating Airfoils with Shocks," *AIAA Journal*, Vol. 19, No. 5, May 1981, pp. 559-566.

23. Tijdeman, H., "Investigations of the Transonic Flow Around Oscillating Airfoils," National Aerospace Laboratory (Amsterdam) Rep. NLR TR 77090-U, December 1977.

24. Ehlers F. E. and Weatherill, W. H., "A Harmonic Analysis Method for Unsteady Transonic Flow and Its Application to the Flutter of Airfoils," NASA CR 3537, May 1982.

25. Caspar, J. R. and Verdon, J. M., "Numerical Treatment of Unsteady Subsonic Flow Past an Oscillating Cascade," *AIAA Journal*, Vol. 19, No. 12, December 1981, pp. 1531-1539.

26. Murman, E. H. and Cole, J. D., "Calculation of Plane Steady Transonic Flows," *AIAA Journal*, Vol. 9, No. 1, January 1971, pp. 114-121.
27. Jameson, A., "Iterative Solution of Transonic Flows Over Airfoils and Wings Including Flows at Mach 1," *Communications on Pure Applied Mathematics*, Vol. 27, 1974, pp.283-309.
28. Thompson, J. F., Warsi, Z. U. A., and Mastin, C. W., *Numerical Grid Generation Foundations and Applications*, North-Holland, New York, NY, 1985.
29. Eriksson, L. E., "Generation of Boundary-Conforming Grids Around Wing-Body Configurations Using Transfinite Interpolation," *AIAA Journal*, Vol 20 , No 10, October 1982, pp 1313-1320.
30. Brandt, A., "Multi-Level Adaptive Techniques (MLAT), I. The Multi-grid Method," IBM Research Report RC 6026, June 1976.
31. Brown, J. J., "A Multigrid Mesh-Embedding Technique for Three-Dimensional Transonic Potential Flow Analysis," NASA CP 2202, October 1981.
32. Usab Jr., W. J. and Murman, E. M., "Embedded Mesh Solutions of the Euler Equations Using a Multiple-Grid Method," AIAA Paper No. 83-1945, July 1983.
33. Brown, J. J., "An Embedded-Mesh Potential Flow Analysis," *AIAA Journal*, Vol. 22, No.2, February 1984.
34. Boppe, C. W., "Computational Transonic Flow About Realistic Aircraft Configurations," NASA CR 3243, May 1980.
35. Atta, E. H., "Component-Adaptive Grid Embedding," NASA CP 2166, October 1980, pp 157-174.
36. Atta, E. H. and Vadyak, J., "A Grid Overlapping Scheme for Flowfield Computations About Multicomponent Configurations," *AIAA Journal*, Vol. 21, No. 9, September 1983, pp 1271-1277.
37. Eisenstat, S. C., Gursky, M. C., Schultz, M. H., and Sherman, A. H., "The Yale Sparse Matrix Package. I. The Symmetric Codes," Yale University, Department of Computer Science, Research Report No. 112, 1977.
38. Eisenstat, S. C., Gursky, M. C., Schultz, M. H., and Sherman, A. H., "The Yale Sparse Matrix Package. II. The Nonsymmetric Codes," Yale University, Department of Computer Science, Research Report No. 114, 1977.
39. Fung, Y. C., *An Introduction to the Theory of Aeroelasticity*, John Wiley and Sons, Inc., New York, 1955, pp. 166-168.
40. Whitlow, W. Jr., Hafez, M. M. and Osher, S. J., "An Entropy Correction Method for Unsteady Full Potential Flows with Strong Shocks," AIAA Paper No. 86-1768-CP, 1986.